A&A 594, A27 (2016)
DOI: 10.1051/0004-6361/201525823

Astronomy & Astrophysics
Special feature

Planck 2015 results

Planck 2015 results

XXVII. The second *Planck* catalogue of Sunyaev-Zeldovich sources

Planck Collaboration: P. A. R. Ade[99], N. Aghanim[68], M. Arnaud[83], M. Ashdown[79,6], J. Aumont[68], C. Baccigalupi[97], A. J. Banday[113,10], R. B. Barreiro[74], R. Barrena[72,43], J. G. Bartlett[1,77], N. Bartolo[35,76], E. Battaner[116,117], R. Battye[78], K. Benabed[69,110], A. Benoît[66], A. Benoit-Lévy[27,69,110], J.-P. Bernard[113,10], M. Bersanelli[38,57], P. Bielewicz[113,10,97], I. Bikmaev[23,2], H. Böhringer[90], A. Bonaldi[78], L. Bonavera[74], J. R. Bond[9], J. Borrill[15,103], F. R. Bouchet[69,101], M. Bucher[1], R. Burenin[102,92], C. Burigana[56,36,58], R. C. Butler[56], E. Calabrese[106], J.-F. Cardoso[84,1,69], P. Carvalho[70,79], A. Catalano[85,82], A. Challinor[70,79,13], A. Chamballu[83,17,68], R.-R. Chary[65], H. C. Chiang[30,7], G. Chon[90], P. R. Christensen[94,42], D. L. Clements[64], S. Colombi[69,110], L. P. L. Colombo[26,77], C. Combet[85], B. Comis[85], F. Couchot[80], A. Coulais[82], B. P. Crill[77,12], A. Curto[6,74], F. Cuttaia[56], H. Dahle[71], L. Danese[97], R. D. Davies[78], R. J. Davis[78], P. de Bernardis[37], A. de Rosa[56], G. de Zotti[53,97], J. Delabrouille[1], F.-X. Désert[62], C. Dickinson[78], J. M. Diego[74], K. Dolag[115,89], H. Dole[68,67], S. Donzelli[57], O. Doré[77,12], M. Douspis[68], A. Ducout[69,64], X. Dupac[45], G. Efstathiou[70], P. R. M. Eisenhardt[77], F. Elsner[27,69,110], T. A. Enßlin[89], H. K. Eriksen[71], E. Falgarone[82], J. Fergusson[13], F. Feroz[6], A. Ferragamo[73,20], F. Finelli[56,58], O. Forni[113,10], M. Frailis[55], A. A. Fraisse[30], E. Franceschi[56], A. Frejsel[94], S. Galeotta[55], S. Galli[69], K. Ganga[1], R. T. Génova-Santos[72,43], M. Giard[113,10], Y. Giraud-Héraud[1], E. Gjerløw[71], J. González-Nuevo[74,97], K. M. Górski[77,118], K. J. B. Grainge[6,79], S. Gratton[79,70], A. Gregorio[39,55,61], A. Gruppuso[56], J. E. Gudmundsson[30], F. K. Hansen[71], D. Hanson[91,77,9], D. L. Harrison[70,79], A. Hempel[72,43,111], S. Henrot-Versillé[80], C. Hernández-Monteagudo[14,89], D. Herranz[74], S. R. Hildebrandt[77,12], E. Hivon[69,110], M. Hobson[6], W. A. Holmes[77], A. Hornstrup[18], W. Hovest[89], K. M. Huffenberger[28], G. Hurier[68], A. H. Jaffe[64], T. R. Jaffe[113,10], T. Jin[6], W. C. Jones[30], M. Juvela[29], E. Keihänen[29], R. Keskitalo[15], I. Khamitov[107,23], T. S. Kisner[87], R. Kneissl[44,8], J. Knoche[89], M. Kunz[19,68,3], H. Kurki-Suonio[29,51], G. Lagache[5,68], J.-M. Lamarre[82], A. Lasenby[6,79], M. Lattanzi[36], C. R. Lawrence[77], R. Leonardi[45], J. Lesgourgues[108,96,81], F. Levrier[82], M. Liguori[35,76], P. B. Lilje[71], M. Linden-Vørnle[18], M. López-Caniego[45,74], P. M. Lubin[33], J. F. Macías-Pérez[85], G. Maggio[55], D. Maino[38,57], D. S. Y. Mak[26], N. Mandolesi[56,36], A. Mangilli[68,80], P. G. Martin[9], E. Martínez-González[74], S. Masi[37], S. Matarrese[35,76,49], P. Mazzotta[40], P. McGehee[65], S. Mei[48,112,12], A. Melchiorri[37,59], J.-B. Melin[17], L. Mendes[45], A. Mennella[38,57], M. Migliaccio[70,79], S. Mitra[63,77], M.-A. Miville-Deschênes[68,9], A. Moneti[69], L. Montier[113,10], G. Morgante[56], D. Mortlock[64], A. Moss[100], D. Munshi[99], J. A. Murphy[93], P. Naselsky[94,42], A. Nastasi[68], F. Nati[30], P. Natoli[36,4,56], C. B. Netterfield[22], H. U. Nørgaard-Nielsen[18], F. Noviello[78], D. Novikov[88], I. Novikov[94,88], M. Olamaie[6], C. A. Oxborrow[18], F. Paci[97], L. Pagano[37,59], F. Pajot[68], D. Paoletti[56,58], F. Pasian[55], G. Patanchon[1], T. J. Pearson[12,65], O. Perdereau[80], L. Perotto[85], Y. C. Perrott[6], F. Perrotta[97], V. Pettorino[50], F. Piacentini[37], M. Piat[1], E. Pierpaoli[26], D. Pietrobon[77], S. Plaszczynski[80], E. Pointecouteau[113,10], G. Polenta[4,54], G. W. Pratt[83], G. Prézeau[12,77], S. Prunet[69,110], J.-L. Puget[68], J. P. Rachen[24,89], W. T. Reach[114], R. Rebolo[72,16,43], M. Reinecke[89], M. Remazeilles[78,68,1], C. Renault[85], A. Renzi[41,60], I. Ristorcelli[113,10], G. Rocha[77,12], C. Rosset[1], M. Rossetti[38,57], G. Roudier[1,82,77], E. Rozo[31], J. A. Rubiño-Martín[72,43], C. Rumsey[6], B. Rusholme[65], E. S. Rykoff[98], M. Sandri[56], D. Santos[85], R. D. E. Saunders[6], M. Savelainen[29,51], G. Savini[95], M. P. Schammel[6,75], D. Scott[25], M. D. Seiffert[77,12], E. P. S. Shellard[13], T. W. Shimwell[6,105], L. D. Spencer[99], S. A. Stanford[32], D. Stern[77], V. Stolyarov[6,79,104], R. Stompor[1], A. Streblyanska[73,20], R. Sudiwala[99], R. Sunyaev[89,102], D. Sutton[70,79,⋆], A.-S. Suur-Uski[29,51], J.-F. Sygnet[69], J. A. Tauber[46], L. Terenzi[47,56], L. Toffolatti[21,74,56], M. Tomasi[38,57], D. Tramonte[72,43], M. Tristram[80], M. Tucci[19], J. Tuovinen[11], G. Umana[52], L. Valenziano[56], J. Valiviita[29,51], B. Van Tent[86], P. Vielva[74], F. Villa[56], L. A. Wade[77], B. D. Wandelt[69,110,34], I. K. Wehus[77], S. D. M. White[89], E. L. Wright[109], D. Yvon[17], A. Zacchei[55], and A. Zonca[33]

(Affiliations can be found after the references)

Received 5 February 2015 / Accepted 11 June 2015

ABSTRACT

We present the all-sky *Planck* catalogue of Sunyaev-Zeldovich (SZ) sources detected from the 29 month full-mission data. The catalogue (PSZ2) is the largest SZ-selected sample of galaxy clusters yet produced and the deepest systematic all-sky survey of galaxy clusters. It contains 1653 detections, of which 1203 are confirmed clusters with identified counterparts in external data sets, and is the first SZ-selected cluster survey containing $>10^3$ confirmed clusters. We present a detailed analysis of the survey selection function in terms of its completeness and statistical reliability, placing a lower limit of 83% on the purity. Using simulations, we find that the estimates of the SZ strength parameter Y_{5R500} are robust to pressure-profile variation and beam systematics, but accurate conversion to Y_{500} requires the use of prior information on the cluster extent. We describe the multi-wavelength search for counterparts in ancillary data, which makes use of radio, microwave, infra-red, optical, and X-ray data sets, and which places emphasis on the robustness of the counterpart match. We discuss the physical properties of the new sample and identify a population of low-redshift X-ray under-luminous clusters revealed by SZ selection. These objects appear in optical and SZ surveys with consistent properties for their mass, but are almost absent from ROSAT X-ray selected samples.

Key words. cosmology: observations – galaxies: clusters: general – catalogs

⋆ Corresponding author: D. Sutton, e-mail: sutton@ast.cam.ac.uk

1. Introduction

This paper is one of a set associated with the 2015 *Planck*[1] full mission data release and describes the production and properties of the legacy catalogue of Sunyaev Zeldovich sources (PSZ2).

In the framework of hierarchical structure formation, peaks in the cosmological density field collapse and merge to form gravitationally bound halos of increasing mass (Peebles 1980). The galaxy clusters are the most massive of these bound structures and act as signposts for the extrema of the cosmological density field on the relevant scales. The evolution of galaxy cluster abundance with mass and redshift is thus a sensitive cosmological probe of the late-time Universe, providing unique constraints on the normalization of the matter density fluctuations, σ_8, the mean matter density, Ω_m, the density and equation of state of the dark energy field, Ω_{DE} and w, as well as constraining some extensions of the minimal cosmological model, such as massive neutrinos, and non-standard scenarios such as modified gravity (see e.g., Borgani & Kravtsov 2011; Allen et al. 2011). In recent years, cluster data from the microwave through to the X-ray parts of the spectrum have been used to constrain cosmological parameters (Vikhlinin et al. 2009b; Rozo et al. 2010; Hasselfield et al. 2013; Benson et al. 2013; Planck Collaboration XX 2014; Zu et al. 2014).

Galaxy clusters are multi-component objects composed of dark matter, which dominates the mass, stars, cold gas, and dust in galaxies, and a hot ionized intra-cluster medium (ICM). These different components make clusters true multi-wavelength objects. The galaxies emit in the optical and infrared. The ICM, which is the majority of the baryonic material by mass, emits in the X-rays via thermal bremsstrahlung and line emission, and energy-boosts cosmic microwave background (CMB) photons via inverse Compton scattering.

This last effect, the thermal Sunyaev Zeldovich (SZ) effect (Sunyaev & Zeldovich 1970, 1980), imprints a redshift-independent spectral distortion on the CMB photons reaching us along the line of sight to the cluster. This results in an increase in intensity at frequencies above 220 GHz, and a decrease in intensity at lower frequencies. The *Planck* High-Frequency Instrument, HFI (Planck Collaboration VII 2016; Planck Collaboration VIII 2016), is unique in providing high-precision data for both the increment and the decrement across the whole sky.

The utility of a cluster survey for cosmological work depends on our ability to determine accurately its selection function and to obtain unbiased measurements of cluster mass and redshift. The first cluster surveys consisted of galaxy overdensities identified by eye from photographic plates (Abell 1958). The construction of large optical catalogues improved significantly with the data from the SDSS (Koester et al. 2007), whose five photometric bands have allowed robust photometric classification of red-sequence cluster galaxies and accurate photometric redshifts to $z < 0.6$ across 1/4 of the sky (Hao et al. 2010; Szabo et al. 2011; Wen et al. 2009; Rykoff et al. 2014). These catalogues now typically contain 10^4–10^5 clusters and provide cluster richness as an observable that correlates with mass with an intrinsic scatter σ_{int} of about 25% (Rozo & Rykoff 2014).

Construction of X-ray cluster surveys is now a mature activity, with several catalogues available based on all-sky data from the ROSAT satellite, alongside additional catalogues of serendipitous detections from pointed observations (Ebeling et al. 1998; Böhringer et al. 2004; Reiprich & Böhringer 2002; Ebeling et al. 2010; Piffaretti et al. 2011; Burenin et al. 2007; Mehrtens et al. 2012). The most basic X-ray survey observable, the X-ray luminosity L_{500} measured within r_{500}[2], has been shown to correlate with mass, with an intrinsic scatter of about 40% (Pratt et al. 2009). Observables with lower intrinsic scatter against mass can be defined when pointed X-ray follow-up information is available, including the core-excised X-ray luminosity (Maughan 2007; Pratt et al. 2009) and Y_X, the product of the gas mass and the core-excised spectroscopic temperature (Kravtsov et al. 2006; Vikhlinin et al. 2009a; Mahdavi et al. 2013). While X-ray surveys are unique in their purity, they do, however, suffer from selection biases that favour low-redshift systems, due to flux limitations, and dynamically relaxed clusters with an X-ray bright cooling core (Eckert et al. 2011; Schuecker et al. 2003; Vikhlinin et al. 2009b; Chen et al. 2007).

SZ surveys offer a different window on the cluster population: their selection function flattens towards higher redshifts, providing a nearly mass-limited census of the cluster population at high redshift, where abundance is strongly sensitive to cosmological parameters (Carlstrom et al. 2002; Planck Collaboration XXIX 2014). The SZ survey observable is the integrated Comptonisation parameter, Y_{sz}, which is related to the integrated electron pressure and hence the total thermal energy of the cluster gas. It is also expected to correlate with mass, with a low intrinsic scatter and little dependence on the dynamical state of the cluster (e.g., da Silva et al. 2004; Kay et al. 2012; Hoekstra et al. 2012; Planck Collaboration Int. III 2013; Sifón et al. 2013).

The spherically-integrated pressure profiles of X-ray and SZ clusters have been observed to follow a near universal profile with little dispersion (Arnaud et al. 2010; Planck Collaboration Int. V 2013), permitting the detection of clusters with a matched multi-frequency filter based on some assumed pressure profile (Herranz et al. 2002; Melin et al. 2006). Samples constructed this way have well understood selection functions, though discrepancies due to profile mismatch or contaminating infra-red emission may still be present to some level. Large SZ surveys have only appeared recently, with catalogues of order 10^2 clusters released by the Atacama Cosmology Telescope (Hasselfield et al. 2013), the South Pole Telescope (Reichardt et al. 2013), and *Planck* satellite collaborations.

This is the third all-sky catalogue produced from *Planck* SZ data. The early Sunyaev-Zeldovich (ESZ) catalogue presented 189 clusters detected from 10 months of survey data (Planck Collaboration 2011), while the PSZ1, the full-sky catalogue assembled from the nominal mission data, presented 1227 cluster candidates detected from 15.5 months of data (Planck Collaboration XXIX 2014). This paper presents 1653 candidates detected from the full HFI mission survey of 29 months. 1203 of these have been confirmed in ancillary data, and 1094 have redshift estimates. The PSZ2 expands the scope and sensitivity of the SZ view of galaxy clusters by substantially increasing the number of lower mass clusters available for study. It is also expected to contain many new, as yet unconfirmed, high-redshift clusters. We report on the construction and characterisation of

[1] *Planck* (http://www.esa.int/Planck) is a project of the European Space Agency (ESA) with instruments provided by two scientific consortia funded by ESA member states and led by Principal Investigators from France and Italy, telescope reflectors provided through a collaboration between ESA and a scientific consortium led and funded by Denmark, and additional contributions from NASA (USA).

[2] The quantity r_{500} is the cluster-centric distance within which the mean density is 500 times the critical density of the Universe at the cluster redshift.

the catalogue, presenting the survey selection functions and a compilation of multi-wavelength ancillary information, including redshifts. We also briefly discuss the physical properties of the sample.

This paper is organized as follows. In Sect. 2 we summarize the three extraction algorithms used to build the catalogue, focussing on the changes in the algorithms since they were used to construct the PSZ1. In Sect. 3 we describe the construction of the catalogue. In Sect. 4 we present the survey selection functions (completeness and statistical reliability) and the complementary approaches used to estimate them, while in Sect. 5 we discuss and validate the estimation of the Y_{sz} parameters, both blindly and when using prior information, and we compare the consistency of the new catalogue with the PSZ1 in Sect. 6. In Sect. 7 we report on the search for multi-wavelength counterparts in ancillary catalogues and follow-up observations. Finally we present the physical properties of the sample in Sect. 8 and conclude in Sect. 9. Appendix A summarizes new high-z SDSS redshifts. Appendices B, C, and E present a detailed account of the changes with respect to the PSZ1 in terms of redshift assignments, detection code implementations, and missing PSZ1 detections, respectively. A full description of the available data products is given in Appendix D. All the data products can be obtained from the Planck Legacy Archive[3].

2. Extraction algorithms

The SZ detection and parameter estimation algorithms used to construct the PSZ2 extend and refine those used to construct the PSZ1. In this section we recall the principles of the three algorithms. The refinements of each algorithm since the PSZ1 release are detailed in Appendix C. Two of the algorithms (`MMF1` and `MMF3`) are based on the same technique (matched multi-filters) but have been implemented independently[4]. The third one (`PwS` for PowellSnakes) relies on Bayesian inference.

2.1. Matched Multi-filters: `MMF1` and `MMF3`

The matched filtering technique was first proposed for SZ studies by Haehnelt & Tegmark (1996). It was subsequently developed by Herranz et al. (2002) and Melin et al. (2006) for SZ cluster extraction in multifrequency data sets such as *Planck*. The method was later adopted by the SPT and ACT collaborations (Staniszewski et al. 2009; Marriage et al. 2011).

We model the vector of map emission at each frequency $\boldsymbol{m}(\boldsymbol{x})$, at a given position on the sky $\boldsymbol{x}$ as

$$\boldsymbol{m}(\boldsymbol{x}) = y_{\rm o}\boldsymbol{t}_{\theta_{\rm s}}(\boldsymbol{x}) + \boldsymbol{n}(\boldsymbol{x}) \quad (1)$$

where $\boldsymbol{t}_{\theta_{\rm s}}(\boldsymbol{x})$ is the signal vector describing the spatial distribution at each frequency of the SZ emission from a cluster with angular scale radius $\theta_{\rm s}$, and $\boldsymbol{n}(\boldsymbol{x})$ is the total astrophysical and instrumental noise. The ith frequency component of the signal vector is the normalized cluster profile $\tau_{\theta_{\rm s}}(\boldsymbol{x})$ (Arnaud et al. 2010) convolved by the *Planck* beams $b_i(\boldsymbol{x})$ and scaled with the characteristic frequency dependance $j_\nu(\nu_i)$ of the thermal SZ effect: $\boldsymbol{t}_{\theta_{\rm s}}(\boldsymbol{x})_i = j_\nu(\nu_i)[b_i * \tau_{\theta_{\rm s}}](\boldsymbol{x})$. $\theta_{\rm s}$ is the cluster scale radius, which is related to θ_{500} through the concentration parameter c_{500} by $\theta_{500} = c_{500}\times\theta_{\rm s}$. The matched multi-filter $\boldsymbol{\Psi}_{\boldsymbol{\theta}_{\rm s}}$ allows us to recover an unbiased estimate $\hat{y}_{\rm o}$ of the central Comptonization parameters $y_{\rm o}$ with minimal variance $\sigma^2_{\theta_{\rm s}}$:

$$\hat{y}_{\rm o} = \int {\rm d}^2x\, \boldsymbol{\Psi}_{\boldsymbol{\theta}_{\rm s}}{}^T(\boldsymbol{x}) \cdot \boldsymbol{m}(\boldsymbol{x}), \quad (2)$$

where

$$\boldsymbol{\Psi}_{\boldsymbol{\theta}_{\rm s}}(\boldsymbol{k}) = \sigma^2_{\theta_{\rm s}} \boldsymbol{P}^{-1}(\boldsymbol{k}) \cdot \boldsymbol{t}_{\boldsymbol{\theta}_{\rm s}}(\boldsymbol{k}), \quad (3)$$

with

$$\sigma_{\theta_{\rm s}} \equiv \left[\int {\rm d}^2k\, \boldsymbol{t}_{\boldsymbol{\theta}_{\rm s}}{}^T(\boldsymbol{k}) \cdot \boldsymbol{P}^{-1} \cdot \boldsymbol{t}_{\boldsymbol{\theta}_{\rm s}}(\boldsymbol{k})\right]^{-1/2}, \quad (4)$$

$\boldsymbol{P}(\boldsymbol{k})$ being the cross-channel power spectrum matrix of the maps. This is effectively the noise matrix for the MMF, because the tSZ is small compared to other astrophysical signals, and is estimated directly from the maps.

The MMF algorithms first divide each *Planck* all-sky map into 640/504 tangential maps (14.66/10 degrees on a side) for `MMF1`/`MMF3`, respectively. Each set of tangential maps is filtered by $\Psi_{\theta_{\rm s}}$, with the assumed cluster size varying from $\theta_{\rm s} = 0.8$ to 32 arcmin. We then locate peaks in the filtered maps above an S/N threshold of four. The locations of the peaks give the positions of our cluster candidates. These are then combined into a single all-sky catalogue by merging candidates separated by less than 10 arcmin. For `MMF3`, we perform a second step by creating sets of smaller rectangular frequency maps centred on the cluster candidates identified in the first step. We re-apply the MMF on these centred tangential maps, which allows a better estimation of the background. During the second step, the sizes and fluxes are estimated more precisely. This second step is only performed for `MMF3`, because the overlap of the tangential maps in the first step is small compared to `MMF1` and `PwS`.

We define the blind cluster size as the filter scale that maximizes the S/N at the location of the cluster candidate and the blind flux is defined as the corresponding $\hat{y}_{\rm o}$ parameter. We then define the integrated blind flux as:

$$Y_{5R500} = \hat{y}_{\rm o} \int_{\theta<5\times\theta_{500}} {\rm d}r\tau_{\theta_{\rm s}}(r). \quad (5)$$

Each of the algorithms produces probability distributions in the ($\theta_{\rm s}$, Y_{5R500}) plane for each detection, marginalizing over the parameters for the centre of the cluster, which possess a Gaussian likelihood. The algorithms also return an estimate of the radial position uncertainty, $\theta_{\rm err}$ from the position likelihood.

Although the two implementations of the MMF are quite close, they produce noticeably different catalogues because the extraction is very sensitive to the estimation of the background (Eq. (4)). Both the size adopted for the tangential maps and the details of the estimation of the matrix $\boldsymbol{P}(k)$ impact the S/N and hence which peaks are detected.

2.2. PowellSnakes (`PwS`)

PowellSnakes (`PwS`) is a fast, fully Bayesian, multi-frequency detection algorithm designed to identify and characterize compact objects buried in a diffuse background, as described in Carvalho et al. (2009, 2012). `PwS` operates using about 2800 square patches of 14.66 degree on a side, in order to ensure highly redundant sky coverage. `PwS` detects candidate clusters and at the same time computes the evidence ratio and samples from the posterior distributions of the cluster parameters. Then,

[3] http://www.cosmos.esa.int/web/planck/pla

[4] The MMF numbers were given after the comparison of twelve algorithms in an earlier phase of the *Planck* mission (Melin et al. 2012). `MMF1` and `MMF3` were, respectively, the first and third algorithm based on matched multi-filters to enter the comparison.

Table 1. Effective frequencies and Gaussian beam widths assumed for extraction per channel.

Channel	*FWHM* [arcmin]	$\nu_{\rm eff}$ [GHz]
100	9.66	103.42
143	7.22	144.90
217	4.90	222.60
353	4.92	355.22
545	4.67	528.40
857	4.22	776.58

Notes. The beam widths are the mean full-width-at-half-maximum, in arcmin, of the Gaussian fits to the per-pixel effective beams estimated by the FEBeCoP algorithm (Mitra et al. 2011). The effective frequencies $\nu_{\rm eff}$, shown in GHz, encapsulate band-pass effects in each channel (Planck Collaboration VIII 2016).

it merges the sub-catalogues from each patch map and applies criteria for acceptance or rejection of the detection, as described in Carvalho et al. (2012). Priors may be provided for the position, integrated flux and radius of the clusters. For cluster detection, we apply flat priors on the position and non-informative priors on the radius and integrated flux, as determined using Jeffrey's method. PwS uses a calibration of the cross-power spectrum that uses an iterative scheme to reduce the contamination of the background by the SZ signal itself. This makes PwS particularly robust to small changes in the background.

3. Catalogue construction

The main catalogue is constructed by combining the detections made by the three methods into a union catalogue, while merging the detections made by more than one method. Half of the detections in this union set are also in the intersection catalogue, defined as those detections made by all three codes simultaneously. This section describes the technical details of the construction of these catalogues.

3.1. Pipeline

The SZ catalogue construction pipeline is shown in schematic form in Fig. 1 and largely follows the process used to build the PSZ1. The *Planck* data required for the construction of the catalogue comprises the HFI maps (Planck Collaboration VII 2016; Planck Collaboration VIII 2016), point source catalogues for each of the HFI channels (Planck Collaboration XXVI 2016), effective frequencies and beam widths per HFI channel (as shown in Table 1), survey masks based on dust emission as seen in the highest *Planck* channels, and the catalogue of extended Galactic cold-clump detections (Planck Collaboration XXVIII 2016).

The HFI maps are pre-processed to fill areas of missing data (typically a few pixels), or areas with unusable data, specifically bright point sources. Point sources with $S/N > 10$ in any channel are masked out to a radius of $3\sigma_{\rm beam}$, using a harmonic infilling algorithm. This prevents spurious detections caused by Fourier ringing in the filtered maps used by the detection algorithms. As a further guard against such spurious detections, we reject any detections within $5\sigma_{\rm beam}$ of a filled point source. We have verified that this treatment reduces spurious detections due to bright point sources to negligible levels in simulations, while reducing the effective survey area by just 1.4% of the sky. Together with

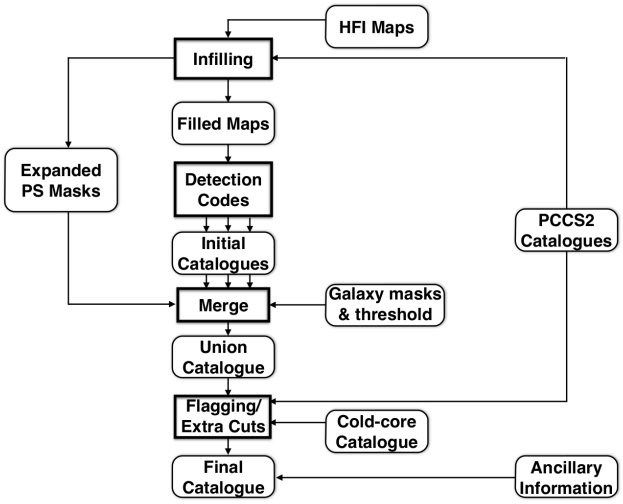

Fig. 1. Pipeline for catalogue construction.

the 15% Galactic dust and Magellanic cloud mask, this defines a survey area of 83.6% of the sky.

After infilling, the three detection codes produce individual candidate catalogues down to a threshold $S/N > 4.5$. The catalogues are then merged to form a union catalogue, using the dust and extended point source masks discussed above to define the survey area. The merging procedure identifies the highest S/N detection as the reference position during the merge and any detections by other codes within 5 arcmin are identified with the reference position. The reference position and S/N are reported in the union catalogue.

PwS can produce a small number of high-significance spurious detections associated with Galactic dust emission. We apply an extra cut of PwS-only detections at $S/N > 10$ where the spectrum has a poor goodness-of-fit to the SZ effect, $\chi^2_{\rm red} > 16$.

We also remove five PSZ2 detections that match PSZ1 detections confirmed to be spurious by the PSZ1 follow-up programme (these were the ones that we re-detected; there were many more confirmed spurious detections from the programme).

Finally the sample is flagged to identify the various subsamples discussed in Sect. 3.3. The most important of these flags is discussed in the next section.

3.2. Infra-red spurious detections

Cold compact infra-red emission, particularly that due to Galactic cold-clumps, can lead to high-significance spurious detections. We identify these detections by searching for 7 arcmin matches with the *Planck* cold-clump catalogue (C3PO), or with PCCS2 detections at both 545 GHz and 857 GHz. This matching radius was chosen because it is the typical size of a *Planck* detected cold-clump (Planck Collaboration XXVIII 2016).

318 raw union detections match these criteria. They tightly follow the distribution of Galactic emission (see Fig. 2), such that if the 65% Galactic dust mask (which was used for constructing cluster sample for cosmology used by Planck Collaboration XXIV 2016) is used to define the sample instead of the 85% dust mask, the number of IR-matched raw detections drops to 40. For the high-purity sample formed from the intersection of all three codes, the numbers are 82 and 13 for the 85% and 65% dust masks respectively. Some high latitude spurious candidates remain. To minimize the effect of spurious detections on the catalogue, we remove these IR matches.

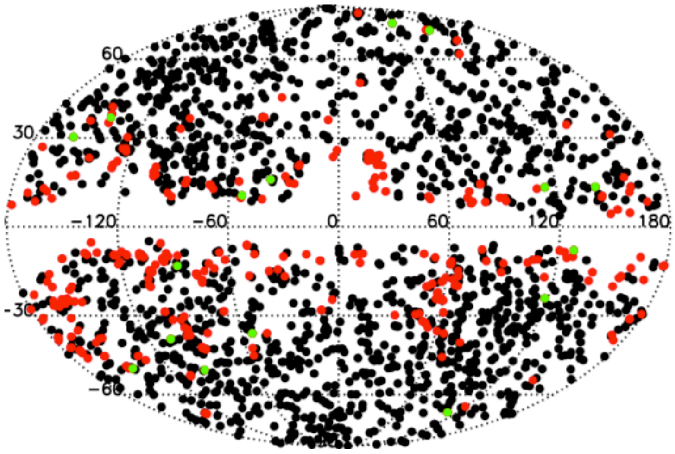

Fig. 2. Distribution of raw SZ detections, with deleted infra-red flagged candidates in red and retained infra-red flagged detections in green. Black points denote detections without an IR flag.

However, we have retained in the sample all 15 confirmed clusters that match these criteria. These IR-contaminated clusters represent about 1.5% of the total confirmed clusters in the PSZ2. In the catalogue, we define a flag, IR_FLAG, to denote the retained clusters that match these criteria; they can be expected to have heavily contaminated SZ signal. This compares well to the 12 contaminated clusters that would be expected from chance alignment if the cluster and IR source populations were uncorrelated.

A small fraction of the unconfirmed detections deleted due to IR-contaminations may have been real clusters. Assuming that optical and X-ray confirmation is unbiased with regard to the presence of IR emission, we estimate these deletions to bias our completeness estimates by less than 1%.

3.3. Catalogue sub-samples

The union catalogue can be decomposed into separate subsamples, defined as the primary catalogues of the three individual detection codes (PwS, MMF1, MMF3), as well as into unions and intersections thereof. The intersection subsample of candidates detected by all three algorithms can be used as a high-reliability catalogue with less than 2% spurious contamination outside of the Galactic plane (see Sect. 4.6).

3.3.1. The cosmology catalogues

We constructed two cluster catalogues for cosmology studies from the MMF3 and the intersection sub-samples, respectively. For these catalogues, our goal was to maximize as much as possible the number of detections, while keeping contamination negligible. A good compromise is to set the S/N threshold to 6 and apply a 65% Galactic and point source mask, as in our 2013 cosmological analysis (Planck Collaboration XX 2014). In this earlier paper, our baseline MMF3 cosmological sample was constructed using a threshold of 7 on the 15.5 month maps, which is equivalent to 8.5 on the full mission maps. Estimations from the Monte Carlo quality assessment, QA (discussed in Sect. 4) suggest that our 2014 intersection sample should be >99% pure for a threshold of 6.

The MMF3 cosmological sample contains 439 detections with 433 confirmed redshifts. The intersection cosmological sample contains 493 detections, with 479 confirmed redshifts. Assuming that all detections having VALIDATION flag greater than zero are clusters, the empirical purity of our samples are >99.8% for MMF3 and >99.6% for the intersection. Note that the intersection sample contains more clusters than the MMF3 sample for the same S/N threshold. This is expected, since the definition of the S/N for the intersection sample is to use the highest value from the three detection methods.

The completeness is also a crucial piece of information. It is computed more easily with the single method catalogue for which the analytical error-function (erf) approximation can be used (as defined in Planck Collaboration XXIX 2014). In Sect. 4.3 and in Planck Collaboration XXIV (2016), we show that this analytical model is still valid for the considered threshold. For the intersection sample, we rely on the Monte Carlo estimation of the completeness described in Sect. 4.2.

These two samples are used in the cosmological parameter analysis of Planck Collaboration XXIV (2016). Detections that are included in either of the cosmology samples are noted in the main catalogue (see Appendix D).

3.4. Consistency between codes

We construct the union sample using the code with the most significant detection to supply the reference position and S/N. This contrasts with the PSZ1approach, which used a pre-defined code ordering to select the reference position and S/N. In this section, we demonstrate the consistency of the detection characteristics of the codes for common detections, motivating this change in catalogue construction.

We fit the S/N relation between codes using the Bayesian approach described by Hogg et al. (2010) for linear fits with covariant errors in both variables. We consider the catalogue S/N values to be estimates of a true underlying variable, s, with Gaussian uncertainties with standard deviation $\sigma = 1$.

We relate the s values for two different catalogues using a simple linear model

$$s_2 = \alpha s_1 + A, \tag{6}$$

where we assume flat priors for the intercept A, and a flat prior on the arc-tangent of the gradient α, such that $p(\alpha) \propto 1/(1+\alpha^2)$. We also allow for a Gaussian intrinsic scatter between the s values that includes any variation beyond the measurement uncertainty on s. This is parameterised by $\sigma_{\rm int}$, with an uninformative prior $p(\sigma_{\rm int}) \propto 1/\sigma_{\rm int}$.

We assume a fiducial correlation of $\rho_{\rm corr} = 0.8$ between the S/N estimates of each code pair, which is typical of the correlation between the matched multi-filtered patches of each code. The fit results are shown in Table 2.

The S/N estimates from the three codes are compared in Fig. 3, which also shows the best-fit relation. MMF1 produces noticeably weaker S/N values than the other two codes for the 14 very strong detections at $S/N > 20$. Excluding these exceptional cases from the comparison, the best-fit relations between the S/N values from each code show no significant deviations from equality between any of the codes.

There are a small number of highly significant outliers in the relation between PwS and the MMF codes. These are clusters imbedded in dusty regions where the different recipes for the filtered patch cross-power spectrum vary significantly and the likelihood assumptions common to all codes break down. PwS shows outlier behaviour relative to the other codes, since its recipe is most different from the other codes.

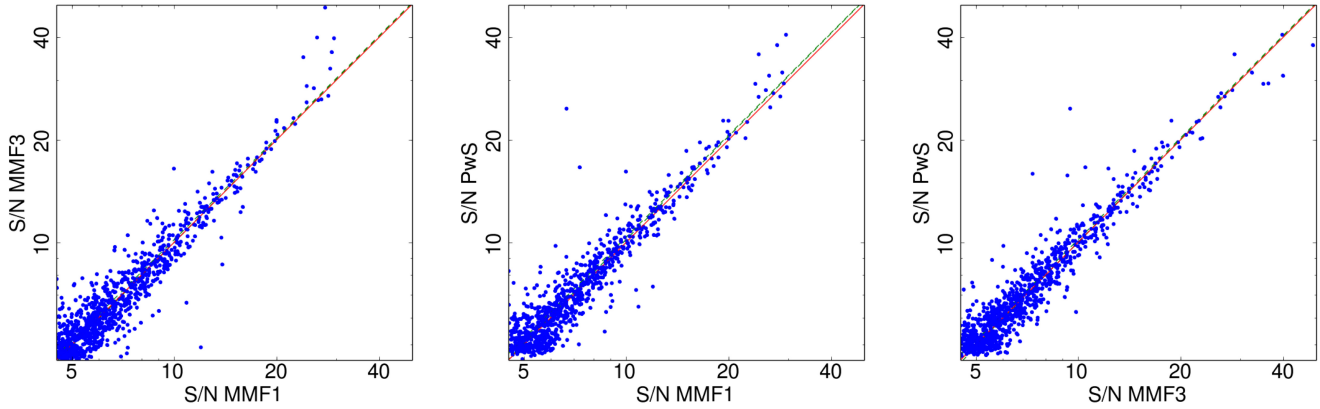

Fig. 3. Comparison of the S/N estimates from the three detection codes. The dashed green curves show the best-fit relation for a correlation of 0.8 and the red line is the line of equality.

Table 2. Results of fits between S/N from the three detection codes, using the fitting function in Eq. (6).

s_1	s_2	N	A	α	$\sigma_{\rm int}$
MMF1	MMF3	1032	-0.01 ± 0.01	1.01 ± 0.01	0.033 ± 0.001
MMF1	PwS	985	-0.02 ± 0.01	1.03 ± 0.02	0.030 ± 0.001
MMF3	PwS	1045	0.00 ± 0.01	1.01 ± 0.01	0.031 ± 0.001

Notes. The assumed correlation of the uncertainties of s_1 and s_2 was 0.8.

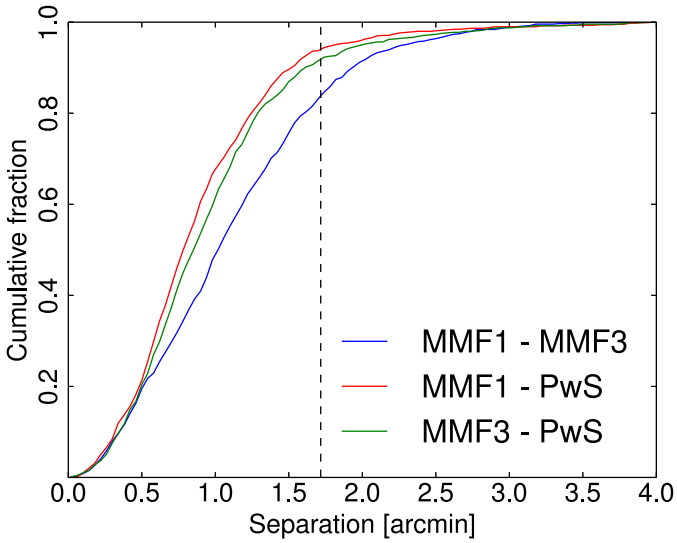

Fig. 4. Cumulative distribution of angular separation between matched detections for each possible code pair. The vertical dashed line indicates the width of a Healpix pixel at the *Planck* resolution.

Figure 4 shows the consistency of the position estimates between the codes. The positions of MMF1 and MMF3 are less consistent with one another than any other code combination. The 67% bound on the MMF1−MMF3 separation is 1.3 arcmin, while for MMF1−PwS it is 0.98 arcmin and for MMF3−PwS it is 1.1 arcmin. This is consistent with the observation from the quality assessment that the PwS positions are the most robust (Sect. 4.4).

4. Selection function

A necessary element of any cluster sample is the selection function that relates the detected sample to the underlying population of objects. The selection function comprises two complementary functions: the completeness, which defines the probability that a given real object will be detected; and the statistical reliability, also known as purity, which defines the probability that a given detection corresponds to a real object. As a function of underlying object attributes, the completeness is a function of underlying SZ observables, θ_{500} and Y_{500}. The reliability is a statistical function of detection attributes and is presented as a function of detection S/N.

4.1. Monte-Carlo Injection

The selection function is determined by the Monte-Carlo injection of simulated clusters into both real and simulated *Planck* maps. A common segment is the injection of cluster SZ signal. The cluster signal is assumed to be spherically symmetric and to follow a pressure profile similar to the generalized Navarro-Frenk-White (GNFW) profile assumed in the catalogue extraction (Nagai et al. 2007; Arnaud et al. 2010).

To include the effects of system-on-system variation in the pressure distribution, we draw the spherically-averaged individual pressure profiles from a set of 910 pressure profiles from simulated clusters coming from the cosmo-OWLS simulations (Le Brun et al. 2014; McCarthy et al. 2014), an extension of the OverWhelmingly Large Simulations project (Schaye et al. 2010). These pressure profiles are empirical in the sense that they have not been fitted using a GNFW profile: the mean pressure is used within concentric radial shells (after the subtraction of obvious sub-structures) and the injected profiles are interpolated across these shells. The simulated clusters were selected for this sample by requiring that their mass be above the approximate limiting mass for *Planck* at that redshift. The ensemble of simulated profiles are shown in Fig. 5. Each profile is normalized such that the spherically integrated Y_{500} parameter matches the fiducial injected (Y_{500}, θ_{500}) parameters for the halo. The injected

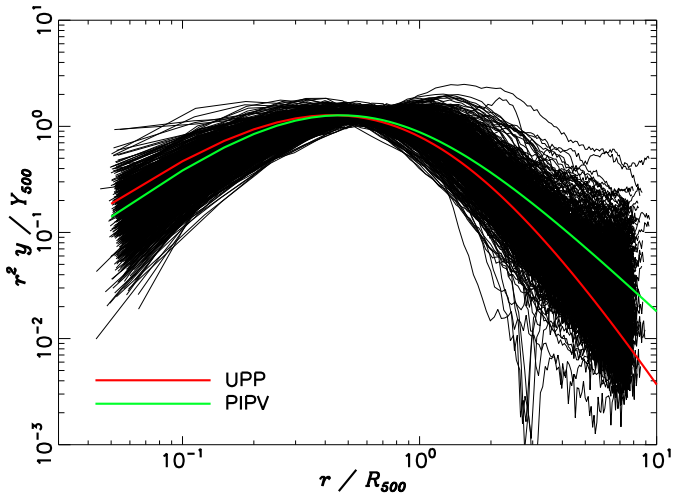

Fig. 5. The 910 simulated pressure profiles from the cosmo-OWLS simulations used for cluster injection. Also shown are the assumed extraction profile (UPP) and the best-fit profile from a sample of 62 pressure profiles fitted using *Planck* and X-ray data (PIPV, Planck Collaboration Int. V 2013).

(Y_{500}, θ_{500}) are different for completeness and reliability simulations and each is discussed below.

Effective beam variation is an important consideration for the unresolved clusters at the intermediate and high redshifts of cosmological interest. We deal with this by convolving the injected clusters with effective beams in each pixel including asymmetry computed following Mitra et al. (2011)

4.2. Completeness

The completeness is defined as the probability that a cluster with a given set of true values for the observables (Y_{500}, θ_{500}) will be detected, given a set of selection criteria. A good approximation to the completeness can be defined using the assumption of Gaussianity in the detection noise. In this case, the completeness for a particular detection code, χ, follows the error function (erf()), parametrized by a selection threshold q and the local detection noise at the clusters radial size, $\sigma_Y(\theta_{500}, \phi, \psi)$,

$$\chi(Y_{500}, \theta_{500}, \phi, \psi) = \frac{1}{2}\left[1 - \mathrm{erf}\left(\frac{Y_{500} - q\sigma_Y(\theta_{500}, \phi, \psi)}{\sqrt{2}\sigma_Y(\theta_{500}, \phi, \psi)}\right)\right]. \quad (7)$$

This approach is not suited to the union and intersection catalogues from *Planck*, due to the difficulty in modelling correlations between detection codes. We determine the completeness by brute force, injecting and detecting simulated clusters into the *Planck* sky maps. This approach has the advantage that all algorithmic effects are encoded into the completeness, and the effects of systematic errors, such as beam and pressure profile variation, can be characterized. This approach also fully accounts for the non-Gaussianity of the detection noise due to foreground emission.

The injected (Y_{500}, θ_{500}) parameters are drawn from a uniform distribution in the logarithm of each variable, ensuring that our logarithmically spaced completeness bins have approximately equal numbers of injected sources.

As the completeness is estimated from injection into real data, injected sources can contribute to the detection noise. We therefore use an injection mode, as was the case for the PSZ1 completeness, where injected clusters are removed from the maps used to estimate the noise statistics. We also avoid superimposing injected clusters on top of one another, or on top of real data detections. Together, these ensure that the noise statistics for injected clusters are the same as for the real detections in the map.

We release as a product the Monte-Carlo completeness of the catalogues at thresholds stepped by 0.5 in S/N over the range $4.5 \leq S/N \leq 10$. Figure 6 shows the completeness of the union and intersection catalogues as functions of input (Y_{500}, θ_{500}) and at representative values of θ_{500}, for three detection thresholds. The union and intersection catalogues are most similar at high S/N, where they match well except at small scales. Here the intersection catalogue follows the lower completeness of `MMF1`. This is due to an extra selection step in that code, which removes spurious detections caused by point sources. The union and intersection catalogues mark the upper and lower limits of the completeness values for the sub-catalogues based on the individual codes.

The completeness of the *Planck* cluster catalogue is robust with respect to deviations of the real SZ profiles of galaxy clusters from the one assumed by the algorithms for filter construction. To demonstrate this, we compare $\chi_{\rm MC}$, the Monte-Carlo completeness for the `MMF3` sample, using the cosmoOWLs profile variation prescription and effective beam variation, to $\chi_{\rm erf}$, the semi-analytic erf() completeness given by Eq. (7). This comparison is shown in Fig. 7, where we show the difference between the two estimates as a function of Y_{500} and θ_{500}. We also show the individual completeness values as functions of Y_{500} for representative values of θ_{500}.

The error function is a good approximation to the MC completeness for the cosmology sample, which uses a higher S/N cut and a larger Galactic mask than the full survey. The MC estimate corrects this analytic completeness by up to 20% for large resolved clusters, where $\chi_{\rm MC}$ is systematically lower than the erf() expectation, primarily due to variation in the cluster pressure profiles. For unresolved clusters, the drop-off in $\chi_{\rm MC}$ is slightly wider than the erf() expectation, reflecting variation both of pressure profiles and of effective beams.

The impact of these changes in completeness on expected number counts and inferred cosmological parameters for the cosmology sample is analysed in Planck Collaboration XXIV (2016). The difference between the Monte Carlo and erf() completeness results in a change in modelled number counts of typically 2.5% (with a maximum of 9%) in each redshift bin. This translates into a 0.26σ shift of the posterior peak for the implied linear fluctuation amplitude, σ_8.

The MC completeness is systematically lower than the analytic approximation for the full survey. One of the causes of this is Galactic dust contamination, which is stronger in the extra 20% of the sky included in the full survey area relative to the cosmology sample area. This tends to reduce the S/N of clusters on affected lines of sight.

We note that this approach ignores other potential astrophysical effects that could affect the completeness. Radio emission is known to be correlated with cluster positions, potentially "filling in" the SZ decrement, though recent estimates suggest that this effect is typically small in *Planck* data (Rodriguez-Gonzalvez et al. 2015). Departures of the pressure distribution from spherical symmetry may also affect the completeness, though this effect is only likely to be significant for nearby and dynamically disturbed clusters, which are not small compared to the *Planck* beams. We test for some of these effects through external validation of the completeness in the next section, and explicitly through simulation in Sect. 4.5.

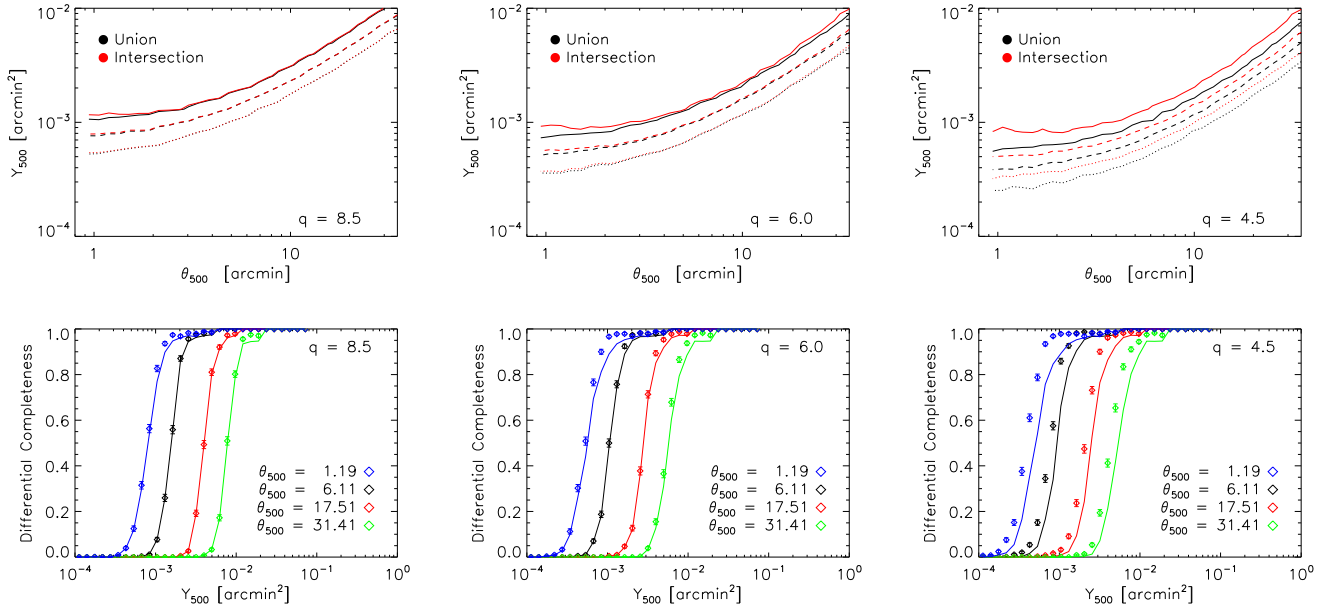

Fig. 6. Completeness of the union and intersection samples at progressively lower S/N thresholds. *From left to right*, the thresholds are 8.5, 6.0 and 4.5 (the survey threshold). In the *top panels*, the dotted lines denote 15% completeness, the dashed lines 50%, and the solid lines 85% completeness. In the *bottom panels*, the union is denoted by the diamonds with Monte Carlo uncertainties based on binomial statistics, and the intersection is denoted by the solid lines.

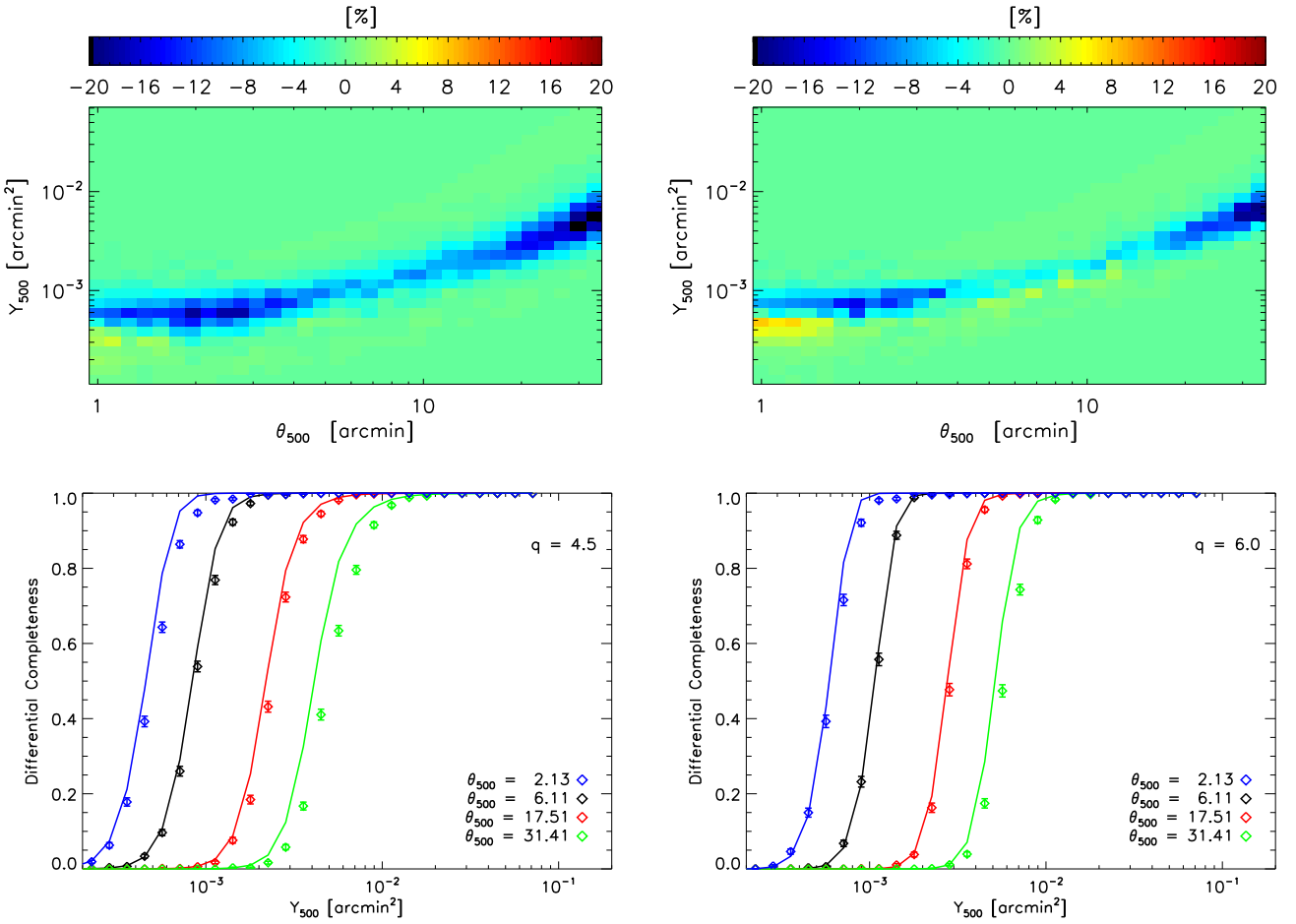

Fig. 7. Differences between the semi-analytic and Monte Carlo completenesses for `MMF3`. *The left panels* show the difference for the full survey over 85% of the sky with a $q = 4.5$ threshold. *The right panels* show the difference for the `MMF3` cosmology sample, covering 65% of the sky to a threshold of $q = 6.0$. *The top panels* show the difference $\chi_{\rm MC} - \chi_{\rm erf}$ as a percentage. *The bottom panels* compare the completenesses at particular θ_{500} values. The Monte-Carlo completeness is denoted by diamonds and the erf() completeness by solid lines.

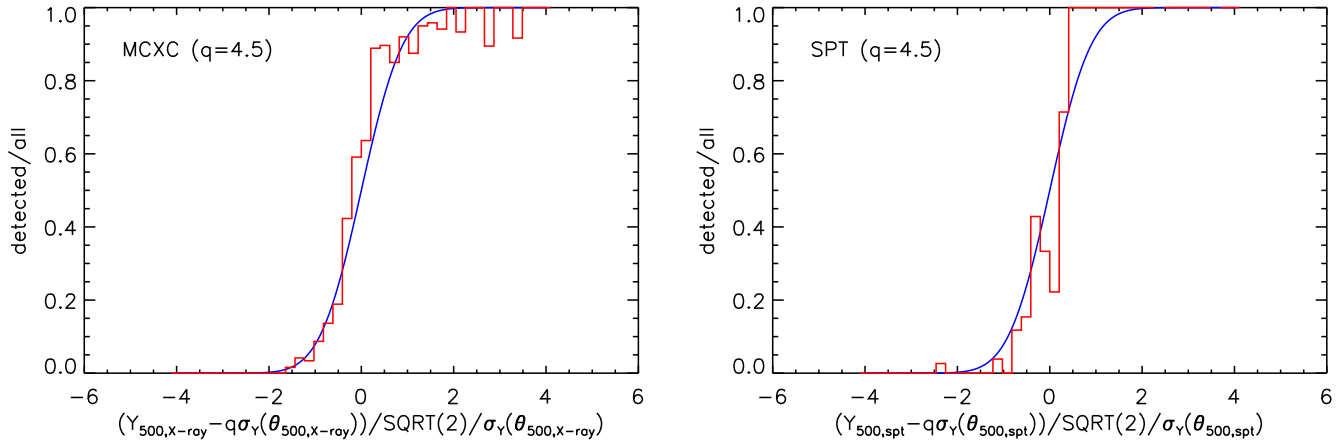

Fig. 8. `MMF3` completeness for the PSZ2 catalogue (S/N threshold $q > 4.5$) determined from the MCXC (*left*) and SPT (*right*) catalogues. This external estimate (red histogram) is in good agreement with the analytic erf() calculation (solid blue line), except for SPT at the high probability end (see text).

Another source of bias is the presence of correlated IR emission from cluster member galaxies. Planck Collaboration XXIII (2016) shows that IR point sources are more numerous in the direction of galaxy clusters, especially at higher redshift, and contribute significantly to the cluster SED at the *Planck* frequencies. Initial tests, injecting cluster signals with the combined IR+tSZ spectrum of $z > 0.22$ clusters observed in Planck Collaboration XXIII (2016), suggest that this reduces the completeness for unresolved clusters. The effective detection threshold can move upwards by up to 30% for unresolved clusters ($\theta_{500} < 7$ arcmin), though no significant changes appear for resolved clusters . Future work is warranted to characterize the evolution and scatter of this IR emission and to propagate the effect on completeness through to cosmological parameters.

4.3. External validation of the completeness

We validated our Monte Carlo completeness calculation and the simple analytical erf() model in Eq. (7) by using the MCXC (Piffaretti et al. 2011) and SPT (Bleem et al. 2015) catalogues. The *Planck* detection threshold is passed across the cluster distributions of these two samples. This is illustrated in Fig. 4 of Chamballu et al. (2012) for the MCXC. This allows us to characterize our completeness by checking if the fraction of detected clusters follows the expected probability distribution as a function of their parameters. For each cluster of the MCXC catalogue, we use the `MMF3` algorithm to extract its flux Y_{500} and associated error σ_Y at the location and for the size given in the X-ray catalogue. We then build the quantity $\delta = (Y_{500} - q\sigma_Y)/\sqrt{2}\sigma_Y$, q being the detection threshold (here 4.5) and σ_Y the noise of the filtered maps. We make the corresponding histogram of this quantity for all the clusters and for the clusters detected by `MMF3`. The ratio of the two histograms is an empirical estimate of the completeness. Results are shown in Fig. 8 for the MCXC (left) and the SPT (right) catalogues. For MCXC, the estimation is in good agreement with the expected simple analytical erf() model ($0.5\,(1 + \mathrm{erf}(\delta))$). For SPT, the estimated completeness is also in good agreement except for $\delta > 1$ where it is higher than the analytic expectation. We attribute this behaviour to the correlation between SPT and *Planck* detections. The SPT catalogue is SZ-based, so a cluster detected by SPT will have a higher than random probability to be detected by *Planck*. This leads to an overestimation of the completeness at the high probability end.

4.4. Position estimates

We characterize the positional recovery of the *Planck* detections using source injection into real data, including pressure profile and beam variation. We draw input clusters from a realistic distribution of (Y_{500}, θ_{500}), which is the same as used for the reliability in Sect. 4.6.

Figure 9 shows the comparative performance of the individual detection codes, and of the reference position chosen for the union catalogue. `PwS` produces the most accurate positions, with 67% of detected positions being within 1.18 arcmin of the input position. For `MMF1` and `MMF3`, the 67% bound is 1.58 arcmin and 1.52 arcmin, respectively. The union and intersection accuracy follow that of the MMFs, with 67% bounds of 1.53 arcmin. We observe that our inter-code merging radius of 5 arcmin is conservative, given the expected position uncertainties.

4.5. Impact of cluster morphology

Clusters are known to possess asymmetric morphologies and a wide range of dynamical states, from irregular merging clusters to regular relaxed clusters. While the completeness simulations have included some morphology variations through variation of the injected radial pressure profile, this ignores the effects of the sub-structures and asymmetries, which may induce detection biases for large clusters at low redshift resolved by the *Planck* beams, $FWHM \approx 7$ arcmin.

Neither of the external samples used in Sect. 4.3 to validate the completeness allow us to properly probe resolved, irregular clusters at low-redshift. The MCXC is biased towards regular clusters, due to X-ray selection effects, while the *Planck* completeness drop-off lies substantially beneath the SPT mass limit at low redshift, so this drop-off is not sampled.

We address the effects of realistic morphology by injecting into the *Planck* maps the raw 2D projected Compton-Y signal from a sample of hydrodynamically simulated cosmoOWLs clusters. The clusters were injected with a large enough angular extent, $\theta_{500} = 20$ arcmin, that they were resolvable in the *Planck* data, and with a range of Y_{500} that encompassed the

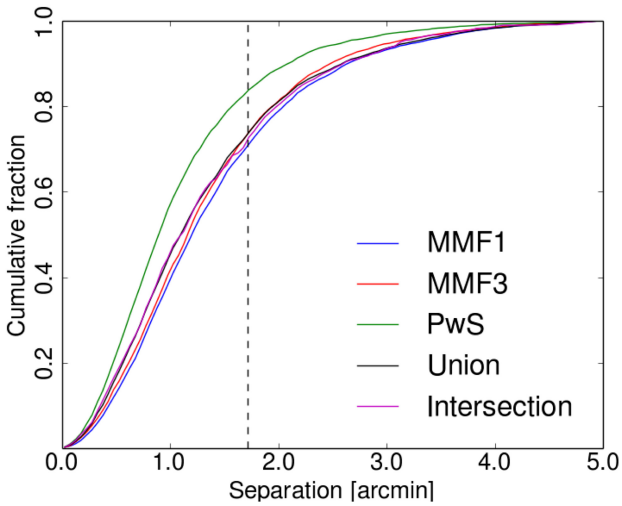

Fig. 9. Cumulative distribution of angular separations between estimated and input positions. The dashed vertical line denotes the *Planck* pixel size.

expected completeness drop-off. 20 candidate clusters were chosen from the sub-sample of cosmoOWLS clusters selected by the mass cuts discussed in Sect. 4.1, based on their dynamical state. The ten clusters in the sub-sample with the highest kinetic-to-thermal energy ratio within θ_{500} constituted our "disturbed" sample, while the "regular" sample comprised the ten clusters with the lowest kinetic-to-thermal energy ratio within θ_{500}. These clusters were injected 200 times, randomly distributed across the sky. We also created simulations injecting symmetric clusters with the UPP with the same parameters and locations as the hydrodynamic projections. In all cases, the signals were convolved with Gaussian beams.

The completeness for regular, disturbed and UPP clusters is shown for the union catalogue in the top panel of Fig. 10. There are no significant differences between the completeness functions for the regular and disturbed clusters. Both sets of hydrodynamic clusters show a slight widening effect in the completeness, caused by the variation in the effective pressure profile away from the UPP assumed for extraction (the same effect as discussed in Sect. 4.2).

Morphology has a clear impact on the estimation of cluster position. The bottom panel of Fig. 10 shows the cumulative distribution of angular separation between union and input positions for the regular, disturbed and UPP clusters. The disturbed clusters show a significant reduction in positional accuracy. Part of this is physical in origin. The cluster centres were defined here as the position of the "most-bound particle", which traces the minimum of the gravitational potential and is almost always coincident with the brightest central galaxy. For merging clusters this position can be significantly offset from the centre of the peak of the SZ distribution. A matching radius of 10 arcmin, which is used in Sect. 7, ensures correct identification of detected and injected positions.

4.6. Reliability

The statistical reliability is the probability that a detection with given detection characteristics is a real cluster. We determine the reliability using simulations of the *Planck* data. Clusters are injected following the prescription in Sect. 4.1, except that the

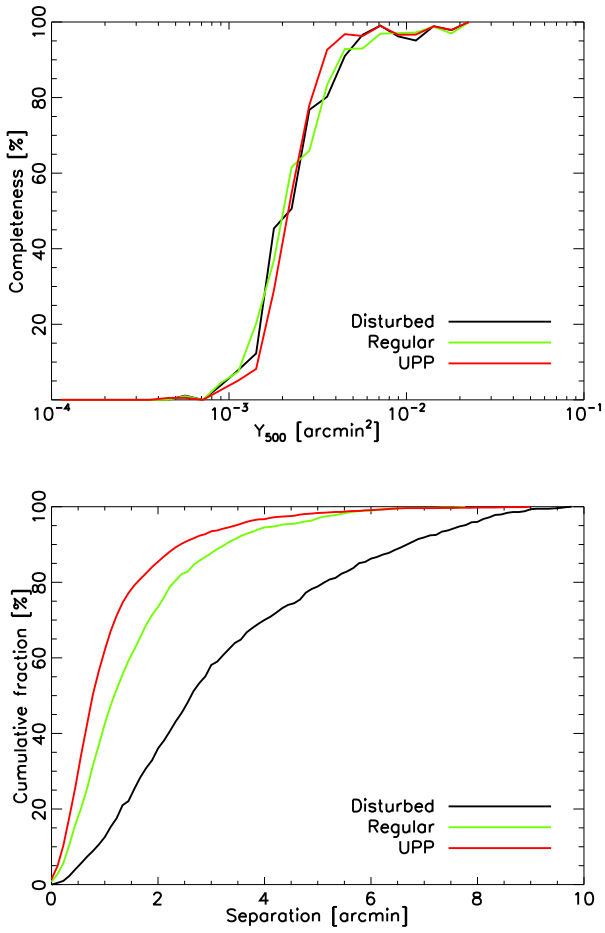

Fig. 10. Impact of cluster morphology on the completeness (*top panel*) and position estimates (*bottom panel*) for resolved clusters. The simulated clusters are all injected with $\theta_{500} = 20'$, and all curves are for the union catalogue. Cluster morphology has no impact on the completeness, but a significant impact on the position estimation.

clusters are injected such that cluster masses and redshifts are drawn from a Tinker et al. (2008) mass function and converted into the observable parameters (Y_{500}, θ_{500}) using the *Planck* ESZ Y_{500}–M_{500} scaling relation (Planck Collaboration X 2011). The other components of the simulations are taken from FFP8 simulation ensemble (Planck Collaboration XII 2016). The components include a model of Galactic diffuse emission, with thermal dust (including some emission from cold-clumps), spinning dust, synchrotron and CO emission, and extra-galactic emission from the far IR background. The diffuse components are co-added to a set of Monte Carlo realizations of CMB and instrumental noise. In addition to the cluster signal, we also inject point sources drawn from a multi-frequency model from the *Planck* sky model (Planck Collaboration XII 2016). These point sources are mock detected, using completeness information from the PCCS2 (Planck Collaboration XXVI 2016), and harmonically infilled using the same process as for the real maps prior to SZ detection. This leaves a realistic population of residual sources in the maps. After detection, candidates that lie within the simulated expanded source mask, or which match with the cold-core or IR source catalogues from the real data, have their S/N values set to zero.

Figure 11 shows the reliability as a function of S/N for the union and intersection samples across the whole survey area and

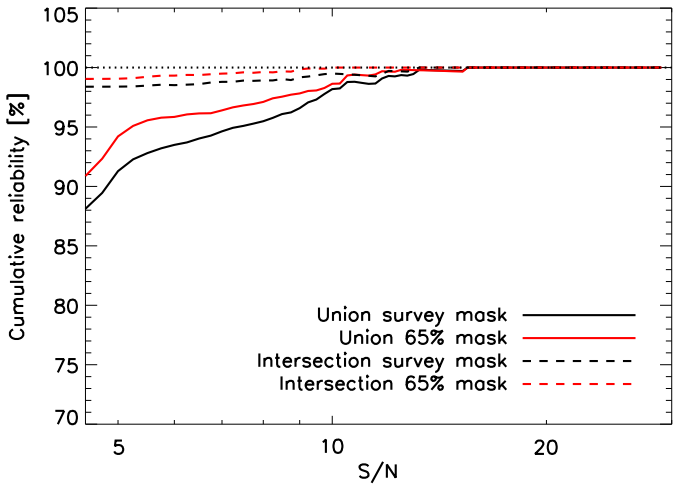

Fig. 11. Cumulative reliability as a function of S/N.

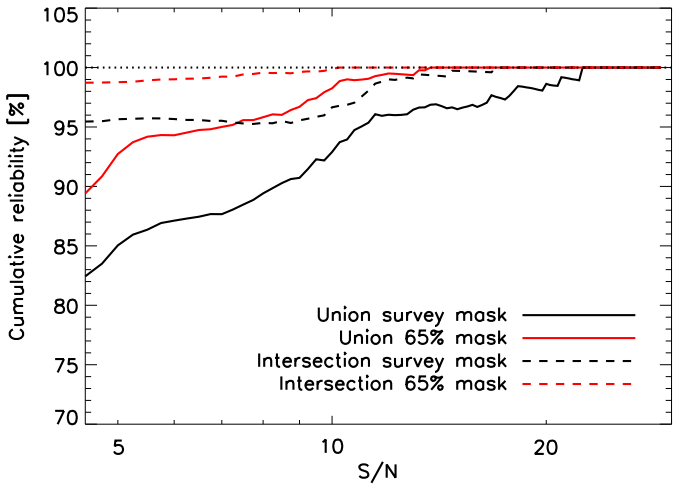

Fig. 12. Lower limits on the catalogue reliability, estimated by combining the reliability simulations with the Q_NEURAL information (see text).

outside the 65% Galactic mask used to define the cosmology samples. Relative to the PSZ1, the reliability of the union sample has improved by 5%, the lower noise levels have revealed more "real" simulated clusters than spurious detections. As was the case with the PSZ1, the reliability is improved significantly by removing more of the Galactic plane, where diffuse and compact Galactic emission induces extra spurious detections.

4.7. Neural network quality assessment

We supplement the simulation-based reliability assessment with an a posteriori assessment using an artificial neural-network. The construction, training, and validation of the neural network is discussed fully in Aghanim et al. (2015). The network was trained on nominal mission *Planck* maps, with a training set composed of three elements: the positions of confirmed clusters in the PSZ1 as examples of good cluster signal; the positions of PCCS IR and radio sources as examples of point-source induced detections; and random positions on the sky as examples of noise-induced detections. We provide for each detection a neural network quality flag, $Q\_\mathrm{NEURAL} = 1 - Q_\mathrm{bad}$, following the definitions in Aghanim et al. (2015), who also tested the network on the unconfirmed detections in the PSZ1. They showed that this flag definition separates the high quality detections from the low quality detections, as validated by the PSZ1 external validation process, such that Q_NEURAL < 0.4 identifies low-reliability detections with a high degree of success.

459 of the 1961 raw detections possess Q_NEURAL < 0.4 and may be considered low-reliability. This sample is highly correlated with the IR_FLAG, 294 detections being in common. After removal of IR spurious candidates identified by the IR_FLAG, as discussed in Sect. 3.2, we retain 171 detections with bad Q_NEURAL, of which 28 are confirmed clusters. This leaves 143 unconfirmed detections considered likely to be spurious by the neural network.

The Q_NEURAL flag is sensitive to IR induced spurious detections. The detections with low Q_NEURAL quality flag are clustered at low Galactic latitudes and at low to intermediate S/N. This clustering is not seen for realization-unique spurious detections in the reliability simulations, which are identifiable as noise-induced. The reliability simulations underestimate the IR spurious populations relative to the Q_NEURAL flag. Conversely, the neural network flag by construction does not target noise-induced spurious detections: Q_bad is the parameter trained to indicate IR-induced spurious sources. The neural network flag also has some sensitivity to the noise realization and amplitude in the data; the assessment is different to that applied to the nominal mission maps in Planck Collaboration XXXII 2015.

To place a lower limit on the catalogue reliability, we combine the Q_NEURAL information with the noise-induced spurious detections from the reliability simulations. For each reliability simulation realization, we remove the simulated IR-spurious detections, which can be identified either as induced by the FFP8 dust component, and thus present in multiple realizations, or as induced by injected IR point sources. We replace these spurious counts with the unconfirmed low Q_NEURAL counts, smoothed so as to remove the steps due to small number statistics.

The combined lower limit of the reliability is shown in Fig. 12. The lower limit tracks the simulation reliability well outside the 65% Galactic dust mask. For the whole survey region, the lower limit is typically 6% lower than the simulation estimate, due either to over-sensitivity of the neural network to dusty foregrounds, or shortcomings in the FFP8 Galactic dust component.

5. Parameter estimates

The SZ survey observable is the integrated Comptonization parameter, Y_SZ. As was the case for the PSZ1, each of the extraction codes has an associated parameter estimation code that evaluates, for each detection, the two dimensional posterior for the integrated Comptonization within the radius $5R_{500}$, Y_{5R500}, and the scale radius of the GNFW pressure θ_S. The radius $5R_{500}$ is chosen because it provides nearly unbiased (to within a few percent) estimates of the total integrated Comptonization parameter, while being small enough that confusion effects from nearby structures are negligible.

We provide these posteriors for each object and for each code, and also provide Y_{5R500} in the union catalogue, defined as the expected value of the Y_{5R500} marginal distribution for the reference detection (the posterior from the code that supplied the union position and S/N).

Below we also discuss the intricacies of converting the posteriors to the widely used X-ray parameters Y_{500} and θ_{500}.

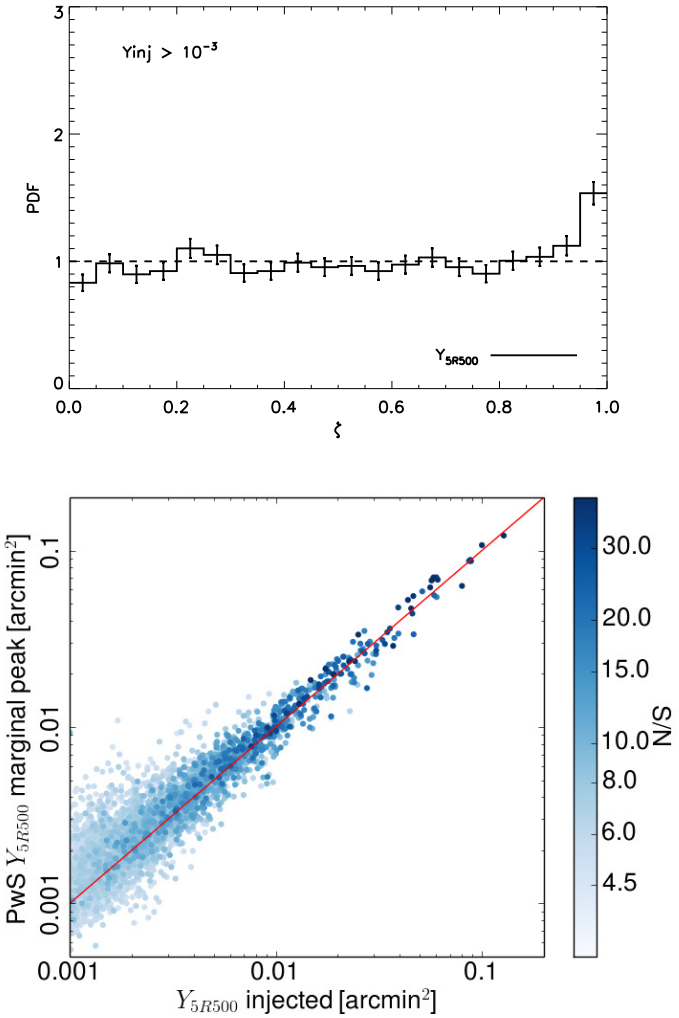

Fig. 13. *Top*: results of the posterior validation for Y_{5R500}. The histogram of the posterior probability, ζ, bounded by the true Y_{5R500} parameter, is almost uniformly distributed, except for a small excess in the tails of the posteriors, at $\zeta > 0.95$. The histogram has been normalised by the expected counts in each ζ bin. *Bottom:* comparison of recovered peak Y_{5R500} to the injected Y_{5R500}. The estimates are unbiased, though asymmetrically scattered, with a scatter that decreases as S/N increases.

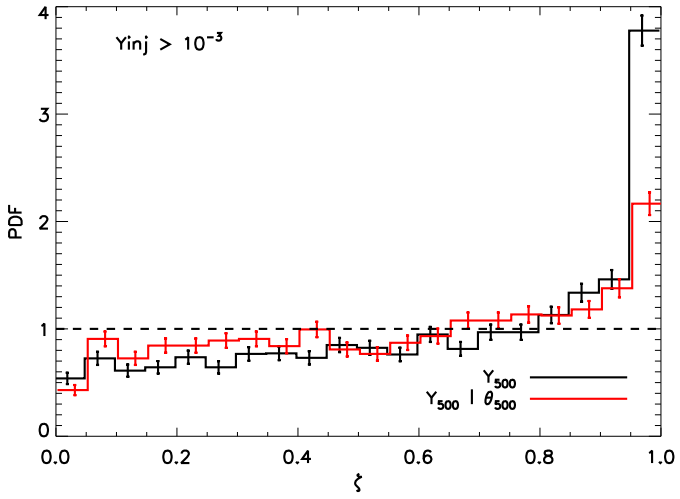

Fig. 14. Bounded probability histograms, as in the top panel of Fig. 13, but for the converted $p(Y_{500})$ marginal and $p(Y_{500}|\theta_{500})$ sliced posteriors. The values of Y_{500} that we injected were all $>10^{-3}$ arcmin^2.

5.1. Y_{5R500} estimates

To validate the Y_{5R500} estimates, we apply the posterior validation process introduced in Harrison et al. (2015) to the Y_{5R500} marginal distributions. In brief, this process involves simulating clusters embedded in the *Planck* maps and evaluating the (Y, θ) posteriors for each (detected) injected cluster. For each posterior, we determine the posterior probability, ζ, bounded by the contour on which the real underlying cluster parameters lie. If the posteriors are unbiased, the distribution of this bounded probability should be uniformly distributed between zero and one.

This process allows us to include several effects that violate the assumptions of the statistical model used to estimate the posteriors. Firstly, by injecting sources into real sky maps, we include non-Gaussian contributions to the noise on the multi-frequency matched-filtered maps that come from Galactic diffuse foregrounds and residual point sources. Secondly, we include violations of the "signal" model that come from discrepancies between the cluster pressure profile and the UPP assumed for parameter estimation, and from position dependent and asymmetric effective beams that vary from the constant Gaussian beams assumed for estimation. The clusters are injected using the process discussed in Sect. 4.1, drawing injected pressure profiles from the set of cosmo-OWLs simulated profiles.

The top panel of Fig. 13 shows the histogram of ζ for the PwS Y_{5R500} marginals. The distribution is flat, except for a small excess in the 0.95–1.0 bin, which indicates a small excess of outliers beyond the 95% confidence region (in this case 52% more than statistically expected). This suggests that the posteriors are nearly unbiased, despite the real-world complications added to the simulations. Note that we have considered only posteriors where the injected $Y_{5R500} > 0.001$ arcmin^2, a cut that removes the population effects of Eddington bias from consideration; we focus here on the robustness of the underlying cluster model.

The bottom panel of Fig. 13 shows the peak recovery from the PwS Y_{5R500} marginals compared to the true injected values. The peak estimates are unbiased relative to the injected parameters: a regression analysis of the peak estimates gives a slope of unity and a bias of 2.6%.

5.2. Conversion to Y_{500}

The (Y_{5R500}, θ_S) estimates can be converted into (Y_{500}, θ_{500}) estimates using conversion coefficients derived from the UPP model that was assumed for extraction. However, when the underlying pressure distribution deviates from this model, the conversion is no longer guaranteed to accurately recover the underlying (Y_{500}, θ_{500}) parameters; variation of the pressure profile can induce extra scatter and bias in the extrapolation.

We demonstrate this by applying the posterior validation process to the Y_{500} posteriors, defined as the Y_{5R500} posteriors scaled with the UPP conversion coefficient, as estimated from injected clusters whose pressure profiles are drawn from the cosmoOWLS pressure profile ensemble. We validate posteriors for Y_{500} calculated in two ways: firstly by marginalizing over the θ_{500} parameter, referred to in previous publications as "Y blind"; and secondly by slicing the (Y_{500}, θ_{500}) posteriors at the true value of θ_{500}, equivalent to applying an accurate, externally measured delta-function radius prior.

Figure 14 shows the bounded probability histograms for the two Y_{500} posteriors and Fig. 15 shows the scatter of the peak

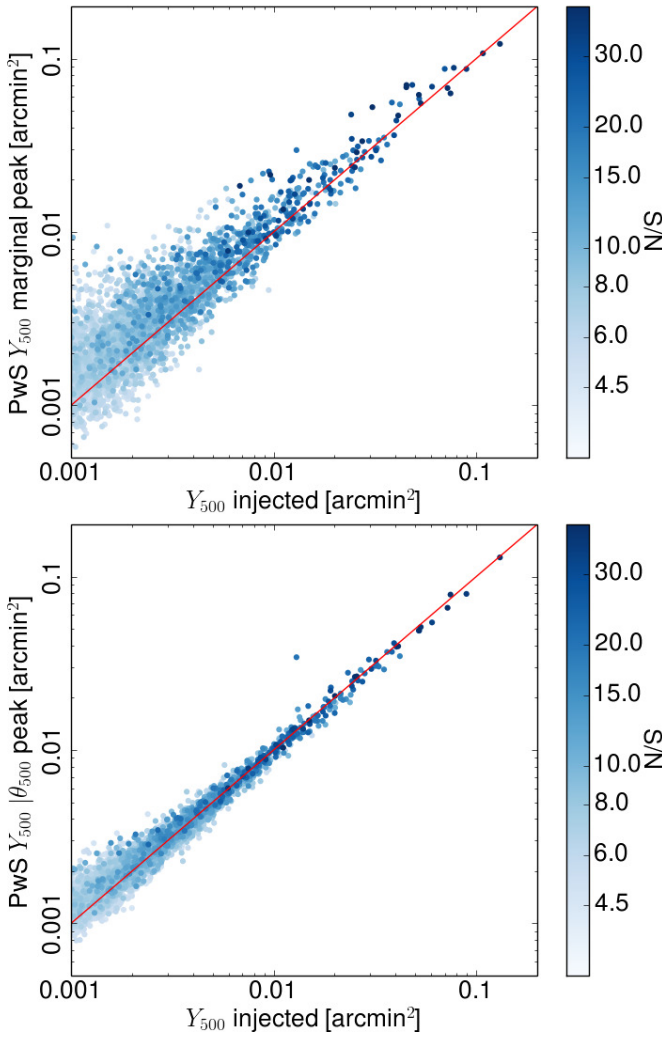

Fig. 15. Scatter of the recovered estimates of Y_{500} with the input Y_{500}. *Top*: for the marginalised Y_{500} posterior, "Y blind". *Bottom*: for the sliced posterior $p(Y_{500}|\theta_{500})$, assuming an accurate radius prior.

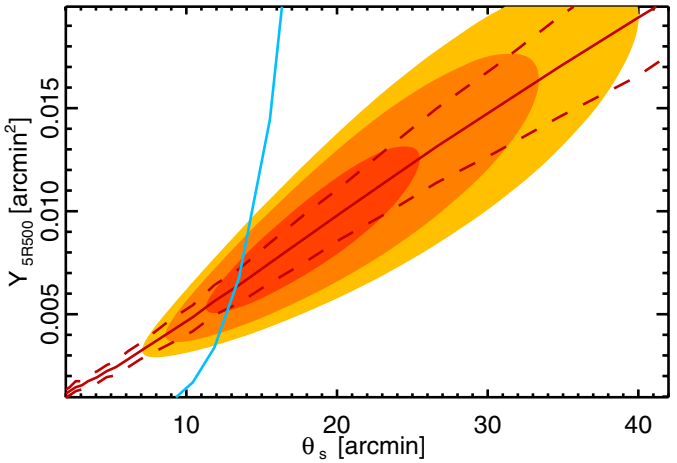

Fig. 16. Illustration of the posterior probability contours in the Y_{5R500}–θ_s plane for a cluster detected by *Planck*. The contours show the 68, 95 and 99% confidence levels. The red continuous line shows the ridge line of the contours, while the dashed lines are the $\pm 1\sigma$ probability value at each θ_S. The cyan line is the expected relation from Arnaud et al. (in prep.) at a given redshift.

of the posteriors with the input values of Y_{500}. The marginal Y_{500} posteriors are poor, with histograms skewed towards the tails of the distribution and large numbers of $>2\sigma$ outliers. The scatter plot reveals the peak estimates to possess a large scatter and to be systematically biased high by 16%. In contrast, the peak $p(Y_{500}|\theta_{500})$ estimates have much better accuracy and precision and are distributed around the input values with low scatter and a bias of −2%. The bounded probability histogram of $p(Y_{500}|\theta_{500})$ shows that while there is a noticeable excess of detections in the wings, the posteriors are reasonably robust. If the posteriors were Gaussian, the skewness of the $p(Y_{500}|\theta_{500})$ histogram towards the tails would be consistent with an underestimate of the Gaussian standard deviation of 21%.

We therefore recommend that, to estimate Y_{500} accurately from *Planck* posteriors, prior information be used to break the (Y_{500}, θ_{500}) degeneracy. However, we note that the uncertainties on such Y_{500} estimates will be slightly underestimated.

5.3. Mass and Y_{500} estimates using scaling priors

The key quantity which can be derived from SZ observables is the total mass of the detected clusters within a given overdensity (we used $\Delta = 500$). To calculate the mass from *Planck* data it is necessary to break the size-flux degeneracy by providing prior information, as outlined in the previous section. We used an approach based on Arnaud et al. (in prep.), where the prior information is an expected function relating Y_{500} to θ_{500} that we intersect with the posterior contours. We obtained this relation by combining the definition of M_{500} (see Eq. (9) in Planck Collaboration XX 2014, connecting M_{500} to θ_{500}, for a given redshift z) with the scaling relation Y_{500}–M_{500} found in Planck Collaboration XX (2014). A similar approach was also used in Planck Collaboration XXIX (2014), but now we use the full posterior contours to associate errors to the mass value.

We illustrate our method in Fig. 16. At any fixed value of θ_S, we study the probability distribution and derive the Y_{5R500} associated to the maximum probability, i.e. the ridge line of the contours (red continous line in Fig. 16). We also derive the Y_{5R500} limits enclosing a 68% probability and use them to define an upper and lower degeneracy curve (dashed lines). From the intersection of these three curves with the expected function, we derive the M_{SZ} estimate and its 1σ errors, by converting Y_{5R500} to Y_{500} and then applying the Y_{500}–M_{500} scaling relation prior at the redshift of the counterpart.

M_{SZ} can be viewed as the hydrostatic mass expected for a cluster consistent with the assumed scaling relation, at a given redshift and given the *Planck*(Y–θ) posterior information. We find that this measure agrees with external X-ray and optical data with low scatter (see Sect. 7). For each M_{SZ} measurement, the corresponding Y_{500} from the scaling relation prior can be calculated by applying the relation.

We underline that the errors bars calculated from this method consider only the statistical uncertainties in the contours, not the uncertainties on the pressure profile nor the errors and scatter in the Y_{500}–M_{500} scaling relation, and should thus be considered a lower limit to the real uncertainties on the mass.

We use the masses for the confirmation of candidate counterparts (see Sect. 7) and we provide them, along with their errors, in the PSZ2 catalogue, for all detections with confirmed redshift. We compared them with the masses provided in PSZ1 for the detections where the associated counterpart (and thus the redshift value) has not changed in the new release (see Appendix B).

Table 3. Results of fits between S/N from the PSZ1 and PSZ2, using the fitting function in Eq. (6).

s_1	s_2	A	α	σ
PSZ2	PSZ1	0.76 ± 0.08	0.72 ± 0.01	0.53 ± 0.02

Notes. The assumed correlation of the uncertainties of s_1 and s_2 was 0.72.

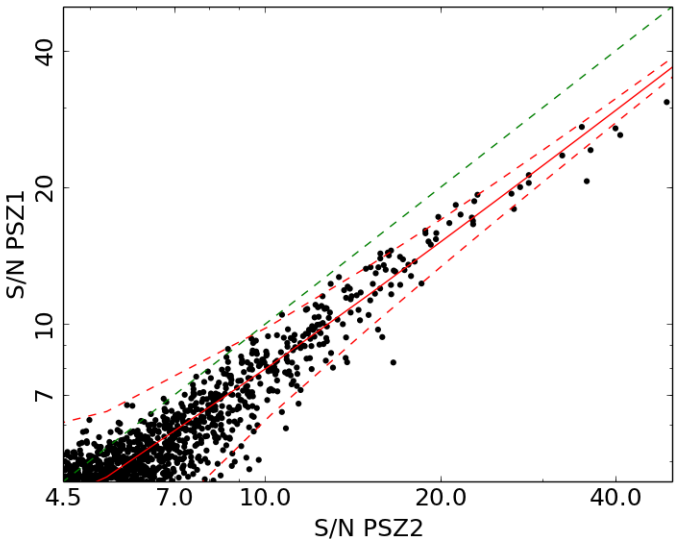

Fig. 17. Comparison of S/N values for common PSZ1 and PSZ2 detections. The best fit relation is plotted in red, with 2σ scatter shown by dashed red lines. The green dashed line denotes the 1-to-1 relation.

We find very good agreement between the two values, which are consistent within the error bars over the whole mass range.

In the individual catalogues, we provide for all entries an array of masses as a function of redshift, $M_{\rm SZ}(z)$, which we obtained by intersecting the degeneracy curves with the expected function for different redshift values, from $z = 0$ to $z = 1$. The aim of this function is to provide a useful tool for counterpart searches: once a candidate counterpart is identified, it is sufficient to interpolate the $M_{\rm SZ}(z)$ curve at the counterpart redshift to estimate its mass.

6. Consistency with the PSZ1

The extra data available in the construction of the PSZ2 improves the detection S/N and reduces statistical errors in the parameter and location estimates. Here we assess the consistency between the two catalogues, given the matching scheme discussed in Sect. 7.1.

6.1. Signal-to-noise

We fit the relation between S/N for common PSZ1 and PSZ2 clusters using the approach and model discussed in Sect. 3.4. For the PSZ1 and PSZ2, the likelihoods for s_1 and s_2 have a strong covariance, since more than half of the PSZ2 observations were used in the construction of the PSZ1. We therefore assign a covariance of 0.72 between the two S/N estimates, as is appropriate for Gaussian errors sharing 53% of the data. As the errors are not truly Gaussian, we allow for an intrinsic scatter between the S/N estimates to encapsulate any unmodelled component of the S/N fluctuation.

The consistency of the S/N estimates between the PSZ1 and PSZ2 are shown in Fig. 17 and the best fitting model is shown in Table 3. Detections with PSZ2 $S/N > 20$ are affected by changes in the `MMF3` S/N definition. For the PSZ1, the empirical standard deviation of the filtered patches was used to define the S/N in this regime, while the theoretical standard deviation of Melin et al. (2006) was used for lower S/N. `MMF3` now uses the theoretical standard deviation for all S/N, consistent with the ESZ and the definitions in the other detection codes. For this reason, the best fit model ignores detections at $S/N > 20$ in either catalogue. The `MMF3` S/N show a flat improvement relative to the ESZ S/N (which was produced solely by `MMF3`), consistent with the reduced noise in the maps.

If the Compton-Y errors are entirely Gaussian in their behaviour, we should expect the S/N to increase by 37% between the PSZ1 and PSZ2, i.e., $\alpha = 0.73$. This is consistent within 1σ with the fit, which describes the S/N behaviour well to $S/N < 20$.

6.2. Position estimation

The distribution of angular separations between the PSZ2 and PSZ1 position estimates is shown in Fig. 18. Of the common detections, 80% of the PSZ2 positions lie within one *Planck* map pixel width, 1.7 arcmin, of the PSZ1 position. `MMF3` does not allow for sub-pixel positioning, so if the `MMF3` position was used for the union in both the PSZ1 or PSZ2, the angular separation will be a multiple of the pixel width. This is evident in the cumulative distribution of angular separations as discontinuities at 0, 1, and $\sqrt{2}$ pixel widths.

We also compare the position discrepancy between the SZ detection and the X-ray centres from the MCXC (Piffaretti et al. 2011). The bottom panel of Fig. 18 shows the distributions of these angular separations for the PSZ2 and PSZ1. The distributions are calculated from the full MCXC match for each catalogue: the PSZ2 includes 124 new detections. The PSZ2 position estimates are clearly closer to the X-ray centres than the PSZ1; for the PSZ1, the 67% error radius is 1.85 arcmin, while for the PSZ2 this reduces to 1.6 arcmin. The expected statistical improvement of the position discrepancy due to the new *Planck* data is a reduction to 1.35 arcmin. This suggests *Planck* positional uncertainty is not the only contributor to this offset. For example a physical offset between X-ray and SZ centroids is possible, with offsets of up to arcminute scales observed in comparisons of SZ and X-ray data for dynamically disturbed clusters (Planck Collaboration Int. IV 2013; Reichardt et al. 2013).

6.3. Missing PSZ1 detections

The PSZ1 produced 1227 union detections. While the numbers of detections has increased by 35% in the PSZ2 to 1653, the number of common detections is 936, so 291 (23.7%) of the PSZ1 detections disappear. The high-purity intersection sample loses 44 detections, of which 20 are lost entirely, and 24 drop out of the intersection after one or two codes failed to detect them. In this section, we discuss these missing detections. Table E.1 details each of the missing detections and provides an explanation for why each is missing.

The first type of missing detection are those that fall under the new survey mask, due to the increase in the number of point sources being masked. The masked areas are pre-processed with harmonic infilling to prevent spurious detections induced by Fourier ringing. The increase of the mask area is driven

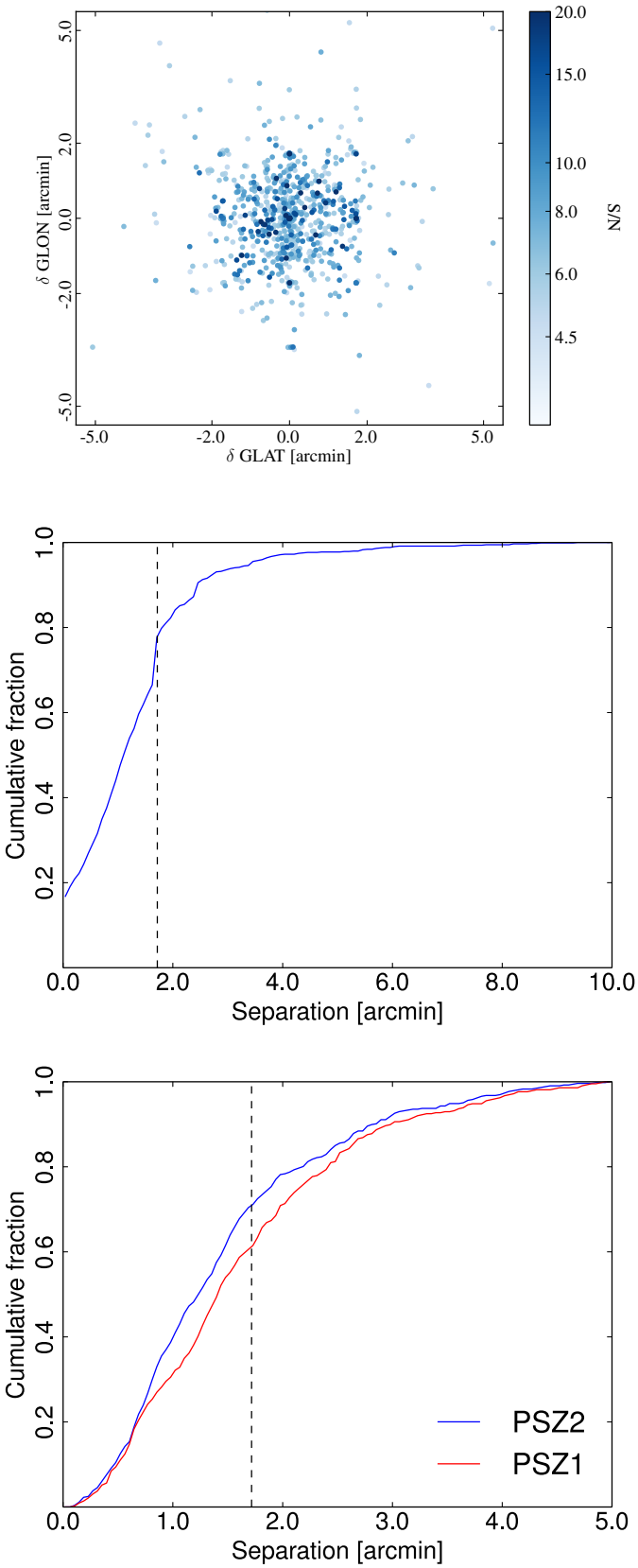

Fig. 18. *Top*: separation between PSZ2 and PSZ1 positions for common detections. *Middle*: cumulative distribution of the angular separation between PSZ1 and PSZ2 positions, with the *Planck* pixel width indicated by a dashed vertical line. *Bottom*: cumulative distributions of angular separation to MCXC X-ray centres, for all PSZ1 and PSZ2 MCXC matches. The vertical dashed line denotes the *Planck* `Healpix` pixel size.

by S/N improvements for IR sources in the high frequency channels. While the increase in the masked area is small (0.1% of the sky), the correlation between IR point sources and galaxy clusters leads to a larger percentage of detections being masked. In the PSZ1, these detections were contaminated by point source emission, but the emission was just beneath the point source masking threshold. 21 PSZ1 union detections fall under the new mask. Of these, three were confirmed clusters, none received the highest validation quality flag of 1 (denoting probable clusters) in the PSZ1 validation process[5], four received the intermediate validation quality flag 2, and 14 received the lowest validation quality flag of 3 (denoting probable spurious detections).

The second type of missing detection is one that has a matching detection in the full-mission data, but where the detection was rejected either by the infra-red spurious cuts or by `PwS` internal consistency cuts, both of which are discussed in Sect. 3.2. The IR cuts are responsible for removing 33 unconfirmed PSZ1 detections, of which six were in the intersection sample. In the PSZ1 validation process, none of these received validation quality flag of 1, seven received quality flag 2, and 26 received quality flag 3. These were all $S/N < 7$ detections. Five detections were lost because `PwS` was the only detecting code in the PSZ2 and they failed `PwS` consistency criteria, with two of these being confirmed clusters.

The final class contains the majority (232) of the missing detections. These are low-significance detections close to the PSZ1 threshold that have downward-fluctuated with the full mission data and are now beneath the PSZ2 threshold. This occurs for some detections despite the fact that the S/N improves for most. The top panel of Fig. 19 shows the PSZ1 S/N distribution of the downward-fluctuated detections. These were weak detections: 87% were within 0.5σ of the detection threshold; and 82% of them were single-code detections. While many of these may be spurious detections, 81 confirmed clusters have been lost. 61 of these were single-code detections and 70 of them were within 0.5σ of the threshold. Based on *Planck* data alone, these clusters were weak SZ detections and were likely to be Eddington biased above the threshold in the PSZ1. We have estimated the S/N for these lost PSZ1 detections in the full-mission maps using `PwS` in a non-blind analysis at the PSZ1 positions. Figure 20 shows the distribution of these non-blind S/N; for most, an apparently significant signal still exists in the maps, but it is now too weak to exceed the detection threshold, typically lying in the range $2 < S/N < 4$. The non-blind S/N for this category is shown per detection in Table E.1. Two detections have a non-blind S/N above the selection threshold. For these detections, the noise level for the non-blind analysis (centred on the PSZ1 location) was lower than for any of the patches in the mosaic used for the cluster detection.

To verify that this sample of missing detections is consistent with the change in data, we simulated the transition from the PSZ1 to the PSZ2 using FFP8 half-mission noise realizations to approximate the nominal mission; this produces a pair of data sets with appropriately correlated noise characteristics. A common sample of clusters and point sources were injected into the simulations and the full pipeline was applied to construct catalogues from both simulated data sets. The simulations produced

[5] The PSZ1 validation process produced three quality flags for unconfirmed clusters. These were based on a combination of SZ signal quality, X-ray signal in the RASS maps, and IR signal in the WISE maps. Class 1 candidates satisfied good quality in all three measures and were high reliability candidates. Class 2 satisfied at least one measure with good quality, while Class 3 failed all three measures and so were considered probably spurious.

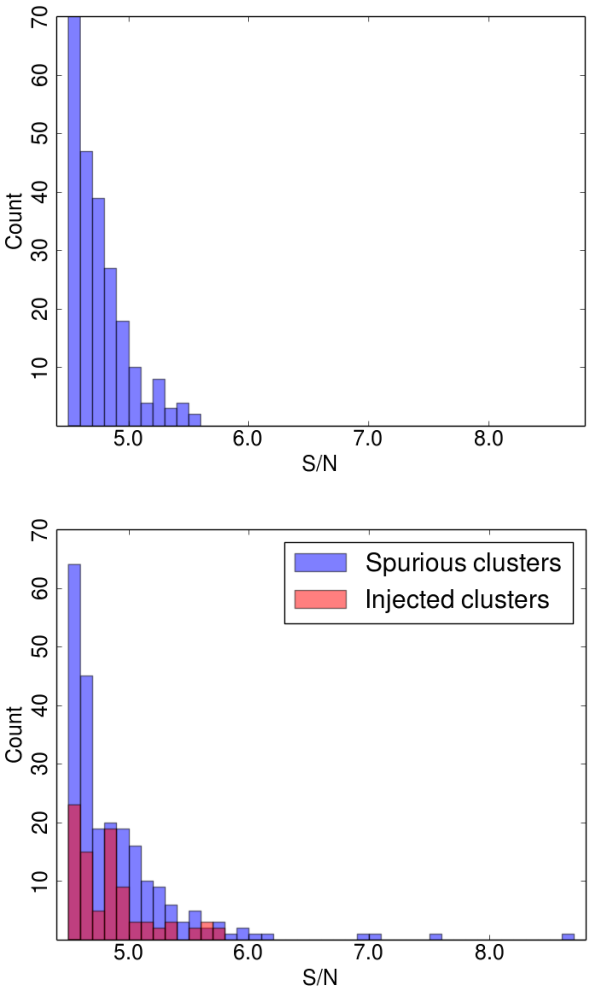

Fig. 19. Distribution of S/N for missing nominal mission detections, lost due to downward fluctuation of the S/N rather than because of spurious rejection cuts or changes in the survey mask. *Top*: detections lost from the PSZ1. *Bottom*: detections lost in simulations of the transition from the nominal to full mission.

a total decrease of 353 detections, of which 24 were lost due to the expansion of the point source mask, ten were lost due to changes to the PwS spurious rejection criteria, and 319 were lost due to downward fluctuation of the S/N beneath the detection threshold.

The S/N distribution of the latter group is shown in the bottom panel of Fig. 19. 75% lie within 0.5σ of the detection threshold and 85% were single-code detections. While this group was primarily composed of 230 spurious detections, 89 injected clusters were lost. The loss of these injected clusters illustrates that, as a statistical process, cluster detection is dependent on the realization of the noise in the filtered patch-maps and we should expect that substantial numbers of confirmed but weak cluster detections will be lost due to noise fluctuations.

These simulations over-estimate the loss-rate of nominal mission detections. This may be due in part to unsimulated changes in the sample selection applied to the real data. For example, we were unable to simulate systematic changes in the IR spurious rejection that may (had they been incorporated) have resulted in some spurious detections from the nominal mission simulation being cut from the comparison.

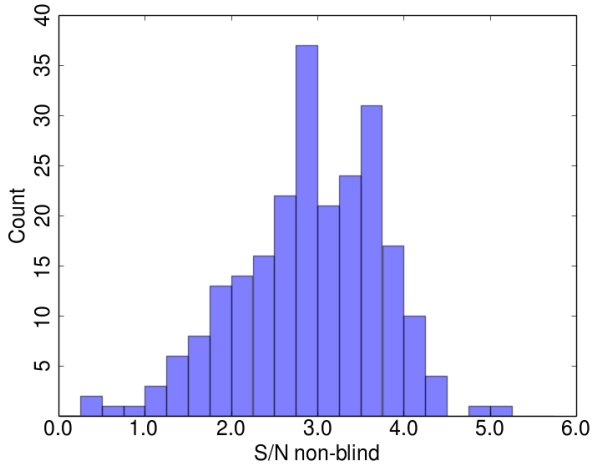

Fig. 20. Non-blind PwS S/N for the SZ signal at the location of missing PSZ1 detections that were not masked out or cut for IR contamination.

6.4. Compton Y estimates

The Compton Y_{5R500} estimates from each code are compared to the PSZ1 estimates in Fig. 21. The Y_{5R500} estimates that we consider here are the mean estimates of the Y_{5R500} marginal posteriors, having been marginalized over the scale radius θ_s.

The best-fit relations between the PSZ2 and PSZ1 values for each code are shown in Table 4. These were fit using a similar procedure to the S/N estimates discussed in the previous section. We assume a log-linear relation between the estimates of the form

$$\log \frac{Y_2}{Y_{\rm piv}} = A + \alpha \log \frac{Y_1}{Y_{\rm piv}}, \tag{8}$$

with a log-normal intrinsic scatter $\sigma_{\rm int}$ and $Y_{\rm piv} = 3 \times 10^{-4}$ arcmin^2. We again assume a bivariate Gaussian likelihood for the estimates, with a correlation of 0.72.

Figure 21 compares the Y_{5R500} estimates for each of the three detection codes. High S/N detections have more consistent estimates of Y_{5R500}. For MMF3, detections at $S/N > 20$ are significantly changed due to the changes in the treatment of these detections discussed in Appendix C; these points are excluded from the fit to the relation. The scatter on the high S/N estimates is determined by the robustness of the noise power spectrum estimation to small changes in the data. For PwS, the high S/N estimates have particularly low scatter, due to the robust nature of the noise estimation that accounts for Compton-Y "noise" contributed by neighbouring clusters.

The low S/N detections show systematic deviations for each of the codes. For the MMFs, these are caused by the correction of PSZ1 Eddington bias in the PSZ2 data, which is visible in Fig. 21 as clouds of faint points where the Y_{5R500} estimate decreases in the PSZ2. The opposite is the case for PwS estimates, where the faint detections show upward deviation in the PSZ2. This is caused by a change in the priors: for the PSZ1, PwS used a power-law prior in Y_{5R500}, which was replaced in the PSZ2 with the uninformative flat prior, since this produced more robust Y_{5R500} estimates in the posterior validation process discussed in the previous section. We have confirmed that PwS behaves in the same way as the MMFs when uninformative priors are used for both PSZ1 and PSZ2 parameter estimates (see the bottom right panel of Fig. 21).

To verify that the bias effects seen in Fig. 21 are within expectations, we extracted Y_{5R500} estimates from the half to

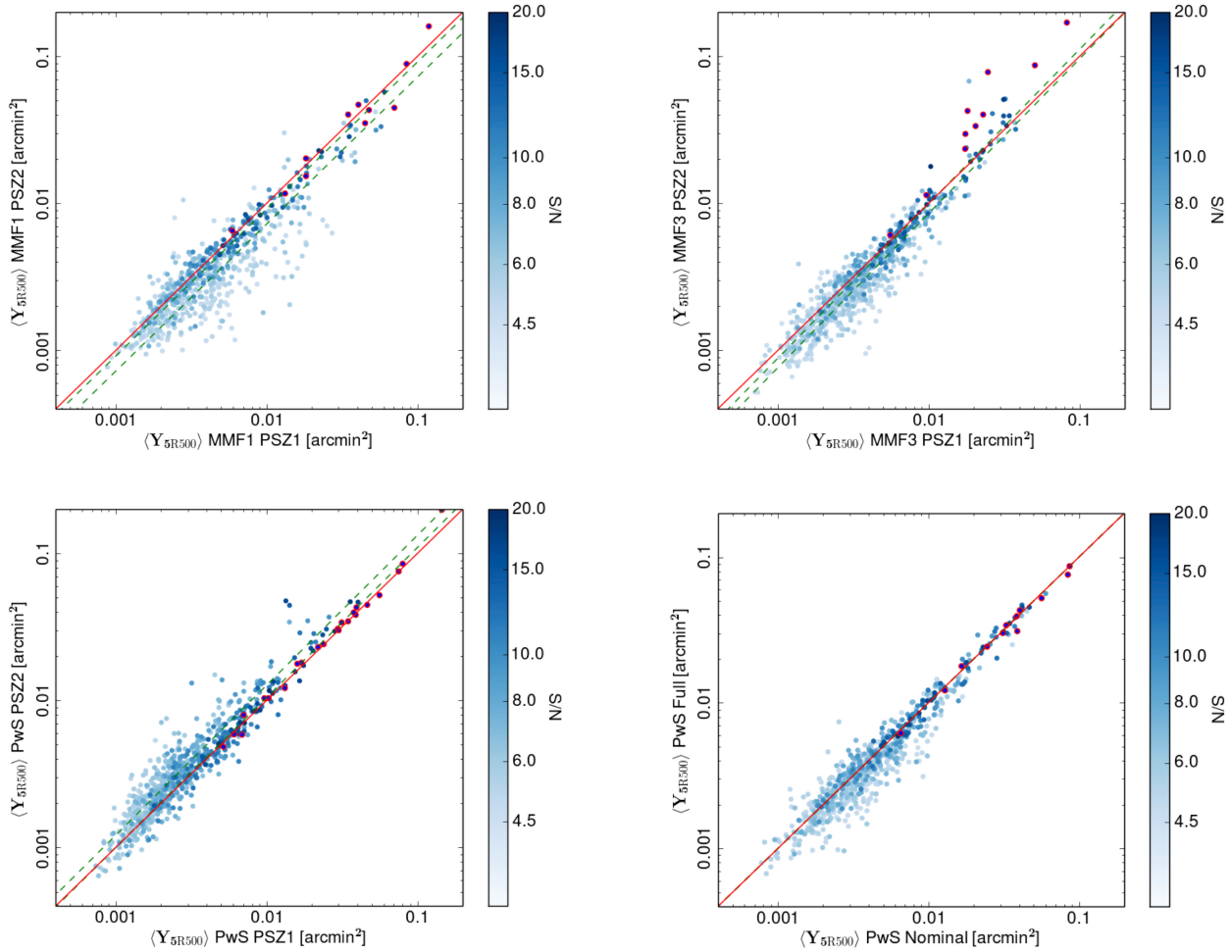

Fig. 21. Comparison of Y_{5R500} estimates from individual codes in the PSZ1 and PSZ2. The Y_{5R500} estimator is the mean of the $Y - \theta$ posteriors, marginalised over θ_S ("Y blind"). The circled red points denote sources with $S/N > 20$. The dashed green lines show the $1 - \sigma$ envelope of the best-fit relations shown in Table 4. `MMF1` estimates are shown *top left*, `MMF3` *top right*. `PwS` estimates are shown *bottom left*. The *bottom right panel* compares `PwS` estimates having re-analysed PSZ1 data using uninformative priors on Y_{5R500} and θ_S.

Table 4. Results of fits between Y_{5R500} from the PSZ1 and PSZ2, following Eq. (8).

Y_1	Y_2	A	α	$\sigma_{\rm int}$
PSZ1 `MMF1`	PSZ2 `MMF1`	-0.087 ± 0.006	1.00 ± 0.02	0.083 ± 0.003
PSZ1 `MMF3`	PSZ2 `MMF3`	-0.054 ± 0.002	1.05 ± 0.01	0.054 ± 0.003
PSZ1 `PwS`	PSZ2 `PwS`	0.056 ± 0.005	1.02 ± 0.01	0.068 ± 0.003

full-mission transition simulations described in Sect. 6.3. We confirm the same behaviour in these simulations as in the real data; namely low S/N detections from the MMFs show a correction of Eddington bias in the full mission, while `PwS` low S/N detections are affected by change from power-law to uninformative priors in the posterior estimation and are typically higher in the full mission.

7. Ancillary Information

7.1. Cross-match with PSZ1

We begin the search for counterparts by conducting a cross-match with the well-validated PSZ1. All matches within 5 arcmin of a PSZ1 detection are accepted as a true match. Both catalogues used this radius as the merging limit to define unique detections, both in the merge of Cartesian patch catalogues to form an all-sky catalogue and in the formation of the union. This step produced no non-unique matches between PSZ1 and PSZ2 locations.

Several of our detections are clear matches with PSZ1 detections at larger radii than this, so we consider matches out to 10 arcmin, as is the case with the X-ray and optical counterpart searches described below. This step produced 18 potential matches, two of which were non-unique. We apply a further condition to accept these high-separation matches, specifically that the PSZ2 S/N be greater than the PSZ1 S/N and that it is consistent with the S/N relation determined in Sect. 6.1. For the two non-unique matches, the nearer match was chosen both times and this match also better fits the S/N relation.

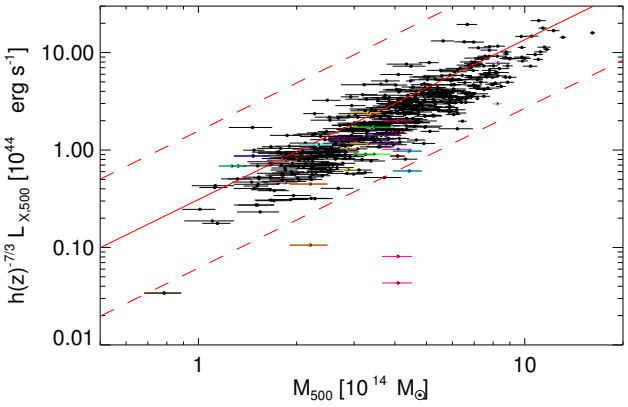

Fig. 22. Comparison of candidates associated with the MCXC catalogue and the expected $L_{X,500}-M_{500}$ scaling relation (red line). The parallel dashed lines identify the region of the plane within $2\sigma_{int}$ from the expected scaling relation, where σ_{int} is the logarithmic intrinsic scatter of the relation we used. Black points are confirmed MCXC associations, while magenta squares mark the associations discarded by the $L-M$ criterion. Pairs of coloured diamonds mark the two possible counterparts for objects with multiple associations.

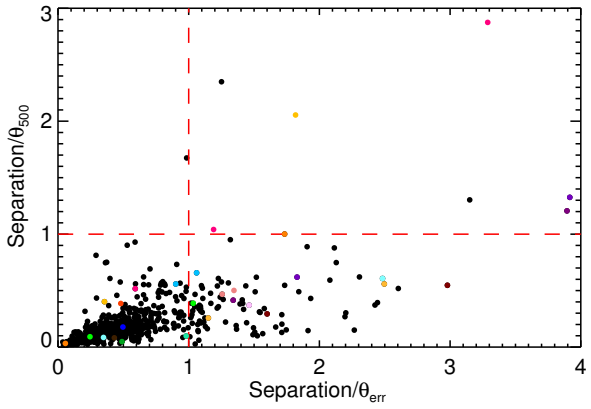

Fig. 23. Separation between the *Planck* and MCXC positions in terms of the positional uncertainty of the *Planck* detection and of the cluster R_{500}. The horizontal and vertical dashed lines mark our acceptance thresholds.

7.2. X-ray information

We use the Meta-Catalogue of X-ray detected Clusters of galaxies (MCXC, Piffaretti et al. 2011) for the association of *Planck* SZ candidates with known X-ray clusters, as was done in Planck Collaboration XXIX (2014). MCXC is based on the *ROSAT* All Sky Survey and is complemented with other serendipitous catalogues and with the *Einstein* Medium Sensitivity Survey. It includes 1743 clusters distributed over the whole sky and provides coordinates, redshifts, and X-ray luminosity measured within R_{500}, i.e. $L_{X,500}$. The association of *Planck* SZ candidates with MCXC clusters follows two steps: first a positional matching between the catalogues; then a verification of the association using the $L_{X,500}$-M_{500} relation (Pratt et al. 2009). In the first step, we looked for possible counterparts of *Planck* SZ candidates in the MCXC within a search radius of 10 arcmin around the *Planck* position. We found one counterpart for 537 candidates and multiple matches for another 16 objects. In the second step, we verified our associations by looking at their position in the $L_{X,500}$-M_{500} plane (Fig. 22). For the X-ray luminosity, we use the $L_{x,500}$ value provided in the MCXC, while we calculate the mass from our own data, as described in Sect. 5. In Fig. 22, we compare our results with the expected $L_{X,500}$-M_{500} relation (Piffaretti et al. 2011); we consider as good associations those whose position in the $L_{X,500}$-M_{500} does not differ from the expected one by more than twice the intrinsic scatter in the relation ($\sigma_{int} = 0.183$, Pratt et al. 2009). Based on this criterion we discarded the association with an MCXC cluster for two objects, PSZ2 G086.28+74.76 and PSZ2 G355.22-70.03, both new PSZ2 detections.

We performed a further check of the candidate counterparts by studying the separation between the *Planck* and MCXC positions. Indeed, the relatively large search radius (10 arcmin) may have led to spurious associations, which might have escaped our selection on the $L_{X,500}$-M_{500} relation. In Fig. 23, we compare the separation between the *Planck* and MCXC positions with two relevant angular scales: the positional uncertainty of the *Planck* detections θ_{err} (90% confidence level, provided in the catalogue); and the cluster size as quantified by θ_{500}[6]. Ideally, one would keep as good counterparts those systems where the angular separation is smaller than both θ_{500} and θ_{err} (lower left quadrant in Fig. 23), but this would lead to a large number of rejected matches, including many objects in the PSZ1. Therefore, we chose a less conservative criterion, and excluded only those associations where the separation is larger than both θ_{500} and θ_{err} (upper right quadrant in Fig. 23). We thus allow the separation to exceed θ_{500} if the MCXC counterpart falls within the *Planck* accuracy (upper left quadrant) and to exceed θ_{err} if it is smaller than the cluster expected size (lower right quadrant). We notice that the most deviant sources in the latter case (with $\theta > 2\theta_{500}$) are associated with nearby clusters ($z < 0.14$) with $\theta_{500} > 7$ arcmin, resolved by *Planck*. In this phase of the analysis, we thus discarded the three associations with PSZ2 G247.97+33.52, PSZ2 G212.93-54.04, and PSZ2 G209.79+10.23 in the upper right quadrant of Fig. 23; for these systems, the separations between the *Planck* and MCXC are always larger than 5 arcmin, which would correspond to a physical distance of around 1 Mpc at the redshifts of the MCXC objects (all at $z > 0.2$).

We also used the position in the $L_{X,500} - M_{500}$ plane and in the separation plane (Fig. 23) to select the most likely counterparts for the objects where two or more MCXC clusters are found within our search radius of 10 arcmin. For seven out of 16 objects, one counterpart does not match the criteria described above and we are thus left with only one good counterpart. For six *Planck* detections, both MCXC counterparts satisfy our requirements. We thus rank them based on their distance from the $L_{X,500}-M_{500}$ scaling relation and their separation in terms of θ_{500} and θ_{err}, and select as the most likely counterpart the one with smaller values for at least two out of three indicators. We provide details of the other possible counterparts in the Comments column of the catalogue . In two cases, the same MCXC cluster can be associated with two *Planck* detections and we used the procedure described above to select the most likely associations.

In the last step of our analysis, we checked our matching with MCXC with the matches made in the PSZ1 catalogue. In most cases the MCXC counterparts in the two catalogues coincide. We examined in detail the cases where, following our selection criteria, we would not have chosen the association with the

[6] We calculated θ_{500} from the mass proxy M_{500}, using the redshift of the MCXC counterpart.

MCXC counterpart which was chosen in PSZ1. This led to three corrections.

- PSZ2 G247.97+33.52 (PSZ1 index 842) association with RXCJ0956.4-1004 lies in the forbidden area in the separation plane. However, RXCJ0956.4-1004 (also known as A901) is a multi-component cluster (Bösch et al. 2013), and the PSZ2 position lies close to the position of one of the components. We thus decided to keep the association.
- PSZ2 G302.41+21.60(PSZ1 index 1054) and PSZ2 G332.29-23.57(PSZ1 index 1158) are both associated very low-redshift clusters (RXC J1248.7-4118 and RXC J1847.3-6320, both $z < 0.015$) which are marginal outliers in the $L - M$ plane. However, our mass proxy estimate may be less reliable for local objects due to the large cluster extent and we thus decided to keep these associations.

7.2.1. Comparison to $L - M$ relation

It is interesting to note in Fig. 22 that most points lie below the expected scaling relations of Pratt et al. (2009), although well within the intrinsic scatter. This means that clusters in our subsample are systematically under-luminous (by about 20%, or $-0.4\sigma_{\rm int}$) in X-rays at a given mass. We recall here that this subsample (the intersection of PSZ2 with MCXC) is not representative and thus cannot be quantitatively compared with a well defined representative sample such as REXCESS, for which the $L_{\rm X,500} - M_{500}$ relation was derived by Pratt et al. (2009). The systematic offset observed in Fig. 22 does not contradict the good agreement between X-ray predictions and *Planck* measurements found using a statistical approach in Planck Collaboration X (2011). It can be explained taking into account selection effects and the scatter in the $Y - L_{\rm X}$ scaling relation; when cutting in SZ S/N, clusters with a high SZ signal (and thus a high mass) for a given X-ray luminosity are preferentially selected. Another effect, which could also partly contribute to the offset in Fig. 22, is the presence of a cluster population with different X-ray properties in the PSZ2 sample; this will be discussed in Sect. 8.2.

7.3. Optical information

We benefit from a wealth of publicly available data over the northern sky, principally thanks to the Sloan Digital Sky Survey (SDSS, York et al. 2000), which covers most of the northern extragalactic sky with imaging in five optical bands (*ugriz*). A number of cluster catalogues have been extracted from these data using different finding algorithms (Koester et al. 2007; Hao et al. 2010; Wen et al. 2012). Among these, the `redMaPPer` catalogue (Rykoff et al. 2014), published since the PSZ1 release and containing many more clusters, has proven to be the most useful for identifying counterparts to *Planck* SZ sources. We also supplement `redMaPPer` with other optically information.

7.3.1. RedMAPPer

The `redMaPPer` algorithm detects clusters by looking for spatial over-densities of red-sequence galaxies. It provides accurate photometric redshift estimates for all sources, spectroscopic redshifts for the brightest central galaxy (BCG) when available, and a specific estimator of the optical richness, λ (defined fully in Rykoff et al. 2014). We used the proprietary `redMaPPer` catalogue (v5.10) provided by Rykoff et al. and containing over 400 000 objects.

In our procedure, detailed further in Bartlett et al. (in prep.), each *Planck* SZ source is first matched to a maximum of three `redMaPPer` clusters falling within a radius of 10 arcmin. They are subsequently ranked by richness and labeled first-, second-, and third-ranked matches. We then calculate the *Planck* mass proxy, $M_{\rm SZ}$, for each SZ source at the redshifts of its matched `redMaPPer` clusters. The best `redMaPPer` counterpart is selected based on cuts in angular separation and richness. The angular cuts incorporate both the *Planck* positional uncertainty and the physical extent of the cluster estimated from the calculated $M_{\rm SZ}$.

These angular criteria alone would leave multiple possible counterparts in many cases, given the high surface density of `redMaPPer` clusters. Any ambiguity is efficiently reduced by the richness cut, which is based on the existence of a well-defined relation between richness, λ, and $M_{\rm SZ}$. Such a relationship was established by Rozo et al. (2015) on the *Planck* 2013 SZ cluster catalogue and is expressed as

$$\langle \ln \lambda | M_{\rm SZ} \rangle = a + \alpha \ln\left(\frac{M_{\rm SZ}}{M_{\rm p}}\right), \tag{9}$$

with $a = 4.572 \pm 0.021$, $\alpha = 0.96 \pm 0.07$, and $M_{\rm p} = 5.23 \times 10^{14}\, M_{\odot}$. The measured dispersion at given $M_{\rm SZ}$ is $\sigma_{\ln\lambda} = 0.266 \pm 0.017$.

In Fig. 24 we compare the distribution of the first, second-, and third-ranked `redMaPPer` matches in the $\lambda - M_{\rm SZ}$ plane to this scaling relation. The quantity $\Delta_{\ln}\lambda \equiv [\ln(\lambda) - \langle \ln \lambda \rangle]/\sigma_{\ln\lambda}$ is the deviation of measured richness from the expected mean. We see that the first-ranked matches (in red) display a prominent peak at $\Delta_{\ln}\lambda = 0$, extending to $\pm 3\,\sigma_{\ln\lambda}$. This reaffirms the existence of the scaling relation and motivates its use in defining the final `redMaPPer` counterparts for the PSZ2.

We define the best `redMaPPer` counterparts with the following cuts:

1. $(\theta/\theta_{\rm err}) \leq 1$ or $(\theta/\theta_{500}) \leq 1$;
2. $|\Delta_{\ln}\lambda| \leq 3$;
3. when more than one object remains a possible counterpart, we choose the highest ranked match.

These criteria on angular separation, θ, allow objects with centres either within *Planck*'s positional uncertainty or within the estimated size of the cluster (or both). The second criterion imposes the richness requirement based on the scaling relation. If there remains more than one possible counterpart satisfying these two criteria, then we choose the one with the largest richness. These latter cases, however, deserve closer examination, in particular for potential projection effects.

Figure 25 shows the distribution of `redMaPPer` objects for *Planck* sources with single and double matches. The dashed lines delineate the angular cuts, while open circles identify those objects that also satisfy the richness cut. We see that the richness cut effectively eliminates objects that would be accepted on angular criteria alone. For the double matches, there are no good second-ranked `redMaPPer` counterparts, because only the highest richness object satisfies the richness cut. Table 5 summarizes the distribution of the 375 counterparts found with the above cuts.

7.3.2. Other optical information

We perform targeted searches for counterparts within the SDSS footprint for all *Planck* sources without good `redMaPPer`

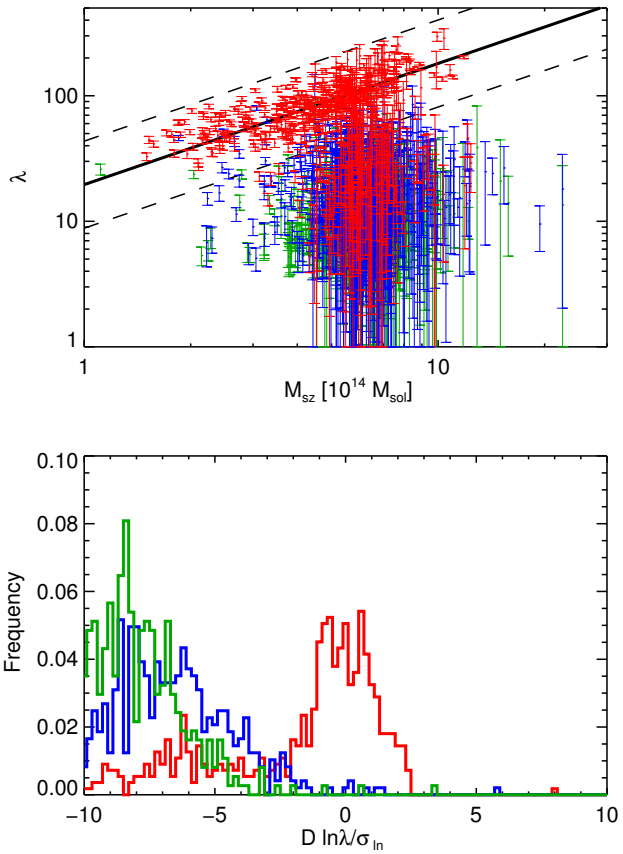

Fig. 24. Distribution of positional matches within a 10 arcmin radius in the richness-M_{SZ} plane. The red points in the *upper panel* represent the highest richness match, blue the second (when present) and green points the third-ranked richness match (when present). The mean scaling law from Rozo et al. (2015) is shown as the solid line, with the dashed lines delineating the $\pm 3\sigma$ band. In the *lower panel*, we show the distribution of these points relative to the mean relation, normalized to the logarithmic scatter. The red, blue and green histograms refer to the first-, second-, and third-ranked matches, respectively.

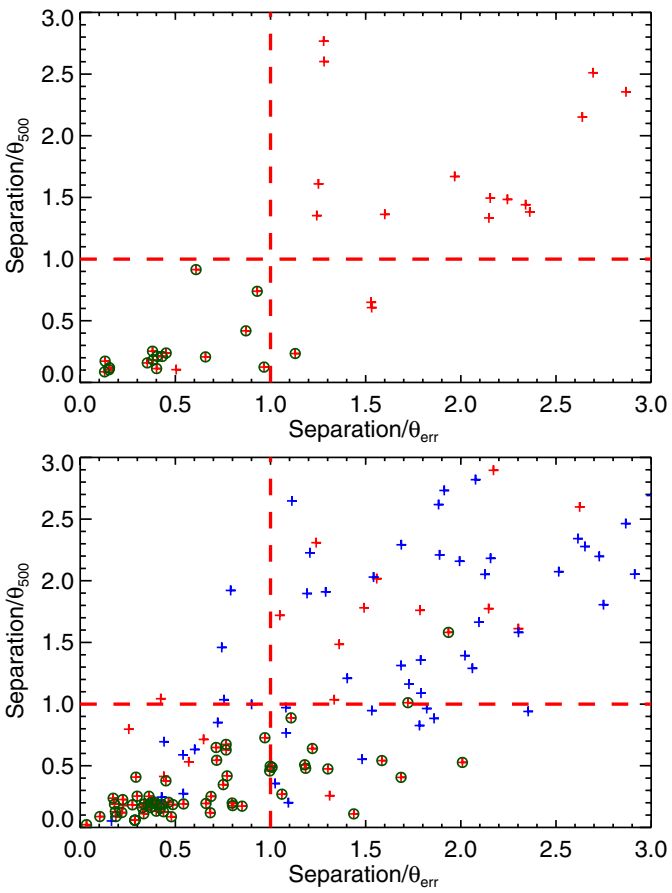

Fig. 25. Selection criteria for `redMaPPer` counterparts. Objects are plotted following the same colour scheme as in the previous figure, i.e., first-, second- and third-ranked matches represented by red, blue and green symbols, respectively. The bands delineate the acceptable region defined by the angular criterion, and circled points indicate objects that also satisfy the richness cut (Criterion 1). *Upper panel*: single matches within a 10 arcmin radius. *Lower panel*: double matches within a 10 arcmin radius. Note that in both panels, only first-ranked matches appear as good counterparts by satisfying both criteria.

matches by applying the `redMaPPer` algorithm on a case-by-case basis. This yields an additional 17 counterparts and associated redshifts.

We add optical confirmations and redshifts from several other sources. These include optical counterparts for PSZ1 clusters published recently from PanSTARRs data (Liu et al. 2015) and from Planck Collaboration optical follow-up observations (Planck Collaboration Int. XXVI 2015; Planck Collaboration Int. XXXVI 2016). We also search for counterparts in the NED[7] database, again removing any negated duplicate matches from the systematic searches. We compared the NED redshifts for PSZ2 matches to the redshifts from all the other ancillary catalogues we have studied. The NED redshifts have 88% agreement with these sources within $\Delta z < 0.02$. We therefore caution that NED redshifts should be considered the least reliable of our counterpart assignments. The NED counterparts are dominated by optical associations with Abell (Abell 1958) and Northern Optical Cluster Survey clusters (Gal et al. 2003).

Finally, we add four high-z counterparts confirmed using SDSS data and which are discussed in Appendix A.

[7] The NASA/IPAC Extragalactic Database (NED) is operated by the Jet Propulsion Laboratory, California Institute of Technology, under contract with the National Aeronautics and Space Administration.

7.4. IR information

At *Planck* detection positions, we have searched for galaxy over-densities in the AllWISE mid-infrared source catalogue (Cutri et al. 2013). The AllWISE source catalogue includes the combined cryogenic and NEOWISE (Mainzer et al. 2011) observations from the Wide-field Infrared Survey Explorer mission (WISE; Wright et al. 2010). The data cover the entire sky and we used the deepest bandpasses, the 3.4 μm (W1) and 4.6 μm (W2) channels. We predicted galaxy (W1–W2) colours from Bruzual & Charlot (2003) stellar population models, and searched for galaxy over-densities of the same colour in successive redshift ranges from $z = 0.3$ to $z = 1.5$ (e.g. Papovich et al. 2010; Mei et al. 2012, 2015; Stanford et al. 2014). At redshift $z < 0.3$, the contrast between red mid-infrared galaxies and the background is not efficient for galaxy cluster detection, so we searched only in the fields of *Planck* detections already validated at redshift $z > 0.3$, and detections not yet confirmed or with unknown redshift.

We estimated a significance of the over-densities by comparing the number of galaxies found in a region of co-moving diameter of 1 Mpc, with the background galaxies found in regions of the same area. To estimate the background density, we

Table 5. Summary of the distribution of the 375 counterparts found with `redMaPPer`.

	Matches					
	Single	Double		Triple		
RANK	(/40)	(/85)		(/438)		
1	17	58	0	283	8	0
2			0		6	0
3						2

Notes. The results are grouped into sets of columns for single-, double-, and triple-matched *Planck* objects. For each grouping, the total number of *Planck* sources is given in parentheses in the heading. The table entries list the number of matches in matrix format, such that the element (i, j) of the matrix gives the number of *Planck* sources with both i- and j-ranked `redMaPPer` counterparts. For example, six of the 438 triple matches have a good second-ranked counterpart only, while eight have both good first- and second-ranked counterparts.

calculated for each redshift range both a local background for each candidate, in a region within 15 arcmin from the *Planck* detection, and a master background derived from the estimators for all the *Planck* fields. A substantial percentage of the *Planck* detections (about 37%) were affected by artefacts from bright stars in the WISE data, which compromise meaningful assessment of the galaxy over-densities. The bulk of these were at low Galactic latitude ($|b| < 20$). This means that we do not expect to reach a detection completeness of better than 60–70%.

After visual inspection of all detections, we flagged our detections in regions not affected by bright star artefacts with the following classification: 3, significant galaxy overdensity detected; 2, probable galaxy overdensity; 1, possible galaxy overdensity; and 0, no significant galaxy overdensity. We also included these classifications for detections in regions affected by bright star artefacts: −1, possible galaxy overdensity; −2, no significant galaxy overdensity; and −3, no assessment possible.

To test our classification, and evaluate our completeness and purity, we blindly applied our automated and visual inspection to 100 objects, consisting of 50 confirmed $z > 0.5$ clusters and 50 random positions in the sky. We show the results of this validation test in Table 6. 59% of the fields have images with bright star artefacts, including 17% that are class −3. In class 3 and 2, we obtain a 96% and 80% purity, respectively, for the validated clusters. Given the high purity of the class 3 detections, we classified these objects as confirmed infra-red clusters.

In Table 7, we show the number of WISE *Planck* detections in each class for the 935 *Planck* detections with $z > 0.3$ or unknown redshift. A detailed study of the WISE detections will be published in a separate paper (Mei et al., in prep.). 73 new clusters have been confirmed (class 3 and not validated by other methods) by our WISE image analysis. A further 54 probable new clusters are identified (class 2 and unvalidated by other methods).

7.5. SZ information

We searched for counterparts of our *Planck* detections using catalogues obtained with other SZ surveys, such as the South Pole Telescope (SPT) and the Atacama Cosmology Telescope (ACT), and updated the list of SZ confirmations by direct follow-up with the Arc-minute Micro-kelvin Interferometer (AMI).

Table 6. Total, validated, and spurious detections in a blind test of our WISE detection classification using 50 real and 50 spurious fields.

	Test detections		
CLASS	Total	Validated	Spurious
3	24	23	1
2	10	8	2
1	3	0	3
0	4	0	4
−1	14	2	12
−2	28	8	20
−3	17	9	8

7.5.1. SPT

For SPT, we refer to the recently released catalogue (Bleem et al. 2015), extracted from the full 2500 deg^2 SZ survey. It contains 677 SZ detections, of which 516 have been confirmed as clusters, through optical and near-IR observations. The catalogue contains the photometric redshifts (spectroscopic when available) and mass estimate of the confirmed clusters. More specifically, we chose to use the "Fiducial Cosmology" Catalogue provided by the SPT collaboration, to be consistent with the cosmological parameters used in the present paper. We performed a two step matching process as described in Sect. 7.2, i.e., a positional match within 10 arcmin, leading to 89 single and five double matches, which we verified by comparing our mass estimate with the one provided in the SPT catalogue. The mass estimates are usually consistent at better than 3σ, except for one detection, PSZ2 G249.87-21.65, where they differ by 3.5σ (combined uncertainty on both measurements) . We note, however, that the error bars on the *Planck* mass reflect only the statistical error on the probability contours and do not consider the uncertainties nor the intrinsic scatter in the scaling relation used to break the degeneracy. Moreover, as discussed also in the SPT case by Bleem et al. (2015), the use of a fixed scaling relation and of a fiducial cosmology results in an underestimation of the statistical and systematic uncertainties in both data sets. Therefore, we decided to keep the SPT counterparts for PSZ2 G249.87-21.65, which is also associated in the SPT catalogue with the same MCXC cluster (RXC J0628.8-4143) as in our matching. We checked the position of the matches in the separation plane: none of the single matches have been discarded in this way, while in four out of five multiple matches, one of the counterparts was excluded following this criterion. In the remaining match, two possible counterparts are allowed and we selected as the most likely the one with a smaller mass difference and a smaller separation in terms of θ_{500}.

We observe a systematic difference between the masses we derived from *Planck* data and those provided in the SPT catalogue. While the discrepancies on the mass estimates for each detection are comparable to their statistical uncertainties (between 1 and 2σ), SPT masses are on average 20% larger than the *Planck* ones. The mass is a derived quantity that requires scaling information to be assumed before it can be calculated from the SZ signal measured by either instrument. Comparison of the SZ observables is complicated by the different scales probed by each instrument: *Planck* is sensitive to the cluster outskirts, while SPT is sensitive to the core regions. Any comparison necessarily requires model extrapolation, which is complicated further by the different pressure models used in the two measurements. A

Table 7. WISE *Planck* detection classification.

	WISE *Planck* detections[a]			
Class	Total	% of sample	Previously confirmed	Unconfirmed
3	374	40	301	73
2	68	7	14	54
1	55	6	7	48
0	88	9	15	73
−1	42	4	5	37
−2	97	10	15	82
−3	211	23	55	156

Notes. [(a)] For each WISE detection class, we show the total number of *Planck* detections and their percentage with respect to the 935 objects with known redshift $z > 0.3$ or unknown redshift, the number of previously confirmed *Planck* clusters, and the number of unconfirmed *Planck* detections.

robust comparison will require a joint analysis of the data, which is beyond the scope of this paper.

7.5.2. ACT

For ACT, we use the catalogue published in Hasselfield et al. (2013), which contains both the most recent ACT detections and an update of the 23 Marriage et al. (2011) detections. 32 PSZ2 sources match with ACT clusters in a 10 arcmin radius. 28 have ACT UPP-based SZ masses consistent with *Planck* M_{SZ} (less than 3σ deviation). Four have more than 3σ deviation: PSZ2 G053.44-36.25 (ACT-CLJ2135.1–0102) and PSZ2 G130.21-62.60 (ACT-CLJ0104.8+0002) are actually considered as good matches by our `redMaPPer` association; PSZ2 G262.27-35.38 (ACT-CLJ0516–5430) is also a good match for our MCXC association; and the last one, PSZ2 G265.86-19.93 (ACT-CLJ0707−5522), is a good match in the PSZ1. We decided to leave blank the ACT field of the PSZ2 catalogue for these four clusters, but, given the uncertainties on the mass determination and associated errors, we did not break the corresponding `redMaPPer`, MCXC, and PSZ1 association.

7.5.3. AMI

Following the ongoing observations of the *Planck* cluster candidates, a total of 161 clusters with $4.5 < S/N < 20$ were observed with AMI. The detection significance is then characterized by calculating of the natural logarithm of the Bayes factor, $\ln B_{10}$,

$$\ln B_{10} = \Delta \ln \mathcal{Z}_{10} = \ln \mathcal{Z}_1 - \ln \mathcal{Z}_0, \quad (10)$$

where $\ln \mathcal{Z}_1$ and $\ln \mathcal{Z}_0$ are the natural logarithm of the Bayesian evidence for model H_1 and H_0 respectively. Model H_1 accounts both for the cluster signal and the contribution from radio sources, while H_0 only takes into account the radio source environment. Further details of the AMI observations, of the Bayesian methodology and of the modelling of interferometric SZ data, primordial CMB anisotropies, and resolved and unresolved radio point sources, as well as of the criteria used to categorize clusters, are given in Perrott et al. (2015) and references therein.

In this context the detection significance for the 161 clusters is described in Table 8. 132 of the 161 AMI confirmed *Planck* clusters are included in the PSZ2.

Table 8. Scale used for an interpretation of the detection significance of the AMI–*Planck* cluster candidates.

Category	$\ln B_{10}$	N
Clear detection	$\ln B_{10} \geq 3$	102
Moderate detection	$0 \leq \ln B_{10} < 3$	30
Non-detection	$-3 \leq \ln B_{10} < 0$	25
Clear non-detection	$\ln B_{10} \leq -3$	4

7.6. Redshift compilation

We provide a single redshift estimate for each detection where at least one redshift is known for a matched counterpart. In many cases, we have multiple estimates per detection. This section discusses the compilation of redshift information and how redshifts are assigned in the final catalogue. Confirmation statistics and final assigned redshift numbers are summarized in Table 9.

Initial redshift estimates are taken from the PSZ1 catalogue redshift compilation, given the matching in Sect. 7.1. We include new follow-up results from the Planck Collaboration (Planck Collaboration Int. XXVI 2015; Planck Collaboration Int. XXXVI 2016), which include spectroscopic updates to PSZ1 photometric redshifts and new confirmations of PSZ1 detections. We also include external updates to PSZ1 counterpart redshifts from the NED and SIMBAD databases (Planck Collaboration XXXII 2015).

After these steps, we cycle through priority levels in our systematic counterpart searches, in the following order of priority: MCXC, `redMaPPer`, ACT, and SPT. We compare the updated PSZ1 and MCXC redshifts with the redshifts from `redMaPPer` where available, and prioritise `redMaPPer` redshifts highest amongst available photometric redshifts. We test spectroscopic redshifts at $z > 0.1$ for consistency within $\Delta z < 0.03$ and $\Delta z/z < 0.1$ of the `redMaPPer` photo-z. Any discrepancies are considered on an individual basis. In a small number of cases, we choose the `redMaPPer` redshift. We also reject a small number of counterpart assignments where that counterpart is a bad match in `redMaPPer`. These cases are discussed in Appendix B.

The common sample between the PSZ2 and each of the external samples is denoted in the catalogue. After the systematic searches, we assign any remaining unconfirmed clusters to database counterparts where available. If a PSZ1 match assigns to the same counterpart as one of the rejected counterparts from

Table 9. Summary of ancillary information.

Confirmation source	Validation	Priority	Joint sample size	Reference confirmations	Planck-discovered	Redshift reference
ENO follow-up	10	1/5	...	22	18	Planck Collaboration Int. XXXVI (2016)
RTT follow-up	11	1/5	...	45	31	Planck Collaboration Int. XXVI (2015)
PanSTARRs	12	6	...	16	16	Liu et al. (2015)
`redMaPPer` non-blind	13	...	...	17	5	This paper: Sect. 7.3.2
SDSS high-z	14	...	...	4	4	This paper: Appendix A
AMI follow-up	15	...	...	10	10	...
WISE	16	...	...	73	73	...
PSZ1 2013	20	1	782	348	125	Planck Collaboration XXIX (2014)
MCXC	21	2	551	447	0	Piffaretti et al. (2011)
SPT	22	4/5	94	39	4	Bleem et al. (2015)
ACT	23	4/5	28	1	0	Hasselfield et al. (2013)
`redMaPPer`	24	3	374	122	2	Rykoff et al. (2014)
Updated PSZ1	25	1	...	19	0	Planck Collaboration XXXII (2015)
NED	30	7	...	40	1	Various

Notes. The highest available priority redshift source, following the ordering in the Priority column, provides the reference confirmation and redshift. When two priorities are given, the first number pertains to spectroscopic redshifts and the second number to photometric redshifts. The PSZ2 contains 1203 confirmed clusters, of which 289 are *Planck*-discovered. 87 of these are clusters newly identified in this paper: 73 are confirmed by WISE; eight are new identifications in SDSS data; and six are confirmed by AMI.

the systematic searches (where the possible counterpart violated the consistency criteria), then the PSZ1 match is also rejected.

8. Sample properties

8.1. Mass and redshift properties

We discuss here the distribution of *Planck* SZ-selected clusters in the mass-redshift ($M_{500} - z$) plane, using the mass proxy derived using scaling relations discussed in Sect. 7. For 1094 detections with known redshifts in the PSZ2 catalogue (Sect. 7), we show in Fig. 26 their position in the M_{500}-z plane, compared with the expected completeness function $\chi(M_{500}, z)$ of our survey (we show the 20%, 50% and 80% completeness levels). These curves indicate the points in the $M_{500} - z$ plane at which clusters have different probabilities of being detected. They were computed for the full survey area. The red points in Fig. 26 show the 298 new PSZ2 confirmed detections, with redshifts, which were not found in the previous version of the catalogue. The black points show the common PSZ1–PSZ2 detections.

We stress that the M_{500}-z distribution in Fig. 26 cannot be considered as fully representative of the *Planck* SZ selection, since it reflects the biases due to the non-uniform knowledge of redshifts over the sky in the ancillary information we used (Sect. 7). For instance, we have extensive redshift information in the sky area covered by the SDSS survey thanks to the `redMaPPer` catalogue (Rykoff et al. 2014), but not in the remaining part of the sky. This incomplete redshift information can also explain the rarity of new detections in the PSZ2 catalogue with respect to PSZ1 at high redshift: at $z > 0.6$ we have 36 objects, but only four new PSZ2 detections. We note however that most of the PSZ1 clusters in this redshift range were not present in existing catalogues, but were confirmed as clusters and their redshift measured thanks to the massive follow-up campaign with optical and X-ray telescopes that was undertaken by the Planck Collaboration for PSZ1 candidates (Planck Collaboration XXIX 2014 and references therein) and which continued also after the 2013 release (Planck Collaboration Int. XXVI 2015; Planck Collaboration Int. XXXV 2016). Since a similar observational campaign has not yet been possible for new PSZ2 detections, we could not populate further the high-mass high-z part of the M_{500}-z plane.

The new PSZ2-confirmed detections (red points in Fig. 26) are mostly low-mass objects close to the detection limit of the survey. The mean mass of confirmed clusters over the whole redshift range in the PSZ2 is $4.82 \times 10^{14}\ M_{\odot}$, which is lower than in the PSZ1 ($5.12 \times 10^{14}\ M_{\odot}$). The common sample of 795 objects contains the higher mass clusters detected by both surveys, with mean mass $5.16 \times 10^{14}\ M_{\odot}$. This is expected, since the common sample contains none of the new low-mass PSZ2 detections and none of the missing low S/N PSZ1 detections (discussed in Sect. 6.3), which were likely to have been low mass.

This is also shown in Fig. 27, where we compare the mass distribution of the confirmed clusters in the PSZ2, the PSZ1 and their common sample, for several redshift bins. The median mass and the first and third quartiles are always lower for the PSZ2 than for the PSZ1 and the common sample, showing that we are significantly expanding the sample towards lower masses.

Figure 26 also shows a comparison of the SZ-selected samples from the *Planck*, ACT, and SPT surveys. *Planck* tends to detect the rarest high-mass clusters observed at high-redshift in these partial-sky surveys and provides a complementary clean SZ selection at lower redshifts, where the *Planck* frequency range provides sufficient information to disentangle the SZ signal of large clusters from the background.

8.2. X-ray underluminous clusters

The presence of a bright cool-core, characterized by a peaked surface brightness profile, has been shown to bias X-ray flux-selected cluster samples in favour of peaked, relaxed objects with respect to morphologically disturbed systems (Eckert et al. 2011). In contrast, SZ-selected samples have produced more disturbed systems than expected, with SZ-discovered clusters typically lying on the lower end of the mass-luminosity relation (Planck Collaboration IX 2011). There has also been much interest in the possible existence of severely X-ray under-luminous clusters, with several authors identifying potential systems (e.g., Bower et al. 1997; Popesso et al. 2007; Dietrich et al. 2009; Trejo-Alonso et al. 2014 and references therein) and suggesting

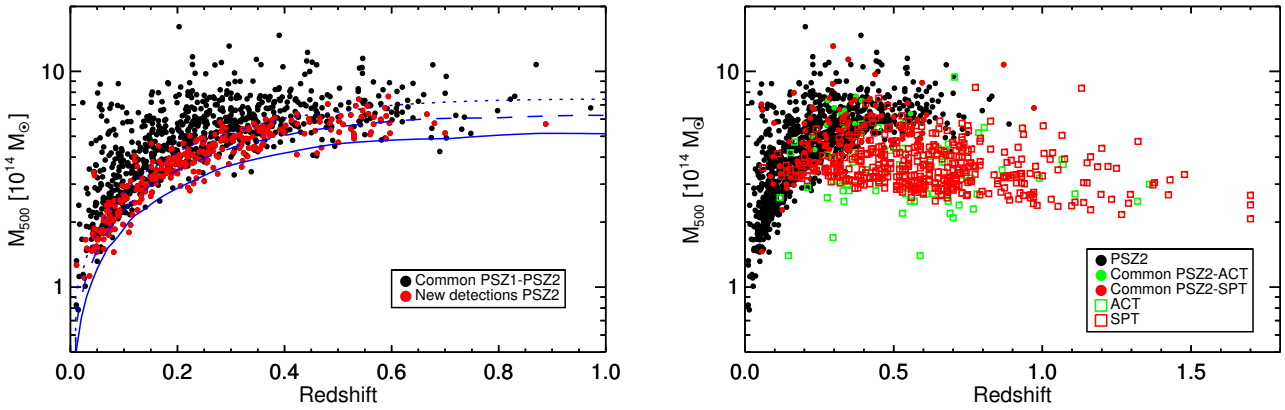

Fig. 26. *Left:* distribution in the M_{500}-z plane of the 1094 PSZ2 clusters with counterparts with known redshift. New PSZ2-detected clusters are indicated with red dots, while commmon PSZ1 and PSZ2 clusters are indicated by black dots. The solid, dashed, and dotted lines indicate, respectively, the 20%, 50%, and 80% survey completeness contours for the PSZ2. *Right:* distribution of the PSZ2 clusters with associated redshift in the $M_{500} - z$ plane compared to the SPT (Bleem et al. 2015) and ACT (Hasselfield et al. 2013) catalogues. Black circles represent PSZ2 clusters, while red and green filled circles mark common SPT/PSZ2 and ACT/PSZ2 clusters, respectively. The remaining SPT and ACT clusters not detected by *Planck* are shown with red and green empty squares.

a model where these clusters are dynamically young objects, still undergoing accretion and mergers and yet to reach equilibrium. An alternative suggestion is that line-of-sight structures may bias mass and richness estimates high relative to the X-ray luminosity (Bower et al. 1997; Giles et al. 2015). However, the reported under-luminosity of these objects is disputed. Andreon & Moretti (2011) note that the under-luminosity is often claimed relative to biased scaling relations, and that the significance of the under-luminosity is amplified due to underestimation of the true scatter in the relation.

In the SDSS area, the majority of *Planck* detections possess counterparts in the `redMaPPer` catalogue, with redshifts and optical richness estimates. We construct a test sample from the *Planck*-`redMaPPer` intersection at low redshift, $z < 0.2$. This sample of 148 clusters can be expected to be detectable in ROSAT maps. While `redMaPPer` is not complete for the *Planck* mass ranges at these redshifts, it allows us to construct a sample that is independent of any X-ray selection effects and therefore well-suited for finding under-luminous clusters, since any biases in selection will affect both normal and under-luminous X-ray clusters alike.

For each of these clusters, we calculated the X-ray count-rate using a growth-curve analysis on the ROSAT 0.5−2.4 keV band maps following Böhringer et al. (2000). We derived the count-rate and its upper and lower limit from the growth curve at θ_{500}, which we calculated from the *Planck* mass proxy. We then converted the RASS count rates into flux in the 0.1−2.4 keV energy range, using an absorbed thermal model, where we used the Galactic absorption at the *Planck* position, the redshift of the `redMaPPer` counterpart and the temperature derived from the mass proxy through the *M*-*T* scaling relation of Arnaud et al. (2007). We then converted fluxes into luminosity in the 0.1−2.4 keV channel. We found good agreement with the reported MCXC values of L_{500} for those clusters also present in the MCXC.

We then searched for outlier clusters from the Y_{500}–L_{500} and Y_{500}–λ relations, using the Y_{500} value calculated following Sect. 5.3. In both cases, we find the best-fit relation for our sample using the BCES algorithm. To exclude outliers from the fits, we clipped objects with orthogonal residual $|r_\perp| > 2.5\sigma_{\rm tot}$ from the best-fit relations, where $\sigma_{\rm tot}$ is the raw scatter around the relation derived from the median-absolute deviation. We

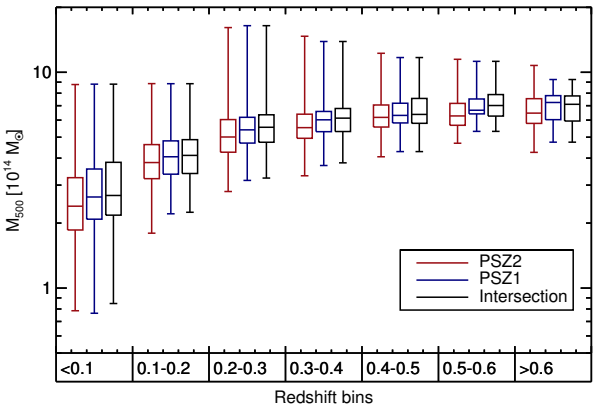

Fig. 27. Box-and-whisker diagrams showing the mass distribution of the PSZ2 (red), PSZ1 (blue) and their intersection (black) sample in seven redshift bins. The bottom and the top of the boxes represent the first and third quartile of the data, while the band inside the box shows the median (i.e., the second quartile). The ends of the whiskers mark the minimum and maximum of the data.

then iterated the sigma-clipping process until convergence was reached.

The top panels of Fig. 28 show the best-fit relations and their $\pm 2\sigma_{\rm tot}$ scatters between Y_{500} and `redMaPPer` richness λ, and between Y_{500} and L_{500}, for the test sample of 148 *Planck*-`redMaPPer` clusters. The bottom panels of Fig. 28 show the histograms of Δ, normalized by $\sigma_{\rm tot}$.

The points highlighted with larger cyan circles denote clusters with L_{500} more than 2.5 $\sigma_{\rm tot}$ below the best-fit relation. These clusters are under-luminous in X-rays for their Y_{500}. However, their Y_{500} estimates are consistent with their optical richness and do not lie preferentially beneath the relation. The consistency of optical and SZ mass proxies suggest either that these clusters are under-luminous for their mass, or that both the Y_{500} and λ estimates are biased high.

One exception to this is PSZ2 G127.71–69.55, which is discrepant with both relations: at $10\sigma_{\rm tot}$ for Y_{500}–L_{500}; and $3\sigma_{\rm tot}$ for Y_{500}–λ. It is circled in red in Figure 28. This is the only cluster in the *Planck*-`redMaPPer` sample with a poor Q_NEURAL flag

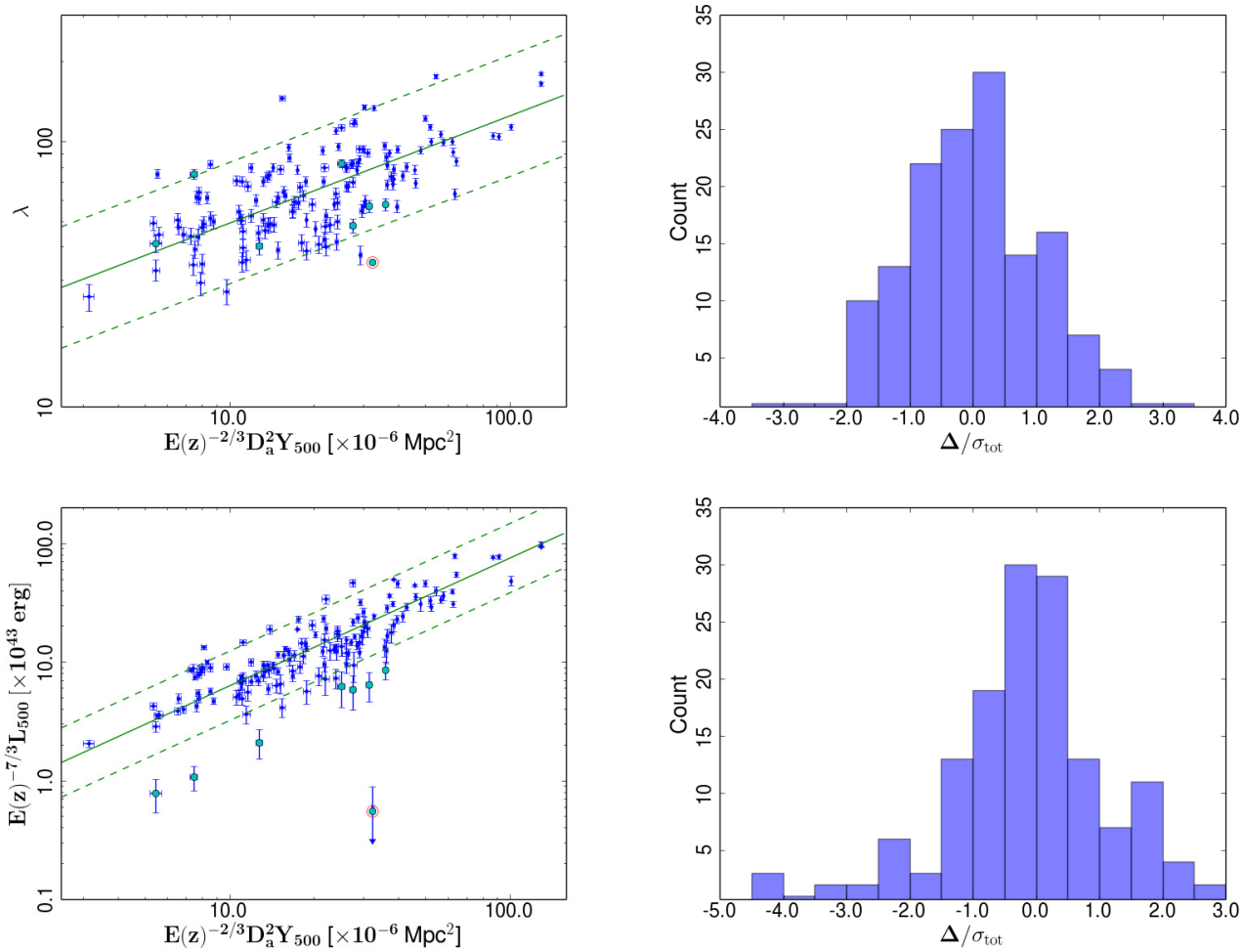

Fig. 28. Properties in the Y_{500}–λ (*top panels*) and Y_{500}-L_{500} (*bottom panels*) planes for the *Planck*-`redMaPPer` sample at $z < 0.2$. Under-luminous candidates are denoted with cyan circles in the scatter *plots to the left*, which also show the best fit relation and the dispersion $\pm 2\sigma_{tot}$. The circled red point is a cluster with contaminated Y signal. The *right plots* show the histograms of orthogonal deviation $\Delta_\perp$ for each relation.

and is either a failed `redMaPPer` match (lying close to the matching threshold in the $M_{sz} - \lambda$ plane) or a cluster with a severely IR-contaminated spectrum for which the *Planck* Y_{500} estimate is likely overestimated. We therefore remove this from the list of under-luminous candidates.

We also expanded the search for under-luminous clusters across the whole sky, testing all clusters with $z < 0.2$ against the mean Y_{500}–L_{500} relation determined above. This increased the number of under-luminous candidates to 22. These objects warrant follow-up observations to determine their dynamical state and to search for line-of-sight structures that may bias high both the Y_{500} and optical richness; they are flagged in the COMMENT field of the catalogue and should be of interest in understanding the systematic differences between SZ and X-ray selection.

9. Summary

The *Planck* satellite is unique in providing broad frequency coverage over the whole sky with good sensitivity to both the high frequency spectral increment and the low frequency decrement of the thermal SZ effect. In this paper, we have presented second *Planck* catalogue of SZ sources (PSZ2). This is based on data from the full 29 month mission and uses a methodology that refines the one used to produce the PSZ1 from 15.5 months of data. The catalogue is based on the union of results from three cluster detection codes (Planck Collaboration XXIX 2014). The PSZ2 contains 1653 cluster candidates distributed across 83.6% of the sky. The catalogue was validated using external X-ray, optical, SZ and near infra-red data, producing confirmation for 1203 candidates with 1094 redshifts. The catalogue contains 716 new detections including 366 confirmed clusters with newly identified SZ signal. 87 of our confirmed clusters are newly identified in this paper. We have found good consistency with the PSZ1 and re-detect 937 SZ sources from the PSZ1 sample of 1227. We have investigated the missed detections: the vast majority of these were low-significance PSZ1 detections whose S/N has fluctuated beneath the detection threshold. The majority of these are expected to be spurious detections.

The current status of our knowledge of counterparts for our detections at various frequencies is summarised in Table 10 and compared to the PSZ1. Our optical validation scheme is based on the newly released SDSS-based `redMaPPer` catalogue (Rozo & Rykoff 2014). This produced 374 high-quality matches where the counterparts are consistent with *Planck* mass and position information. We reject 188 possible matches where the mass or position information is inconsistent with the *Planck* information. This underlines the importance of consistency checks when matching with high density SDSS catalogues. Our X-ray and SZ counterpart searches implement similar consistency criteria leading to tight control over mismatches.

Table 10. Counterpart summary for PSZ2 compared to PSZ1.

Sample	PSZ1 2013	PSZ1 2015	PSZ2	Common	New PSZ2
Union	1227	1227	1653	937	716
Intersection	546	546	827	502	325
Confirmed	861	947	1203	820	383
Candidates	366	292	546	99	447
Low reliability	142	131	143	39	104
Total X-ray	501	501	603	477	126
MCXC	455	455	551	427	124
SZ clusters	82	82	110	79	31

Notes. Common samples are defined as those PSZ2 detections with the given property that has a counterpart with that property in the PSZ1 2015. The intersection comprises those detections common to all three detector codes. Low reliability candidates possess a poor neural-network quality assessment flag. In the PSZ1, low reliability candidates possess the lowest external quality assessment flag. "SZ clusters" here means clusters with SZ detections in ACT or SPT. "PSZ1 2013" refers to the 2013 release of the catalogue (Planck Collaboration XXIX 2014), and "PSZ1 2015" to a recent addendum updating the counterpart information of the catalogue (Planck Collaboration XXXII 2015).

Central to the counterpart search process is the understanding of the *Planck* SZ parameter estimates. We have validated the *Planck* Compton-Y posteriors using detailed simulations that include an ensemble of hydro-dynamically simulated pressure profiles that vary from the pressure profile assumed by our extraction algorithms. Our Y_{5R500} estimates are robust to mis-matches in the pressure profile. When translating to Y_{500}, we have shown the importance of accurate prior information about radius to break the $Y - \theta$ degeneracy and produce accurate and precise estimates from the *Planck* data. Our counterpart searches make extensive use of the *Planck* mass-proxy; this uses prior information about redshift and scaling relations to derive mass constraints which show low scatter with respect to external estimates. We provide this $M_{\rm sz}$ for all candidates with a redshift, and provide $M_{\rm sz}(z)$ in the range $0 < z < 1$ for all other candidates. We expect this information to be useful in future comparisons with external data.

Central to any statistical use of a cluster sample is the survey selection function. We have estimated the catalogue completeness using Monte-Carlo source injection and we provide this as a product for the full survey and for various sub-samples as a function of selection S/N. We have validated the completeness through a comparison with external X-ray data and high resolution SZ data from SPT (Bleem et al. 2015), which spans the redshift range and angular sizes of the *Planck* data. We estimate the catalogue to be 83−87% pure, based on simulations of the *Planck* data and detection-by-detection quality assessment utilising machine learning. Higher reliability sub-samples can be constructed easily: the main contaminant is infra-red galactic emission and as such the reliability is a strong function of galactic latitude. Specifically, the cluster cosmology zone that covers 65% of the sky contains 1308 detections at ∼90% reliability, and full survey intersection catalogue (objects detected by all three codes) contains 827 detections at >95% reliability.

Cosmology using the cluster counts is also dependent on external observational data to provide cluster redshifts. Planck Collaboration XXIV (2016) have produced cosmological constraints using samples drawn from the PSZ2, containing 493 candidates from the intersection sample and 439 drawn from the single-code `MMF3` sample. Utilising larger samples from the PSZ2 requires further redshift information. We also expect the PSZ2 to contain many high-mass clusters at $z > 0.6$. So far only 36 have been identified, of which 21 were identified in targeted follow-up observations of PSZ1 candidates. For these reasons, the PSZ2 should motivate further follow-up observations. In particular, the catalogue contains 73 clusters confirmed by WISE infra-red data that currently have no redshift information but which are likely to be high-redshift.

Understanding the biases in cluster selection that affect samples defined at different wavelengths will be important for interpreting statistical results from existing surveys and those planned for the near future. Using a low-redshift overlap sample from PSZ2 and `redMaPPer`, we have identified a population of low-z clusters with "typical" optical and SZ properties, but which are underluminous for their mass in ROSAT X-ray data. These clusters may be part of a population of dynamically disturbed clusters that are under-represented in X-ray selected surveys. These objects will be interesting targets for multi-wavelength follow-up to determine their dynamical state.

In the near future, *Planck* all-sky SZ data can be combined with observations of the large-scale structure by surveys such as PAN-STARRS, LOFAR, Euclid, LSST, and RSG/e-ROSITA. This will provide an unprecedented multi-wavelength view of the evolution of large-scale structure that will revolutionise our understanding of the physics governing this process.

Acknowledgements. The Planck Collaboration acknowledges the support of: ESA; CNES and CNRS/INSU-IN2P3-INP (France); ASI, CNR, and INAF (Italy); NASA and DoE (USA); STFC and UKSA (UK); CSIC, MINECO, JA, and RES (Spain); Tekes, AoF, and CSC (Finland); DLR and MPG (Germany); CSA (Canada); DTU Space (Denmark); SER/SSO (Switzerland); RCN (Norway); SFI (Ireland); FCT/MCTES (Portugal); ERC and PRACE (EU). A description of the Planck Collaboration and a list of its members, indicating which technical or scientific activities they have been involved in, can be found at `http://www.cosmos.esa.int/web/planck/planck-collaboration`. We thank Ian McCarthy for providing images and profiles of simulated clusters from cosmo-OWLS. This research has made use of the NASA/IPAC Extragalactic Database (NED), which is operated by the Jet Propulsion Laboratory, California Institute of Technology, under contract with the National Aeronautics and Space Administration, and the SIMBAD database, operated at CDS, Strasbourg, France This research made use of data retrieved from SDSS-III. Funding for SDSS-III has been provided by the Alfred P. Sloan Foundation, the Participating Institutions, the National Science Foundation, and the US Department of Energy Office of Science; the SDSS-III web site is `http://www.sdss3.org/`. This research has made use of data processed by the Centre d'Analyse de Données Étendues (`http://cade.irap.omp.eu/`) and has made use of the `HEALPix` pixelization software (`http://healpix.sourceforge.net`; Górski et al. 2005). Some of this work was performed using the Darwin Supercomputer of the University of Cambridge High Performance Computing Service (`http://www.hpc.cam.ac.uk/`), provided by Dell Inc. using Strategic Research Infrastructure Funding from the Higher Education Funding Council for England and funding from the Science and Technology Facilities Council.

References

Abell, G. O. 1958, ApJS, 3, 211
Aghanim, N., Hurier, G., Diego, J.-M., et al. 2015, A&A, 580, A138
Allen, S. W., Evrard, A. E., & Mantz, A. B. 2011, ARA&A, 49, 409
Andreon, S., & Moretti, A. 2011, A&A, 536, A37
Arnaud, M., Pointecouteau, E., & Pratt, G. W. 2007, A&A, 474, L37
Arnaud, M., Pratt, G. W., Piffaretti, R., et al. 2010, A&A, 517, A92
Benson, B. A., de Haan, T., Dudley, J. P., et al. 2013, ApJ, 763, 147
Bleem, L. E., Stalder, B., de Haan, T., et al. 2015, ApJS, 216, 27
Böhringer, H., Voges, W., Huchra, J. P., et al. 2000, ApJS, 129, 435
Böhringer, H., Schuecker, P., Guzzo, L., et al. 2004, A&A, 425, 367
Borgani, S., & Kravtsov, A. 2011, Adv. Sci. Lett., 4, 204
Bösch, B., Böhm, A., Wolf, C., et al. 2013, A&A, 554, A97
Bower, R. G., Castander, F. J., Ellis, R. S., Couch, W. J., & Boehringer, H. 1997, MNRAS, 291, 353
Bruzual, G., & Charlot, S. 2003, MNRAS, 344, 1000
Burenin, R. A., Vikhlinin, A., Hornstrup, A., et al. 2007, ApJS, 172, 561
Carlstrom, J. E., Holder, G. P., & Reese, E. D. 2002, ARA&A, 40, 643
Carvalho, P., Rocha, G., & Hobson, M. P. 2009, MNRAS, 393, 681
Carvalho, P., Rocha, G., Hobson, M. P., & Lasenby, A. 2012, MNRAS, 427, 1384
Chamballu, A., Bartlett, J. G., & Melin, J.-B. 2012, A&A, 544, A40
Chen, Y., Reiprich, T. H., Böhringer, H., Ikebe, Y., & Zhang, Y.-Y. 2007, A&A, 466, 805
Crawford, C. S., Edge, A. C., Fabian, A. C., et al. 1995, MNRAS, 274, 75
Cutri, R. M., Wright, E. L., Conrow, T., et al. 2013, Explanatory Supplement to the AllWISE Data Release Products, Tech. Rep.
da Silva, A. C., Kay, S. T., Liddle, A. R., & Thomas, P. A. 2004, MNRAS, 348, 1401
Dietrich, J. P., Biviano, A., Popesso, P., et al. 2009, A&A, 499, 669
Ebeling, H., Edge, A. C., Bohringer, H., et al. 1998, MNRAS, 301, 881
Ebeling, H., Edge, A. C., Mantz, A., et al. 2010, MNRAS, 407, 83
Eckert, D., Molendi, S., & Paltani, S. 2011, A&A, 526, A79
Gal, R. R., de Carvalho, R. R., Lopes, P. A. A., et al. 2003, AJ, 125, 2064
Giles, P. A., Maughan, B. J., Hamana, T., et al. 2015, MNRAS, 447, 3044
Górski, K. M., Hivon, E., Banday, A. J., et al. 2005, ApJ, 622, 759
Haehnelt, M. G., & Tegmark, M. 1996, MNRAS, 279, 545
Hao, J., McKay, T. A., Koester, B. P., et al. 2010, ApJSS, 191, 254
Harrison, D., Sutton, D., Carvalho, P., & Hobson, M. 2015, MNRAS, 451, 2610
Hasselfield, M., Hilton, M., Marriage, T. A., et al. 2013, J. Cosmol. Astropart. Phys., 7, 8
Herranz, D., Sanz, J. L., Hobson, M. P., et al. 2002, MNRAS, 336, 1057
Hoekstra, H., Mahdavi, A., Babul, A., & Bildfell, C. 2012, MNRAS, 427, 1298
Hogg, D. W., Bovy, J., & Lang, D. 2010, ArXiv e-prints [arXiv:1008.4686]
Kay, S. T., Peel, M. W., Short, C. J., et al. 2012, MNRAS, 422, 1999
Koester, B. P., McKay, T. A., Annis, J., et al. 2007, ApJ, 660, 239
Kravtsov, A. V., Vikhlinin, A., & Nagai, D. 2006, ApJ, 650, 128
Le Brun, A. M. C., McCarthy, I. G., Schaye, J., & Ponman, T. J. 2014, MNRAS, 441, 1270
Liu, J., Hennig, C., Desai, S., et al. 2015, MNRAS, 449, 3370
Mahdavi, A., Hoekstra, H., Babul, A., et al. 2013, ApJ, 767, 116
Mainzer, A., Bauer, J., Grav, T., et al. 2011, ApJ, 731, 53
Marriage, T. A., Acquaviva, V., Ade, P. A. R., et al. 2011, ApJ, 737, 61
Maughan, B. J. 2007, ApJ, 668, 772
McCarthy, I. G., Le Brun, A. M. C., Schaye, J., & Holder, G. P. 2014, MNRAS, 440, 3645
Mehrtens, N., Romer, A. K., Hilton, M., et al. 2012, MNRAS, 423, 1024
Mei, S., Stanford, S. A., Holden, B. P., et al. 2012, ApJ, 754, 141
Mei, S., Scarlata, C., Pentericci, L., et al. 2015, ApJ, 804, 117
Melin, J., Bartlett, J. G., & Delabrouille, J. 2006, A&A, 459, 341
Melin, J.-B., Aghanim, N., Bartelmann, M., et al. 2012, A&A, 548, A51
Mitra, S., Rocha, G., Górski, K. M., et al. 2011, ApJS, 193, 5
Nagai, D., Kravtsov, A. V., & Vikhlinin, A. 2007, ApJ, 668, 1
Papovich, C., Momcheva, I., Willmer, C. N. A., et al. 2010, ApJ, 716, 1503
Peebles, P. J. E. 1980, The large-scale structure of the universe (Princeton University Press)
Perrott, Y. C., Olamaie, M., Rumsey, C., et al. 2015, A&A, 580, A95
Piffaretti, R., Arnaud, M., Pratt, G. W., Pointecouteau, E., & Melin, J.-B. 2011, A&A, 534, A109
Planck Collaboration 2011, The Explanatory Supplement to the Planck Early Release Compact Source Catalogue (ESA)
Planck Collaboration IX. 2011, A&A, 536, A9
Planck Collaboration X. 2011, A&A, 536, A10
Planck Collaboration XX. 2014, A&A, 571, A20
Planck Collaboration XXIX. 2014, A&A, 571, A29
Planck Collaboration XXXII. 2015, A&A, 581, A14
Planck Collaboration I. 2016, A&A, 594, A1
Planck Collaboration II. 2016, A&A, 594, A2
Planck Collaboration III. 2016, A&A, 594, A3
Planck Collaboration IV. 2016, A&A, 594, A4
Planck Collaboration V. 2016, A&A, 594, A5
Planck Collaboration VI. 2016, A&A, 594, A6
Planck Collaboration VII. 2016, A&A, 594, A7
Planck Collaboration VIII. 2016, A&A, 594, A8
Planck Collaboration IX. 2016, A&A, 594, A9
Planck Collaboration X. 2016, A&A, 594, A10
Planck Collaboration XI. 2016, A&A, 594, A11
Planck Collaboration XII. 2016, A&A, 594, A12
Planck Collaboration XIII. 2016, A&A, 594, A13
Planck Collaboration XIV. 2016, A&A, 594, A14
Planck Collaboration XV. 2016, A&A, 594, A15
Planck Collaboration XVI. 2016, A&A, 594, A16
Planck Collaboration XVII. 2016, A&A, 594, A17
Planck Collaboration XVIII. 2016, A&A, 594, A18
Planck Collaboration XIX. 2016, A&A, 594, A19
Planck Collaboration XX. 2016, A&A, 594, A20
Planck Collaboration XXI. 2016, A&A, 594, A21
Planck Collaboration XXII. 2016, A&A, 594, A22
Planck Collaboration XXIII. 2016, A&A, 594, A23
Planck Collaboration XXIV. 2016, A&A, 594, A24
Planck Collaboration XXV. 2016, A&A, 594, A25
Planck Collaboration XXVI. 2016, A&A, 594, A26
Planck Collaboration XXVII. 2016, A&A, 594, A27
Planck Collaboration XXVIII. 2016, A&A, 594, A28
Planck Collaboration Int. III. 2013, A&A, 550, A129
Planck Collaboration Int. IV. 2013, A&A, 550, A130
Planck Collaboration Int. V. 2013, A&A, 550, A131
Planck Collaboration Int. XXVI. 2015, A&A, 582, A29
Planck Collaboration Int. XXXV. 2016, A&A, 586, A138
Planck Collaboration Int. XXXVI. 2016, A&A, 586, A139
Popesso, P., Biviano, A., Böhringer, H., & Romaniello, M. 2007, A&A, 461, 397
Pratt, G. W., Croston, J. H., Arnaud, M., & Böhringer, H. 2009, A&A, 498, 361
Reichardt, C. L., Stalder, B., Bleem, L. E., et al. 2013, ApJ, 763, 127
Reiprich, T. H., & Böhringer, H. 2002, ApJ, 567, 716
Rodriguez-Gonzalvez, C., Chary, R. R., Feroz, F., et al. 2015, MNRAS, submitted [arXiv:1505.01132]
Rozo, E., & Rykoff, E. S. 2014, ApJ, 783, 80
Rozo, E., Wechsler, R. H., Rykoff, E. S., et al. 2010, ApJ, 708, 645
Rozo, E., Rykoff, E. S., Bartlett, J. G., & Melin, J. B. 2015, MNRAS, 450, 592
Rykoff, E. S., Rozo, E., Busha, M. T., et al. 2014, ApJ, 785, 104
Schaye, J., Dalla Vecchia, C., Booth, C. M., et al. 2010, MNRAS, 402, 1536
Schuecker, P., Böhringer, H., Collins, C. A., & Guzzo, L. 2003, A&A, 398, 867
Sifón, C., Menanteau, F., Hasselfield, M., et al. 2013, ApJ, 772, 25
Stanford, S. A., Gonzalez, A. H., Brodwin, M., et al. 2014, ApJS, 213, 25
Staniszewski, Z., Ade, P. A. R., Aird, K. A., et al. 2009, ApJ, 701, 32
Struble, M. F., & Rood, H. J. 1991, ApJS, 77, 363
Struble, M. F., & Rood, H. J. 1999, ApJS, 125, 35
Sunyaev, R. A., & Zeldovich, I. B. 1980, ARA&A, 18, 537
Sunyaev, R. A., & Zeldovich, Y. B. 1970, Comments on Astrophysics and Space Physics, 2, 66
Szabo, T., Pierpaoli, E., Dong, F., Pipino, A., & Gunn, J. 2011, ApJ, 736, 21
Tinker, J., Kravtsov, A. V., Klypin, A., et al. 2008, ApJ, 688, 709
Trejo-Alonso, J. J., Caretta, C. A., Laganá, T. F., et al. 2014, MNRAS, 441, 776
Vikhlinin, A., Burenin, R. A., Ebeling, H., et al. 2009a, ApJ, 692, 1033
Vikhlinin, A., Kravtsov, A. V., Burenin, R. A., et al. 2009b, ApJ, 692, 1060
Wen, Z. L., Han, J. L., & Liu, F. S. 2009, ApJS, 183, 197
Wen, Z. L., Han, J. L., & Liu, F. S. 2012, ApJS, 199, 34
Wright, E. L., Eisenhardt, P. R. M., Mainzer, A. K., et al. 2010, AJ, 140, 1868
York, D. G., Adelman, J., Anderson, Jr., J. E., et al. 2000, AJ, 120, 1579
Zu, Y., Weinberg, D. H., Rozo, E., et al. 2014, MNRAS, 439, 1628

[1] APC, AstroParticule et Cosmologie, Université Paris Diderot, CNRS/IN2P3, CEA/lrfu, Observatoire de Paris, Sorbonne Paris Cité, 10 rue Alice Domon et Léonie Duquet, 75205 Paris Cedex 13, France
[2] Academy of Sciences of Tatarstan, Bauman Str., 20, 420111 Kazan, Republic of Tatarstan, Russia
[3] African Institute for Mathematical Sciences, 6−8 Melrose Road, Muizenberg, Cape Town, South Africa
[4] Agenzia Spaziale Italiana Science Data Center, via del Politecnico snc, 00133 Roma, Italy

[5] Aix Marseille Université, CNRS, LAM (Laboratoire d'Astrophysique de Marseille) UMR 7326, 13388 Marseille, France
[6] Astrophysics Group, Cavendish Laboratory, University of Cambridge, J J Thomson Avenue, Cambridge CB3 0HE, UK
[7] Astrophysics & Cosmology Research Unit, School of Mathematics, Statistics & Computer Science, University of KwaZulu-Natal, Westville Campus, Private Bag X54001, 4000 Durban, South Africa
[8] Atacama Large Millimeter/submillimeter Array, ALMA Santiago Central Offices, Alonso de Cordova 3107, Vitacura, Casilla 763 0355, Santiago, Chile
[9] CITA, University of Toronto, 60 St. George St., Toronto, ON M5S 3H8, Canada
[10] CNRS, IRAP, 9 Av. colonel Roche, BP 44346, 31028 Toulouse Cedex 4, France
[11] CRANN, Trinity College, 2 Dublin, Ireland
[12] California Institute of Technology, Pasadena, California, USA
[13] Centre for Theoretical Cosmology, DAMTP, University of Cambridge, Wilberforce Road, Cambridge CB3 0WA, UK
[14] Centro de Estudios de Física del Cosmos de Aragón (CEFCA), Plaza San Juan 1, planta 2, 44001 Teruel, Spain
[15] Computational Cosmology Center, Lawrence Berkeley National Laboratory, Berkeley, California, USA
[16] Consejo Superior de Investigaciones Científicas (CSIC), 28049 Madrid, Spain
[17] DSM/Irfu/SPP, CEA-Saclay, 91191 Gif-sur-Yvette Cedex, France
[18] DTU Space, National Space Institute, Technical University of Denmark, Elektrovej 327, 2800 Kgs. Lyngby, Denmark
[19] Département de Physique Théorique, Université de Genève, 24 Quai E. Ansermet, 1211 Genève 4, Switzerland
[20] Departamento de Astrofísica, Universidad de La Laguna, 38206 La Laguna, Tenerife, Spain
[21] Departamento de Física, Universidad de Oviedo, Avda. Calvo Sotelo s/n, 33007 Oviedo, Spain
[22] Department of Astronomy and Astrophysics, University of Toronto, 50 Saint George Street, 38100 Toronto, Ontario, Canada
[23] Department of Astronomy and Geodesy, Kazan Federal University, Kremlevskaya Str., 18, 420008 Kazan, Russia
[24] Department of Astrophysics/IMAPP, Radboud University Nijmegen, PO Box 9010, 6500 GL Nijmegen, The Netherlands
[25] Department of Physics & Astronomy, University of British Columbia, 6224 Agricultural Road, Vancouver, British Columbia, Canada
[26] Department of Physics and Astronomy, Dana and David Dornsife College of Letter, Arts and Sciences, University of Southern California, Los Angeles, CA 90089, USA
[27] Department of Physics and Astronomy, University College London, London WC1E 6BT, UK
[28] Department of Physics, Florida State University, Keen Physics Building, 77 Chieftan Way, Tallahassee, Florida, USA
[29] Department of Physics, Gustaf Hällströmin katu 2a, University of Helsinki, 00560 Helsinki, Finland
[30] Department of Physics, Princeton University, Princeton, New Jersey, USA
[31] Department of Physics, University of Arizona, 1118 E 4th St, Tucson, AZ, 85721, NJ 08540, USA
[32] Department of Physics, University of California, One Shields Avenue, Davis, California, USA
[33] Department of Physics, University of California, Santa Barbara, California, CA 95616, USA
[34] Department of Physics, University of Illinois at Urbana-Champaign, 1110 West Green Street, Urbana, Illinois, CA 93106, USA
[35] Dipartimento di Fisica e Astronomia G. Galilei, Università degli Studi di Padova, via Marzolo 8, 35131 Padova, Italy
[36] Dipartimento di Fisica e Scienze della Terra, Università di Ferrara, via Saragat 1, 44122 Ferrara, Italy
[37] Dipartimento di Fisica, Università La Sapienza, P.le A. Moro 2, 00133 Roma, Italy
[38] Dipartimento di Fisica, Università degli Studi di Milano, via Celoria, 16, 20133 Milano, Italy
[39] Dipartimento di Fisica, Università degli Studi di Trieste, via A. Valerio 2, 34127 Trieste, Italy
[40] Dipartimento di Fisica, Università di Roma Tor Vergata, via della Ricerca Scientifica 1, 00133 Roma, Italy
[41] Dipartimento di Matematica, Università di Roma Tor Vergata, via della Ricerca Scientifica 1, 00133 Roma, Italy
[42] Discovery Center, Niels Bohr Institute, Blegdamsvej 17, 1165 Copenhagen, Denmark
[43] Dpto. Astrofísica, Universidad de La Laguna (ULL), 38206 La Laguna, Tenerife, Spain
[44] European Southern Observatory, ESO Vitacura, Alonso de Cordova 3107, Vitacura, Casilla 19001 Santiago, Chile
[45] European Space Agency, ESAC, Planck Science Office, Camino bajo del Castillo, s/n, Urbanización Villafranca del Castillo, 28691 Villanueva de la Cañada, Madrid, Spain
[46] European Space Agency, ESTEC, Keplerlaan 1, 2201 AZ Noordwijk, The Netherlands
[47] Facoltà di Ingegneria, Università degli Studi e-Campus, via Isimbardi 10, 22060 Novedrate (CO), Italy
[48] GEPI, Observatoire de Paris, Section de Meudon, 5 Place J. Janssen, 92195 Meudon Cedex, France
[49] Gran Sasso Science Institute, INFN, viale F. Crispi 7, 67100 L'Aquila, Italy
[50] HGSFP and University of Heidelberg, Theoretical Physics Department, Philosophenweg 16, 69120 Heidelberg, Germany
[51] Helsinki Institute of Physics, Gustaf Hällströmin katu 2, University of Helsinki, 00560 Helsinki, Finland
[52] INAF−Osservatorio Astrofisico di Catania, via S. Sofia 78, Catania, Italy
[53] INAF−Osservatorio Astronomico di Padova, Vicolo dell'Osservatorio 5, 35131 Padova, Italy
[54] INAF−Osservatorio Astronomico di Roma, via di Frascati 33, 00040 Monte Porzio Catone, Italy
[55] INAF−Osservatorio Astronomico di Trieste, via G.B. Tiepolo 11, 34127 Trieste, Italy
[56] INAF/IASF Bologna, Via Gobetti 101, 40127 Bologna, Italy
[57] INAF/IASF Milano, Via E. Bassini 15, 20133 Milano, Italy
[58] INFN, Sezione di Bologna, Via Irnerio 46, 40126, Bologna, Italy
[59] INFN, Sezione di Roma 1, Università di Roma Sapienza, Piazzale Aldo Moro 2, 00185 Roma, Italy
[60] INFN, Sezione di Roma 2, Università di Roma Tor Vergata, Via della Ricerca Scientifica, 1 Roma, Italy
[61] INFN/National Institute for Nuclear Physics, via Valerio 2, 34127 Trieste, Italy
[62] IPAG; Institut de Planétologie et d'Astrophysique de Grenoble, Université Grenoble Alpes, IPAG; CNRS, IPAG, 38000 Grenoble, France
[63] IUCAA, Post Bag 4, Ganeshkhind, Pune University Campus, 411 007 Pune, India
[64] Imperial College London, Astrophysics group, Blackett Laboratory, Prince Consort Road, London, SW7 2AZ, UK
[65] Infrared Processing and Analysis Center, California Institute of Technology, Pasadena, CA 91125, USA
[66] Institut Néel, CNRS, Université Joseph Fourier Grenoble I, 25 rue des Martyrs, 38042 Grenoble, France
[67] Institut Universitaire de France, 103 Bd Saint-Michel, 75005 Paris, France
[68] Institut d'Astrophysique Spatiale, CNRS (UMR8617) Université Paris-Sud 11, Bâtiment 121, 91898 Orsay, France
[69] Institut d'Astrophysique de Paris, CNRS (UMR7095), 98 bis Boulevard Arago, 75014 Paris, France
[70] Institute of Astronomy, University of Cambridge, Madingley Road, Cambridge CB3 0HA, UK
[71] Institute of Theoretical Astrophysics, University of Oslo, Blindern, 0371 Oslo, Norway
[72] Instituto de Astrofísica de Canarias, C/Vía Láctea s/n, La Laguna, 38205 Tenerife, Spain

[73] Instituto de Astrofísica de Canarias, 38200 La Laguna, Tenerife, Spain
[74] Instituto de Física de Cantabria (CSIC-Universidad de Cantabria), Avda. de los Castros s/n, 39005 Santander, Spain
[75] Istituto Nazionale di Astrofisica – Osservatorio Astronomico di Roma, via Frascati 33, 00040 Monte Porzio Catone (RM), Italy
[76] Istituto Nazionale di Fisica Nucleare, Sezione di Padova, via Marzolo 8, 35131 Padova, Italy
[77] Jet Propulsion Laboratory, California Institute of Technology, 4800 Oak Grove Drive, Pasadena, California, USA
[78] Jodrell Bank Centre for Astrophysics, Alan Turing Building, School of Physics and Astronomy, The University of Manchester, Oxford Road, Manchester, M13 9PL, UK
[79] Kavli Institute for Cosmology Cambridge, Madingley Road, Cambridge, CB3 0HA, UK
[80] LAL, Université Paris-Sud, CNRS/IN2P3, Orsay, France
[81] LAPTh, Univ. de Savoie, CNRS, BP 110, 74941 Annecy-le-Vieux, France
[82] LERMA, CNRS, Observatoire de Paris, 61 Avenue de l'Observatoire, 75000 Paris, France
[83] Laboratoire AIM, IRFU/Service d'Astrophysique – CEA/DSM – CNRS – Université Paris Diderot, Bât. 709, CEA-Saclay, 91191 Gif-sur-Yvette Cedex, France
[84] Laboratoire Traitement et Communication de l'Information, CNRS (UMR 5141) and Télécom ParisTech, 46 rue Barrault, 75634 Paris Cedex 13, France
[85] Laboratoire de Physique Subatomique et Cosmologie, Université Grenoble-Alpes, CNRS/IN2P3, 53 rue des Martyrs, 38026 Grenoble Cedex, France
[86] Laboratoire de Physique Théorique, Université Paris-Sud 11 & CNRS, Bâtiment 210, 91405 Orsay, France
[87] Lawrence Berkeley National Laboratory, Berkeley, CA 94720 California, USA
[88] Lebedev Physical Institute of the Russian Academy of Sciences, Astro Space Centre, 84/32 Profsoyuznaya st., 117997 Moscow, GSP-7, Russia
[89] Max-Planck-Institut für Astrophysik, Karl-Schwarzschild-Str. 1, 85741 Garching, Germany
[90] Max-Planck-Institut für Extraterrestrische Physik, Giessenbachstraße, 85748 Garching, Germany
[91] McGill Physics, Ernest Rutherford Physics Building, McGill University, 3600 rue University, Montréal, QC, H3A 2T8, Canada
[92] Moscow Institute of Physics and Technology, Institutsky per., 9, 141700 Dolgoprudny, Russia
[93] National University of Ireland, Department of Experimental Physics, Maynooth, Co. Kildare, Ireland
[94] Niels Bohr Institute, Blegdamsvej 17, 1165 Copenhagen, Denmark
[95] Optical Science Laboratory, University College London, Gower Street, London, UK
[96] SB-ITP-LPPC, EPFL, 1015 Lausanne, Switzerland
[97] SISSA, Astrophysics Sector, via Bonomea 265, 34136 Trieste, Italy
[98] SLAC National Accelerator Laboratory, Menlo Park, CA 94025, USA
[99] School of Physics and Astronomy, Cardiff University, Queens Buildings, The Parade, Cardiff, CF24 3AA, UK
[100] School of Physics and Astronomy, University of Nottingham, Nottingham NG7 2RD, UK
[101] Sorbonne Université-UPMC, UMR7095, Institut d'Astrophysique de Paris, 98 bis Boulevard Arago, 75014 Paris, France
[102] Space Research Institute (IKI), Russian Academy of Sciences, Profsoyuznaya Str, 84/32, 117997 Moscow, Russia
[103] Space Sciences Laboratory, University of California, Berkeley, California, CA 94720 USA
[104] Special Astrophysical Observatory, Russian Academy of Sciences, Nizhnij Arkhyz, Zelenchukskiy region, 369167 Karachai-Cherkessian Republic, Russia
[105] Sterrewacht Leiden, PO Box 9513, 2300 RA Leiden, The Netherlands
[106] Sub-Department of Astrophysics, University of Oxford, Keble Road, Oxford OX1 3RH, UK
[107] TÜBİTAK National Observatory, Akdeniz University Campus, 07058 Antalya, Turkey
[108] Theory Division, PH-TH, CERN, 1211 Geneva 23, Switzerland
[109] UCLA Astronomy, PO Box 951547, Los Angeles CA 90095-1547, USA
[110] UPMC Univ. Paris 06, UMR7095, 98 bis Boulevard Arago, 75014 Paris, France
[111] Universidad Andrés Bello, Dpto. de Ciencias Fisicas, Facultad de Ciencias Exactas, 8370134 Santiago de Chile, Chile
[112] Université Denis Diderot (Paris 7), 75205 Paris Cedex 13, France
[113] Université de Toulouse, UPS-OMP, IRAP, 31028 Toulouse Cedex 4, France
[114] Universities Space Research Association, Stratospheric Observatory for Infrared Astronomy, MS 232-11, Moffett Field, CA 94035, USA
[115] University Observatory, Ludwig Maximilian University of Munich, Scheinerstrasse 1, 81679 Munich, Germany
[116] University of Granada, Departamento de Física Teórica y del Cosmos, Facultad de Ciencias, 18071 Granada, Spain
[117] University of Granada, Instituto Carlos I de Física Teórica y Computacional, 18071 Granada, Spain
[118] Warsaw University Observatory, Aleje Ujazdowskie 4, 00-478 Warszawa, Poland

Table A.1. Optical information for our high-z SDSS confirmations.

Name	$\alpha_{\rm BCG}$	$\delta_{\rm BCG}$	z	N_z
PSZ2 G076.18-47.30 ...	343.1475	4.5381	0.666	3
PSZ2 G087.39+50.92 ..	231.6383	54.1520	0.748	1
PSZ2 G089.39+69.36 ..	208.4382	43.4843	0.68	...
PSZ2 G097.52+51.70 ..	223.8374	58.8707	0.7	...

Notes. Alongside the redshift, we give the RA and Dec of the BCG and if the redshift is spectroscopic, N_z gives number of cluster members with spectroscopic redshifts.

Appendix A: High-redshift SDSS confirmations

Table A.1 gives optical information for four high-redshift confirmations found using a search in SDSS data around unmatched *Planck* detections.

We use a multi-wavelength approach to confirm the clusters. Each of these candidates possess coincident high-redshift optical over-densities in SDSS, firm infra-red confirmations from WISE, and significant emission in the ROSAT 0.5–2.4 keV band. We estimate the X-ray luminosity from the ROSAT maps using growth-curve analysis, and confirm that the luminosity is consistent with the measured $M_{\rm SZ}$ as discussed in Sect. 7.2.

One interesting case is PSZ2 G097.52+51.70, which appears to be a near line-of-sight projection with components at $z = 0.7$ and $z = 0.333$, separated by 1.91 arcmin. Both systems may contribute to the observed *Planck* signal. We have associated the *Planck* source with the high-redshift cluster because it is significantly closer to the SZ centre (0.714 arcmin vs. 2.47 arcmin separation), and because it is coincident (0.23 arcmin) with the ROSAT X-ray centre. The $z = 0.333$ system shows less significant hard-band emission.

Appendix B: Differences in PSZ1 and PSZ2 redshift assignments

The PSZ2 contains 782 clusters that had redshift estimates in the PSZ1. We assign the same redshift in all but 43 of these cases. In 25 of these cases, there is no significant difference (defined by $|\Delta z| > 0.03$ or $|\Delta z|/z > 0.1$) between the estimates and we have updated PSZ1 photometric redshift from various sources to new estimates from `redMaPPer` or *Planck* follow-ups.

We have updated a further seven PSZ1 photometric redshifts with recent *Planck* ENO follow-up redshifts (Planck Collaboration Int. XXXVI 2016) where the redshift has significantly changed. Of these, one was from the PSZ1 SDSS search, two were from PanSTARRs and four were from earlier *Planck* photometric follow-ups. These updates are included in the 2015 revision of the PSZ1 redshift compilation (Planck Collaboration XXXII 2015).

We discuss the remaining 11 significant differences below.

- *PSZ2 G020.66+37.99* (PSZ1 INDEX 51):
  Rozo et al. (2015) discuss this cluster in depth. `redMaPPer` finds two overlapping clusters, $z_{\rm spec} = 0.338, \lambda = 85.4$ and $z_{\rm spec} = 0.443, \lambda = 23.5$. The PSZ1 redshift $z_{\rm phot} = 0.39$ from WFI *Planck* follow-up is likely to be biased by members from the less rich and more distant system. For the PSZ2, we choose the higher richness match and quote $z_{\rm phot} = 0.345$. The 2015 update to the PSZ1 adopts this change.
- *PSZ2 G066.68+68.44* (PSZ1 INDEX 222):
  This is an ambiguous system. The PSZ1 used $z_{\rm spec} = 0.1813$ from NORAS (Böhringer et al. 2000). For the PSZ2 we have quoted $z_{\rm phot} = 0.163$ from `redMaPPer`, which agrees with the estimate $z_{\rm spec} = 0.16$ from BCS follow-up (Struble & Rood 1999; Crawford et al. 1995) and the SDSS BCG estimate $z_{\rm spec} = 0.163$. The decision between these two ROSAT follow-up spectroscopic redshifts rests on the `redMaPPer` information, which identifies a rich $\lambda = 84.1$ system at $z_{\rm phot} = 0.163$.
- *PSZ2 G087.39+50.92* (PSZ1 INDEX 299):
  The PSZ2 position has moved closer to a clear high-redshift SDSS cluster at $z_{\rm spec} = 0.748$ at separation $0.9 \times \theta_{\rm err}$, and away from the PSZ1 SDSS match which is now at $2.62 \times \theta_{\rm err}$. There is also clear ROSAT 0.5–2.4 keV X-ray emission at the high-z location, whose strength is consistent with the SZ emission, while there is no significant emission at the PSZ1 SDSS match location.
- *PSZ2 G090.66-52.34* (PSZ1 INDEX 308):
  The PSZ1 redshift $z_{\rm spec} = 0.1784$ came from a single galaxy spectrum (Struble & Rood 1999). `redMaPPer` suggest that this galaxy is likely to be in the foreground, with the rich $\lambda = 85$ cluster at slightly higher redshift $z_{\rm phot} = 0.197$. We note, however, that the difference is small (10.2%).
- *PSZ2 G113.91-37.01* (PSZ1 INDEX 416):
  We adopt the Rozo et al. (2015) update of the NORAS redshift, which replaced a $\lambda = 7.1$ group at $z = 0.135$ with a rich $\lambda = 159$ cluster at $z = 0.371$ separated by 8 arcmin.
- *PSZ2 G121.13+49.64* (PSZ1 INDEX 443):
  We note that this system is a probable projection. We adopt the correction of the redshift from Rozo et al. (2015), noting that the richness of the $z = 0.22$ component is consistent with the SZ signal, while the $z = 0.438$ system matched in the PSZ1 is insufficiently rich. The 2015 update to the PSZ1 adopts this change.
- *PSZ2 G143.26+65.24* (PSZ1 INDEX 513):
  The PSZ1 association with ACO 1430 is correct, but we update the redshift of $z_{\rm spec} = 0.211$ from two members (Struble & Rood 1991) with $z_{\rm phot} = 0.363$ from `redMaPPer`. The X-ray and optical images show an E-W elongation and two possible galaxy concentrations, possibly a projection. The high-redshift component has richness consistent with the SZ signal. The 2015 update to the PSZ1 adopts this change.
- *PSZ2 G151.19+48.27* (PSZ1 INDEX 537):
  The PSZ1 association with A0959 is correct. NED lists two literature redshifts for this cluster: 0.289 (which we adopt) and 0.353 (adopted in the PSZ1). This object is bimodal in the optical and in the X-ray and is almost certainly a projection. `redMaPPer` suggests association with the 0.289 component, based on consistency of richness with the SZ signal. The 2015 update to the PSZ1 adopts this change.
- *PSZ2 G259.30+84.41* (PSZ1 INDEX 888):
  We adopt the correction of Rozo et al. (2015) to the PSZ1 redshift $z_{\rm phot} = 0.4125$ from NSCS, instead matching to a clear and rich SDSS cluster within 1 arcmin of the *Planck* position at $z_{\rm phot} = 0.323$. The 2015 update to the PSZ1 adopts this change.
- *PSZ2 G310.81+83.91* (PSZ1 INDEX 1093):
  The PSZ2 matched to an SDSS cluster at $z_{\rm phot} = 0.446$. `redMaPPer` finds this potential counterpart to be insufficiently rich to be detected by *Planck* at this redshift and there is no X-ray emission in ROSAT. The *Planck* detection may be spurious; there are point sources detected at 353 and 545 GHz and the neural network quality assessment suggests a contaminated spectrum. We therefore break the association and leave the detection unconfirmed.

– *PSZ2 G318.62+58.55* (PSZ1 INDEX 1123):
We adopt the correction of Rozo et al. (2015) of the PSZ1 redshift $z_{\rm spec} = 0.1144$. This makes an association to a different cluster at 4.56 arcmin separation, with `redMaPPer` redshifts $z_{\rm phot} = 0.22$ ($z_{\rm spec} = 0.233$), and richness $\lambda = 69.3$.

Appendix C: Modifications of the extraction algorithms since the PSZ1 release

C.1. MMF1

The MMF1 code used for the PSZ2 is the same as for the PSZ1 with the following changes:

– position estimates are now calculated with sub-pixel positioning using posteriors marginalized over all other parameters, rather than taking the pixel centre closest to the peak;
– position error radius estimation has been debugged;
– the 2D contour grids for (Y, θ) expand dynamically if the 91% confidence region is not entirely contained within the grid, although this expansion is not applied to S/N< 5 detections.

C.2. MMF3

For the PSZ2 release, we made three improvements to our MMF3 code.

– Bright clusters impact the estimation of background. For the PSZ1 we adopted two different estimators of the MMF3 background depending on the S/N of the detections. If the S/N was below 20, the theoretical calculation was used (see Eq. (7) in Melin et al. 2006) while, for S/N greater than 20, we used the standard deviation of the filtered map. When the cluster signal is subdominant in the map the two estimators return the same result, but they differ if the cluster is bright (typically with S/N above 20) due to the contamination of the background by the cluster itself. The choice of using two estimators has been made to make the MMF3 background estimate compatible with PwS and MMF1 for the PSZ1. We tested it against the QA after the 2013 release and found that it biases significantly the MMF3 two dimensional ($\theta_{\rm s}$, Y_{5R500}) contours with respect to injected cluster size and flux at high S/N. We thus decided to come back to the theoretical calculation of the background across all the S/N range, as in the earlier version of MMF3 used for the ESZ. This choice fixes the issue with high S/N cluster contours in the QA; however it increases the S/N value and shifts the ($\theta_{\rm s}$,Y_{5R500}) contours for MMF3 detections in the PSZ2 release with respect to PSZ1 for the detections with S/N above 20, more than the increase expected from the additional integration time. For the PSZ2, PwS now estimates the cross-channel covariance matrix under the "native" prescription (see PwS section in this appendix). This improvement makes the background estimate compatible with the theoretical calculation from MMF3 and also gives unbiased estimates for the PwS two dimensional contours in the QA.
– MMF3 two dimensional ($\theta_{\rm s}$,Y_{5R500}) contours in the PSZ1 were tested against the QA after the 2013 release. The contours were found to be wider than expected. The code has been corrected and new contours have been produced and included in the *Planck* Legacy Archive for the PSZ1. The PSZ2 relies on this new and fully tested estimate of the two dimensional contours.
– The MMF3 positional error for the PSZ1 was overestimated. The code has been corrected and tested against the QA. New estimates have been produced and included in the Planck Legacy Archive for the PSZ1. The PSZ2 uses the new estimate of the positional error.

C.3. PwS

The PwS code used for PSZ2 is similar to the one used for PSZ1, with two modifications.

– The cross-channel covariance matrix is now always estimated using iterative recalibration but is parameterized in order to produce a smoother estimate. Using the QA, we have shown that the new calibration only impacts the S/N estimate (by about 12%), keeping unchanged all other parameter estimates. The new S/N estimates are consistent with the other codes.
– For ($\theta_{\rm s}$,Y_{5R500}), we now adopt non-informative priors, formulated using Jeffrey's method (Carvalho et al. 2012), instead of informative priors derived from a fiducial cosmology and mass function.

Appendix D: Description of the delivered products

The data products comprise: (i) the main catalogue, which contains the characterized catalogue with ancillary information; (ii) individual algorithm catalogues produced by each of the codes prior to merging to create the main catalogue, which contain Y–θ parameter posteriors per cluster; and (iii) selection function files containing the completeness and survey masks for various sample definitions. All the products are available from the Planck Legacy Archive maintained by ESA[8].

D.1. Main catalogue

See Table D.1.

D.2. Individual algorithm catalogues

See Table D.2.

Second extension HDU

The second extension HDU contains a three-dimensional image with the two-dimensional probability distribution in $\theta_{\rm s}$ and Y_{5R500} for each cluster. The probability distributions are evaluated on a 256×256 linear grid between the limits specified in the first extension HDU. The limits are determined independently for each detection. The dimensions of the 3D image are $256 \times 256 \times n$, where n is the number of detections in the catalogue. The second dimension is $\theta_{\rm s}$ and the first dimension is Y_{5R500}.

Third extension HDU

The third extension HDU contains a three-dimensional image with the $M_{\rm SZ}$ observable information per cluster as a function of assumed redshift. The image dimensions are $100 \times 4 \times n$, where n is the number of detections in the catalogue. The first dimension is the assumed redshift. The second dimension has size 4 and the first element is the assumed redshift value for the $M_{\rm SZ}$ fields. The second element is the $M_{\rm SZ}$ lower 67% confidence bound, the third element is the $M_{\rm SZ}$ estimate and the fourth element is the $M_{\rm SZ}$ upper 67% confidence bound, all in units of 10^{14} $M_{\odot}$. These errors are based on the Planck measurement uncertainties only; not included in the error estimates are the statistical errors on the

[8] http://www.cosmos.esa.int/web/planck/pla

Table D.1. Column definitions of the main (union) catalogue table.

Column name	Data type	Units	Description
INDEX	Integer(4)	...	Index of detection[a]
NAME	String	...	Name of detection[b]
GLON	Real(8)	[degrees]	Galactic longitude ($0° \leq l < 360°$)
GLAT	Real(8)	[degrees]	Galactic latitude ($-90° \leq b \leq 90°$)
RA	Real(8)	[degrees]	Right ascension (J2000)
DEC	Real(8)	[degrees]	Declination (J2000)
POS_ERR	Real(4)	[arcmin]	Uncertainty in position[c]
SNR	Real(4)	...	S/N of detection
PIPELINE	Integer(4)	...	Pipeline from which information is taken: the reference pipeline[d]
PIPE_DET	Integer(4)	...	Information on pipelines making detection[d]
PCCS2	Boolean	...	Indicates whether detection matches with any in PCCS2 catalogues
PSZ	Integer(4)	...	Index of matching detection in PSZ1, or –1 if a new detection
IR_FLAG	Integer(1)	...	Flag denoting heavy IR contamination
Q_NEURAL	Real(4)	...	Neural network quality flag[e]
Y5R500	Real(4)	[10^{-3} arcmin^2]	Mean marginal Y_{5R500} as measured by the reference pipeline
Y5R500_ERR	Real(4)	[10^{-3} arcmin^2]	Uncertainty on Y_{5R500} as measured by the reference pipeline
VALIDATION	Integer(4)	...	External validation status[f]
REDSHIFT_ID	String	...	External identifier of cluster associated with redshift measurement[g]
REDSHIFT	Real(4)	...	Redshift of clusters[g]
MSZ	Real(4)	[10^{14} $M_\odot$]	SZ mass proxy[h]
MSZ_ERR_UP	Real(4)	[10^{14} $M_\odot$]	Upper 1σ SZ mass proxy confidence interval[h]
MSZ_ERR_LOW	Real(4)	[10^{14} $M_\odot$]	Lower 1σ SZ mass proxy confidence interval[h]
MCXC	String	...	ID of X-ray counterpart in the MCXC if one is present
REDMAPPER	String	...	ID of optical counterpart in the `redMaPPer` catalogue if one is present
ACT	String	...	ID of SZ counterpart in the ACT catalogues if one is present
SPT	String	...	ID of SZ counterpart in the SPT catalogues if one is present
WISE_FLAG	Integer(4)	...	Confirmation flag of WISE IR overdensity[i]
AMI_EVIDENCE	Real(4)	...	Bayesian evidence for AMI counterpart detection[i]
COSMO	Boolean	...	Indicates whether the cluster is in the cosmology sample
COMMENT	String	...	Comments on this detection

Notes. [(a)] The index is determined by the order of the detections in the union catalogue. The matching entries in the individual catalogues have the same index to facilitate cross-referencing. [(b)] The names are in the format PSZ2 Gxxx.xx ± yy.yy where xxx.xx is the Galactic longitude and ±yy.yy is the Galactic latitude of the detection, both in degrees. The coordinates are truncated towards zero, not rounded. [(c)] The value given here is the 95% confidence interval of the distribution of radial displacement. [(d)] The PIPELINE column defines the pipeline from which the values in the union catalogue are taken: 1 = `MMF1`; 2 = `MMF3`; and 3 = `PwS`. The PIPE_DET column is used to indicate which pipelines detect this object. The three least significant decimal digits are used to represent detection or non-detection by the pipelines. Order of the digits: hundreds = MMF1; tens = MMF3; and units = `PwS`. If it is detected then the corresponding digit is set to 1, otherwise it is set to 0. [(e)] The neural network quality flag is 1-$Q_{\rm bad}$, following the definitions in Aghanim et al. (2015). Values Q_NEURAL < 0.4 denote low-reliability detections. [(f)] The VALIDATION column gives a summary of the external validation, encoding the most robust external identification: –1 = no known external counterpart; 10 = ENO follow-up; 11 = RTT follow-up; 12 = PanSTARRs; 13 = `redMaPPer` non-blind; 14 = SDSS high-z; 15 = AMI; 16 = WISE; 20 = legacy identification from the PSZ1 2013 release; 21 = MCXC; 22 = SPT; 23 =ACT; 24 = `redMaPPer`; 25 = PSZ1 counterpart with redshift updated in Planck Collaboration XXXII (2015); and 30 = NED. [(g)] The redshift source is the most robust external validation listed in the VALIDATION field. [(h)] Definition of $M_{\rm SZ}$. The hydrostatic mass, M_{500}, assuming the Y–M scaling relation of Eq. (7) of Planck Collaboration XX (2014) as a prior that cuts a plane through the parameter contours (see Sect. 5.3). The assumed cosmology for this calculation $h = 0.7$, $\Omega_{\rm m} = 0.3$ and $\Omega_\Lambda = 0.7$. The errors are 67% confidence statistical errors and based on the *Planck* measurement uncertainties only. Not included in the error estimates are the statistical errors on the scaling relation, the intrinsic scatter in the relation, or systematic errors in data selection for the scaling relation fit. [(i)] The WISE confirmation flag is assigned by visual inspection and defined to be one of $[-10, -2, -1, 0, 1, 2, 3]$, where –10 denotes no information and the other values are discussed in Sect. 7.4. The Bayesian evidence for the AMI counterpart is defined in Sect. 7.5.3.

scaling relation, the intrinsic scatter in the relation, or systematic errors in data selection for the scaling relation fit.

D.3. Selection function file format

The selection function information is stored in FITS files. The filenames of the catalogues are of the form PSZ2-selection_Rx.xx.fits, where x.xx is the release number.

First extension HDU

The first extension HDU contains the survey region, denoted by an $N_{\rm side} = 2048$ ring-ordered `HEALPix` map in Galactic coordinates. Pixels in the survey region have the value 1.0, while areas outside of the survey region have value 0.0.

Table D.2. Column definitions of the individual algorithm catalogue tables.

Column name	Data type	Units	Description
INDEX	Integer(4)	...	Index of detection[a]
NAME	String	...	Name of detection[a]
GLON	Real(8)	[degrees]	Galactic longitude ($0° \leq l < 360°$)
GLAT	Real(8)	[degrees]	Galactic latitude ($-90° \leq b \leq 90°$)
RA	Real(8)	[degrees]	Right ascension (J2000)
DEC	Real(8)	[degrees]	Declination (J2000)
POS_ERR	Real(4)	[arcmin]	Uncertainty in position[b]
SNR	Real(4)	...	S/N of detection[c]
TS_MIN	Real(4)	[arcmin]	Minimum θ_s in second extension HDU[d]
TS_MAX	Real(4)	[arcmin]	Maximum θ_s in second extension HDU[d]
Y_MIN	Real(4)	[arcmin^2]	Minimum Y_{5R500} in second extension HDU[d]
Y_MAX	Real(4)	[arcmin^2]	Maximum Y_{5R500} in second extension HDU[d]

Notes. [(a)] The index and name are taken from the union catalogue. The matching entries in the individual catalogues have the same index and name to facilitate cross-referencing. [(b)] The value given here is the 95% confidence interval of the distribution of radial displacements. [(c)] The SNR column contains the native signal-to-noise ratio determined by the detection pipeline. [(d)] These entries define the limits of the grid used to evaluate the 2D probability distribution of θ_s and Y_{5R500} in the second extension HDU (see below).

Second extension HDU

The second extension HDU consists of a three-dimensional image containing the survey completeness probability distribution for various thresholds. The information is stored in an image of size $30 \times 32 \times 12$. The first dimension is Y_{500}, the second dimension is θ_{500}, and the third dimension is the signal-to-noise threshold. The units are percent, lie in the range 0–100, and denote the detection probability of a cluster lying within the given Y_{500}–θ_{500} bin.

Third extension HDU

The second extension HDU contains the Y_{500} grid values for the completeness data cube held in the second extension. It has length 30 and spans the range 1.12480×10^{-4} arcmin^2 – 7.20325×10^{-2} arcmin^2 in logarithmic steps.

Fourth extension HDU

The fourth extension HDU contains the θ_{500} grid values for the completeness data cube held in the second extension. It has length 32 and spans the range 0.9416−35.31 arcmin in logarithmic steps.

Fifth extension HDU

The fifth extension HDU contains the signal-to-noise threshold grid values for the completeness data cube held in the second extension. It has length 12 and contains thresholds at intervals of 0.5 from 4.5 to 10.0.

Appendix E: Detail of missing PSZ1 detections

Table E.1. Detail of the 291 PSZ1 detections not present in the PSZ2 catalogue.

Index	S/N	Pipeline	PIPE_DET	ID_EXT	Redshift	S/N (non-blind)	Type
4.....	6.04	3	101	...	...	...	3
8	4.92	1	100	...	...	0.34	1
9	5.76	1	100	...	...	...	3
13	4.52	1	100	ZwCl 1454.5+0656	0.429	3.73	1
28	4.70	2	10	...	0.46	3.54	1
30	4.72	1	100	...	...	1.83	1
32	4.54	1	100	...	...	1.65	1
34	4.50	1	100	...	...	1.42	1
38	4.65	1	100	...	...	2.48	1
40	4.89	2	10	...	...	2.90	1
41	4.81	2	10	...	...	2.90	1
43	4.76	2	10	...	...	2.69	1
52	5.71	2	10	...	0.39	...	4
58	4.56	1	100	...	...	2.06	1
59	4.63	1	100	...	...	3.27	1
60	4.84	2	10	RXC J1917.5-1315	0.177	3.11	1
61	5.06	2	111	...	0.650893	2.91	1
62	4.95	2	11	ACO S 1010	0.28	4.02	1
66	5.20	2	10	...	...	3.19	1
68	4.67	3	1	...	...	3.45	1
77	4.58	1	100	RXC J1453.1+2153	0.1186	2.96	1
82	4.98	2	10	...	...	2.84	1
83	4.96	2	10	...	...	3.53	1
84	4.84	2	10	...	...	3.80	1
86	5.23	1	100	...	...	2.82	1
89	4.69	3	101	WHL J248.764+15.4836	0.4725	3.27	1
90	4.68	1	100	...	...	2.11	1
97	4.82	1	100	WHL J252.649+16.8253	0.3612	2.56	1
98	4.70	3	1	...	...	3.54	1
104	4.54	2	10	...	...	1.94	1
111	4.57	2	10	...	...	1.97	1
112	4.61	1	100	...	...	1.59	1
121	4.70	2	110	...	...	1.22	1
126	4.67	2	10	...	...	1.91	1
128	4.54	3	1	RXC J1623.5+2634	0.4274	3.79	1
131	5.23	2	11	AMF J320.551-6.81740	0.5344	3.59	1
136	4.74	1	100	...	...	...	3
142	4.52	3	101	...	...	1.26	1
157	4.64	1	100	...	...	2.27	1
158	5.29	2	10	...	...	2.08	1
162	4.60	1	100	...	...	2.34	1
165	5.11	3	101	...	...	...	3
170	5.33	2	11	...	...	4.32	1
175	4.82	1	100	...	0.1944	2.84	1
176	5.72	2	10	...	...	...	3
184	4.76	3	1	...	...	2.67	1
193	4.55	1	100	...	...	2.83	1
199	4.55	3	1	...	...	2.12	1
203	4.65	2	10	...	...	1.98	1
211	4.58	3	1	...	...	3.31	1
212	4.54	3	1	...	...	3.72	1
213	4.70	2	10	...	...	2.93	1
223	4.51	2	10	...	0.3341	3.16	1
233	4.79	2	10	ZwCl 2151.0+1325	0.205	3.97	1
237	4.78	1	100	ACO 2429	...	3.36	1
251	5.17	1	100	...	...	2.59	1
257	4.90	2	11	...	...	3.68	1
260	4.78	2	110	WHL J242.728+51.2267	0.4096	3.60	1
262	4.52	1	100	...	...	3.63	1

Notes. The TYPE column lists the reason why the detection was dropped. TYPE 1 lost detections are low-S/N sources lost due to changes in the noise realization. The "S/N (non blind)" field contains the non-blind S/N for the Y signal in the full-mission maps at the location and size of the PSZ1 detection and is provided for all TYPE 1 lost detections (whereas the field S/N is for the PSZ1). TYPE 2 sources are lost behind the new point source mask. TYPE 3 are removed due to IR contamination. TYPE 4 are cut by internal PwS consistency criteria. Each of these types are discussed in Sect. 6.3.

Table E.1. continued.

Index	S/N	Pipeline	PIPE_DET	ID_EXT	Redshift	S/N (non-blind)	Type
267	6.37	2	111	ACTJ2327.4-0204	0.705	...	2
271	4.71	2	10	...	...	3.84092	1
272	4.57	3	1	ZwCl 1746.2+5429	0.31	3.9982	1
276	4.65	2	11	...	...	2.88368	1
278	4.55	2	10	...	0.306807	2.32043	1
300	5.07	2	10	...	0.1132	4.09432	1
305	4.82	2	10	...	...	2.12439	1
306	4.90	1	100	...	...	3.50522	1
309	5.37	2	110	ZwCl 1602.3+5917	0.2544	4.0135	1
311	4.64	2	110	...	...	...	3
314	5.18	1	100	...	...	1.77555	1
317	5.46	1	100	...	...	1.0888	1
321	4.58	1	100	ZwCl 1604.4+6113	0.3447	4.06313	1
327	5.78	3	101	RXC J2318.4+1843	0.0389		4
331	4.79	3	101	...	...	2.53009	1
333	4.71	3	1	WHL J286.905+64.5511	0.3561	3.89137	1
336	6.55	2	111	...	...	...	3
349	4.87	2	11	...	...	...	2
361	4.71	2	10	...	...	1.27901	1
365	4.82	3	101	RXC J1834.1+7057	0.0824	3.43465	1
367	4.52	2	10	ZwCl 1748.0+7125	...	2.72016	1
370	5.08	2	110	...	...	...	3
371	4.55	2	110	...	...	...	3
372	4.63	2	11	...	...	4.02674	1
373	4.50	2	10	...	...	...	2
375	4.78	3	101	...	...	3.02917	1
376	4.54	2	10	AMF J359.521+15.1625	0.1785	2.56247	1
382	4.73	2	110	...	...	...	3
387	4.66	2	111	...	...	...	2
396	4.55	2	10	...	0.25	1.78124	1
397	6.89	2	111	...	...	...	3
398	4.55	2	10	...	...	...	3
400	4.58	2	111	...	0.533998	2.74459	1
405	4.81	1	100	WHL J358.170+38.9803	0.27	2.79469	1
412	4.76	3	1	...	...	3.08399	1
426	5.85	2	111	...	...	...	2
430	4.54	3	1	...	...	3.59742	1
436	4.96	3	101	...	...	3.37978	1
437	4.51153	1	100	...	...	3.4165	1
444	4.721222	2	110	...	...	3.54217	1
445	4.657247	2	10	Abell 98S	0.104	2.86664	1
446	5.346884	2	11	...	...	...	2
456	4.8859854	1	100	...	...	3.07575	1
458	4.857769	3	101	...	...	2.81502	1
462	5.401291	2	110	...	...	...	2
466	5.9113874	2	11	...	...	...	3
468	4.9521785	2	10	...	...	3.00375	1
469	4.898088	2	11	...	0.423	2.90179	1
476	4.909587	2	10	...	...	2.66482	1
478	5.421913	3	1	...	...	...	3
479	4.814969	2	11	...	...	4.24698	1
483	4.5689936	2	10	...	...	3.39778	1
488	4.5772305	1	100	RXC J0115.2+0019	0.045	3.60322	1
489	4.57693	3	1	...	...	2.75025	1
490	5.2208633	2	10	...	...	3.17854	1
491	4.5107737	1	100	RXC J0152.9+3732	0.2993	3.61788	1
504	4.9024134	1	100	...	...	2.99012	1
505	4.531147	2	10	...	0.172448	2.87619	1
517	4.6261425	2	10	...	...	2.33451	1
522	6.621042	3	110	...	...	...	3
524	4.955422	3	1	RXC J0209.5+1946	0.0657	3.5731	1
527	4.52441	1	100	...	0.38508	1.53553	1
529	8.404867	2	111	...	...	...	2
534	4.7526336	3	1	...	...	...	3
538	4.6985216	1	100	...	...	3.61937	1
539	5.5858	2	111	ACO 307	...	3.51864	1
544	4.7949095	2	10	...	...	3.56745	1
555	4.5136585	3	1	...	...	2.81332	1
556	5.27531	2	111	...	0.532786	3.53787	1
557	4.7586565	1	100	...	...	1.96562	1
559	4.674867	1	100	...	...	2.48062	1
562	4.6401553	2	10	RXC J0157.4-0550	0.1289	4.35153	1

Table E.1. continued.

Index	S/N	Pipeline	PIPE_DET	ID_EXT	Redshift	S/N (non-blind)	Type
564	6.557654	1	100	...	...	...	3
565	5.2208285	2	111	RXC J0137.4-1259	0.2143	5.1613	1
576	4.5137296	1	100	...	...	2.81468	1
586	5.319431	2	10	...	...	3.03603	1
590	4.8859153	2	11	...	...	4.82751	1
592	4.6193595	2	10	RXC J0822.1+4705	0.1303	3.47281	1
604	4.6777244	1	100	RXC J0248.0-0332	0.1883	3.19088	1
605	5.0145736	3	101	...	...	2.67592	1
607	4.940518	1	100	RXC J0956.0+4107	0.587	2.95738	1
611	4.816886	2	111	...	...	...	3
612	5.870266	2	11	...	...	...	2
616	5.085939	2	10	...	...	2.20452	1
618	5.4275565	2	11	...	...	3.43311	1
621	4.78395	2	11	RXC J0326.8+0043	0.45	2.89631	1
622	5.426397	2	10	...	0.494731	1.51139	1
626	5.9038296	2	111	...	...	...	3
629	4.509565	1	100	...	...	2.06723	1
639	5.103071	3	1	...	...	4.27439	1
642	4.6462555	1	100	WHL J164.029+34.0043	0.3805	3.50245	1
645	4.509731	1	100	...	...	2.59932	1
650	4.556457	1	100	...	0.47	1.09522	1
652	4.6217184	1	100	...	...	2.59036	1
653	5.187331	3	1	...	...	...	3
658	4.568522	1	100	...	...	1.78067	1
659	4.8158317	1	100	...	...	3.23821	1
669	4.849164	2	10	RXC J1110.7+2842	0.0314	2.96398	1
670	4.8620453	1	100	WHL J56.0261-13.5512	0.5757	3.72685	1
671	4.696646	3	1	...	...	...	2
672	4.9377847	2	110	WHL J161.821+27.9906	0.4333	3.28498	1
678	4.5387063	1	100	...	0.37572	2.00976	1
679	4.551286	1	100	...	...	3.31052	1
683	5.3817525	2	10	...	...	...	2
684	6.6154532	3	101	...	...	...	2
697	4.6185327	3	1	ACO 457	...	3.80583	1
698	4.7205544	2	10	...	...	...	2
699	4.77476	1	100	...	...	2.73017	1
704	4.563896	1	100	WHL J131.956+13.5279	0.3487	3.79252	1
705	4.6742454	1	100	...	...	0.271007	1
712	4.653271	1	100	...	...	1.52425	1
719	4.8215613	2	10	WHL J158.665+20.5346	0.4674	2.94774	1
721	4.5309896	1	100	ACO S 270	...	2.00543	1
722	4.7083845	3	1	...	...	2.76103	1
725	4.562224	2	10	...	...	3.60607	1
728	5.289766	1	100	RXC J0906.4+1020	0.1328	3.6668	1
729	4.620416	1	100	WHL J140.630+11.6581	0.2609	2.87712	1
735	4.5158153	3	1	...	...	3.3707	1
736	5.0232625	2	10	...	...	3.94745	1
737	4.517171	2	10	...	...	3.18925	1
743	4.5700955	2	10	...	...	3.44528	1
748	4.5529675	3	1	...	...	3.84224	1
749	4.9690437	3	101	ACO 3218	...	4.02593	1
750	5.1315746	2	10	...	0.31	3.37397	1
751	4.8075237	1	100	CXOMP J091126.6+055012	0.7682	3.81998	1
753	4.5188074	3	1	...	...	3.42246	1
755	7.7706156	3	1	...	...	...	2
760	4.6238937	2	110	WHL J134.086+1.78038	0.7243	2.89771	1
762	4.9262795	3	1	...	...	...	4
766	7.831258	3	1	...	...	...	4
770	4.63975	3	1	RXC J1047.5+1513	0.2108	3.50397	1
771	4.5217223	2	10	WHL J124.638-6.42296	0.5123	3.19257	1
775	6.9654646	3	1	...	...	...	2
781	4.7938952	3	1	...	...	...	3
782	4.6223207	3	1	ZwCl 0919.7-0016	0.3538	2.639	1
788	4.64205	2	10	ACO S 403	...	3.71697	1
789	5.2240515	2	110	...	...	...	3
792	4.5170665	2	10	...	...	1.3851	1
794	5.8301225	1	100	...	...	...	3
795	4.598188	2	111	WHL J170.480+15.8014	0.5593	2.95346	1
798	5.0543885	2	10	...	...	3.29023	1
809	4.588916	1	100	...	...	2.84826	1
811	4.6410813	3	1	...	...	...	3
813	4.6434965	1	100	...	...	3.05506	1

Table E.1. continued.

Index	S/N	Pipeline	PIPE_DET	ID_EXT	Redshift	S/N (non-blind)	Type
814	4.583767	3	1	...	...	4.49628	1
820	4.5714545	1	100	RXC J1013.7-0006	0.0927	2.4853	1
827	8.142719	3	1	...	...	...	2
830	4.5559297	2	10	...	...	2.32998	1
832	4.5498447	2	10	ACO S 539	...	3.03818	1
833	4.6228485	2	110	...	...	3.38266	1
836	4.7564516	2	110	RXC J0345.7-4112	0.0603	3.88946	1
843	4.513602	3	1	...	...	2.78046	1
844	4.7834334	3	1	...	...	3.91417	1
845	7.1448226	3	1	...	...	...	4
859	4.886414	3	1	...	...	1.86549	1
860	4.638687	1	100	...	...	2.41334	1
864	5.0417113	2	10	...	...	3.54132	1
866	5.168761	3	1	...	...	...	3
874	4.548713	1	100	...	...	3.45449	1
884	4.6741834	1	100	...	...	0.99106	1
885	4.5309443	3	1	...	...	3.0147	1
886	4.715562	2	111	...	...	2.5028	1
900	4.6036177	3	1	...	...	2.9232	1
908	4.6843767	2	10	...	0.45	3.14342	1
909	4.6769667	1	100	...	...	1.94061	1
913	4.872177	2	10	...	...	3.50097	1
917	4.7799654	1	100	...	...	1.45693	1
921	4.720672	2	10	...	0.26	4.22762	1
923	4.713845	1	100	...	...	1.56599	1
925	5.002551	1	100	...	...	2.16267	1
927	4.715874	1	100	...	...	1.83619	1
928	4.6580725	3	1	...	...	2.65203	1
933	4.5972934	2	10	...	...	3.05862	1
949	4.864598	3	1	...	...	1.88233	1
950	4.7590675	1	100	...	...	2.10619	1
953	4.865524	3	1	...	...	3.98468	1
964	4.946659	2	10	...	0.14	2.8276	1
965	4.5068207	1	100	...	...	1.70981	1
966	4.5067983	3	1	...	...	2.1943	1
968	4.535754	2	10	...	...	2.67392	1
973	4.5617847	1	100	...	...	1.52403	1
980	12.780052	2	111	RXC J1217.6+0339	0.0766		2
992	5.522259	2	11	...	...	0.68348	1
1010	5.906472	2	11	...	...	...	3
1016	4.763515	2	110	...	...	2.73909	1
1018	4.6082454	3	1	...	...	3.96679	1
1019	4.981976	2	11	...	...	3.89276	1
1031	4.8077016	2	110	...	...	...	3
1039	4.50475	2	10	...	...	3.30443	1
1048	4.8961234	2	10	ACO S 137	0.02764	2.49855	1
1049	4.948578	2	10	ACO 1603	0.1314	2.85532	1
1052	5.7445407	3	1	...	...	...	3
1055	4.6209354	3	1	RXC J0052.7-8015	0.1141	4.03375	1
1059	4.684562	1	100	...	...	2.7398	1
1060	6.810468	2	111	...	...	...	3
1069	4.8399434	2	10	...	0.12941	2.2881	1
1080	4.605055	1	100	...	...	2.39711	1
1081	4.6	2	10	...	...	...	3
1091	5.2132697	2	11	...	...	...	3
1092	4.6357284	2	10	...	...	3.08333	1
1094	4.676179	1	100	...	...	2.56732	1
1103	6.148161	1	100	...	...	...	2
1107	5.0184035	2	10	...	...	2.38865	1
1111	4.831168	2	10	...	...	2.73575	1
1119	5.4801097	2	10	...	...	3.52593	1
1132	4.5146875	1	100	...	...	1.42893	1
1133	4.7255597	1	100	...	0.25	2.80855	1
1135	4.781288	3	1	...	...	3.83267	1
1144	4.9033356	3	1	...	...	4.21885	1
1152	4.63114	3	1	...	...	3.60522	1
1155	4.7780237	2	111	SPT-CLJ2148-6116	0.571	3.58897	1
1159	4.7621408	1	100	...	...	2.15125	1
1162	4.628621	1	100	...	...	2.73569	1
1170	4.6537085	2	10	...	...	3.63003	1
1173	4.550007	1	100	...	...	2.2385	1
1174	6.613522	2	111	...	...	...	2

Table E.1. continued.

Index	S/N	Pipeline	PIPE_DET	ID_EXT	Redshift	S/N (non-blind)	Type
1177	5.580667	2	10	...	...	...	3
1178	4.5030346	1	100	...	...	2.90078	1
1180	5.8775973	2	111	...	...	...	3
1188	4.7791066	2	10	...	...	3.03411	1
1194	4.7459564	2	10	...	0.21	3.2567	1
1196	4.568303	1	100	...	...	2.75983	1
1197	4.775479	2	11	...	...	2.34573	1
1198	4.8042645	1	100	...	...	2.90578	1
1199	4.5996885	2	110	...	...	2.31421	1
1203	5.0193796	1	100	ACO S 808	0.049131	3.40921	1
1204	4.696981	1	100	...	0.5	3.20218	1
1212	4.7399464	1	100	...	...	2.84324	1
1215	4.6261168	1	100	...	...	3.42905	1
1217	4.5237203	2	10	...	...	2.48797	1
1219	5.1635747	3	1	...	...	...	2
1221	5.468506	2	11	...	...	...	2